Dipl.-Ing. Roland Schmied, BSc

Focused Ion Beam Structuring of Low Melting Polymeric Materials

DOCTORAL THESIS

For obtaining the academic degree
Doktor der technischen Wissenschaften

Doctoral Programme of technical Sciences
Technical Physics

Graz, University of Technology

Supervisor:
Ao.Univ.-Prof. Dipl.-Ing. Dr.techn. Ferdinand Hofer
Institute for Electron Microscopy and Nanoanalysis

Co - Supervisor:
Dipl.-Ing. Dr.techn. Harald Plank
Institute for Electron Microscopy and Nanoanalysis

Graz, December 2014

When you have eliminated the impossible,
whatever remains, however improbable, must be the truth.
(A. Conan Doyle, The Sign of Four)

Abstract

This thesis focuses on heating effects during focused ion beam (**FIB**) processing of low melting polymers. The combined approach using experiments and simulations identifies the in part massive local temperatures as a convolution between intrinsic ion-matter effects and a considerable, technically-induced heating component. While the former is invariable, the latter has been minimized by an alternative process strategy which massively improves the morphological stability and minimizes chemical damage during FIB processing, thus opening new possibilities for application on sensitive, low melting materials. The study starts with systematic experimental investigations which strongly suggested the existence of a technically-induced heating component as a consequence of classically-used serpentine or raster-like patterning strategies. Based on these results, a combined simulation approach of ion trajectories and thermal spike model calculations have been employed to get a deeper insight into spatial and temporal temperature evolution. The results were then combined with the thermodynamic behavior of polymers by means of melting and volatizing temperatures. The comparison of these simulation-based predictions with real FIB experiments revealed very good agreement, proving the applicability of the approach used to describe the temperature evolution from a fundamental point of view. As a next step, these simulations were then applied to the different scanning strategies which further confirmed the existence of a technically-induced heating component via classically-used patterning approaches. Due to the deep insight gained via simulations, an alternative patterning strategy was developed, which was expected to minimize these avoidable influences. This new strategy was then evaluated using a multi-technique approach, which revealed strongly reduced chemical damage together with increasing morphological stabilities even for temperature-sensitive polymers. Finally, this alternative strategy was applied for the preparation of ultra-thin lamellas for transmission electron microscopy. The results revealed that the new approach is capable of preserving 10 nm thick polymeric interface layers without delamination and / or chemical intermixing of adjacent layers. The successful reduction of chemical damage with increased morphological stabilities by application of the alternative patterning strategy pushes the combination of FIB processing with low melting polymers towards the unavoidable, intrinsic limit of single ion beam pulses. In consequence, this new approach is expected to open new possibilities for FIB-related soft matter processing, which in the past has often been considered to be complicated or even impossible.

Kurzfassung

Die vorliegende PhD Thesis fokussiert sich auf Temperatureffekten während der Focused Ion Beam (FIB) Prozessierung von niedrigschmelzenden Polymeren. Der kombinierte Ansatz zwischen experimentellen Methoden und Simulationen identifiziert die teilweise enormen, lokalen Temperaturen als eine Überlagerung von intrinsischen Ionen - Material Effekten mit beträchtlichen, technisch induzierten Komponenten. Während ersteres unvermeidbar ist, konnte letzteres über eine alternative Prozessstrategie minimiert werden. Dies führte zu stark verbesserten morphologischen Stabilitäten sowie reduzierten chemischen Schädigungen während der FIB Prozessierung, wodurch sich neue Möglichkeiten für den Anwendungsbereich sensibler, niedrigschmelzender Materialien eröffnen. Die Studie startet mit systematischen Experimenten, welche auf die Existenz einer technisch induzierten Temperaturkomponente aufgrund klassisch verwendeter Serpentinen- bzw. Raster-Patterningstrategien hinweist. Basierend auf diesen Resultaten wurde ein kombinierter Ansatz zwischen Simulation von Ionen Trajektorien und Thermal Spike Modell Berechnungen eingeführt um einen tieferen Einblick in die räumliche und zeitliche Temperaturevolution zu erlangen. Die Resultate wurden im Anschluss mit dem thermodynamischen Verhalten von Polymern hinsichtlich Schmelz- und Verdampfungspunkte kombiniert. Der direkte Vergleich dieser simulationsgestützten Voraussagen wurde mit realen FIB Experimenten verglichen welche sehr gute Übereinstimmung zeigten, wodurch auch die Anwendbarkeit des fundamental orientierten Ansatzes zur Temperaturentwicklung gezeigt werden konnte. Als Folgeschritt wurden diese Simulationen auf verschiedene Scan - Strategien ausgeweitet, welche die Existenz der technisch induzierten Temperaturkomponente durch klassisch verwendete Patterningstrategien weiter bestätigten. Durch diesen simulationsgestützten, tiefen Einblick in das Temperaturverhalten wurde eine alternative Patterningstrategie entwickelt, welche die vermeidbaren Komponenten minimieren sollte. Diese Strategie wurde mittels verschiedener Methoden evaluiert welche die stark reduzierte chemische Schädigung zusammen mit einer erhöhten morphologischen Stabilität selbst für temperatur - sensitive Polymer bestätigen konnte. Letztlich wurde diese alternative Strategie für die Herstellung von ultradünnen Lamellen für die

Transmissionselektronenmikroskopie verwendet. Die Resultate zeigten, dass der neue Zugang ermöglicht, 10 nm dicke Polymerzwischenschichten ohne Ablösung oder chemischer Mischung mit benachbarten Lagen aufrecht zu erhalten. Die erfolgreiche Reduktion der chemischen Schädigung bei erhöhter morphologischer Stabilität mittels der alternativen Patterningstrategie ermöglicht die FIB Prozessierung von niedrigschmelzenden Polymeren näher am unvermeidbaren, intrinsischen Limit der Einzel - Ionenpulse. Dadurch ist zu erwarten, dass dieser Ansatz neue Möglichkeiten für die Kombination FIB und weichen Materialien eröffnet welche in der Vergangenheit oftmals als kompliziert oder unmöglich galten.

Acknowledgements

First I want to thank my supervisor and head of the institute, **Prof. Dr. Ferdinand Hofer**, for giving me the unique opportunity to perform my doctoral thesis in an outstanding sophisticated scientific environment. Also my biggest gratitude goes to him for his gentle guidance and permanent support during my PhD thesis.

In particular I owe greatest thanks to **Dr. Harald Plank** as the leader of the work group S^3 and his professional supervision of this thesis. I also want to thank him for his irresistible energy in teaching me in scientific working and his incredible technical and personal support during the whole thesis revealing the far-ranging wideness of science With his outstanding knowledge and skills in many aspects of science it is always a pleasure to discuss new ideas and results with Harald. Also special thanks go to him for his inspiring, motivating and sometimes creative way as the head of the work group S3.

My special gratitude goes to **Prof. Dr. Michael Huth** for his inimitable expertise and his extremely helpful and constructive input during the review process.

Also, I want to express my appreciations to **Dr. Boril Chernev** for his uncomplicated character and the very profitable introduction and training at the Raman microscope.

I am also very grateful to **DI Angelina Orthacker** for being part in our project team. Her creative and sophisticated input strongly increased the progress and the output of the project and pushed us beyond initial thinking borders. Apart from these professional qualities I strongly benefited from our collaboration from a personal point of view.

Special appreciations go to **Martina Dienstleder** as non- straightforward FIB specialist including advanced specimen preparation. Her creative input definitely contributed to the success of the thesis for which I am very grateful.

Moreover I want to express my gratitude to **Mag. Johanna Kraxner** for her never-ending support in TEM measurements, great discussions and generating new pathways for advanced sample preparation.

Special thanks go to **Dr. Karin Wewerka** and **Dr. Armin Zankel** for the material supply, to **Sebastian Rauch**, **Manuel Paller**, **Claudia Mayrhofer** and the whole **lab crew** for their outstanding sample preparation, which was essential for this thesis. In addition I want to thank Johannes Fröch for his very motivating work during his bachelor thesis.

I also want to thank **Prof. Dr. Gregor Trimmel** and **Josefine Hobisch** for their supportive STA measurements.

Finally, I want to thank **Dr. Christian Gspan** and **DI Robert Winkler** for having such a pleasant and inspiring atmosphere at the office and their helping hand.

In general, my gratitude goes to the entire **FELMI ZFE team**, especially the S3 work group members, for their help and the personal atmosphere during the whole thesis.

I would give special thanks to **my family** for their great and continuous support even through the hard times.

Table of Contents

Abstract **iii**

Kurzfassung **v**

Acknowledgements **vii**

Introduction and Motivation **xv**

1. Fundamentals and Methodology **1**

- 1.1. Fundamentals of Dual Beam Microscopy . . . 1
  - 1.1.1. Scanning Electron Microscopy . . . 2
  - 1.1.2. Focused Ion Beam Microscopy . . . 16
- 1.2. Transmission Electron Microscopy . . . 21
  - 1.2.1. Energy Dispersive X-Ray Spectroscopy . . . 23
  - 1.2.2. Electron Energy Loss Spectroscopy . . . 24
- 1.3. Atomic Force Microscopy . . . 26
  - 1.3.1. Components . . . 27
  - 1.3.2. Topographical Imaging . . . 32
  - 1.3.3. Contact Mode . . . 34
  - 1.3.4. Tapping Mode . . . 35
  - 1.3.5. Phase Mode . . . 36
  - 1.3.6. Kelvin Probe Force Microscopy . . . 37
- 1.4. Raman Spectroscopy . . . 39
  - 1.4.1. Basic Principles . . . 41
  - 1.4.2. Instrumentation and Sampling Methods . . . 46
- 1.5. Ultramicrotomy . . . 50
- 1.6. Simulations . . . 52
- 1.7. Polymers . . . 53
  - 1.7.1. Polymer Structures . . . 53
  - 1.7.2. Phase Transition in Polymers . . . 57
  - 1.7.3. Semi-Crystalline Polymers . . . 59
  - 1.7.4. Amorphous Polymers . . . 62
- 1.8. Methodology . . . 63
  - 1.8.1. Dual Beam Microscope . . . 63
  - 1.8.2. Transmission Electron Microscope . . . 67
  - 1.8.3. Atomic Force Microscope . . . 68

1.8.4. Raman Spectroscope 69
1.8.5. Ultramicrotomy 69
1.8.6. Simulations 70

2. Results 72
2.1. Pristine Polymer Sample Characterization 72
2.1.1. Polypropylene 73
2.1.2. Polyethylene 74
2.1.3. Polymethylmethacrylate 74
2.1.4. Polyethylene Oxide 75
2.1.5. Ethylene Vinyl Acetate 76
2.1.6. Polystyrene 77
2.2. Damage Characterization in Standard Patterning 78
2.2.1. Morphological Instabilities 78
2.2.2. Chemical Degradation 85
2.2.3. Cross-Section Characterization 86
2.3. Simulations 89
2.3.1. Finite Elements Simulations 89
2.3.2. Interaction Volume and Phonon Distribution Simulation 91
2.3.3. Thermal Spike Model Calculation and Experimental Validation . 94
2.4. Interlacing Strategy Characterization 101
2.4.1. Morphological Stability 103
2.4.2. Chemical Stability 105
2.4.3. Material Related Effects 107
2.5. Applications 109
2.5.1. FIB Structuring of Polymers 109
2.5.2. TEM Lamella Preparation of an Organic Thin Film Transistor . . 111
2.5.3. TEM Lamella Preparation of a Layered Polymeric Sample 113

3. Summary 116

A. Curriculum Vitae I

List of Figures

1.1. Schematic illustration of a DBM 1
1.2. Resolution capabilities of microscopes 2
1.3. Tungsten hairpin 4
1.4. Lanthanum hexaboride elecrode 5
1.5. Field emission gun 5
1.6. Working principle of an FEG and the Wehnelt cylinder 6
1.7. Illustration of the spherical abberation 7
1.8. Illustration of the chromatic aberration 8
1.9. Working principle of a FEG and the Wehnelt cylinder 8
1.10. Interaction volume simulation for 5 kV electrons 9
1.11. Elastic and inelastic scattering 9
1.12. Electron beam heating effects 11
1.13. Typical hydrocarbon conatamination 13
1.14. Energy distribution of primary elelctrons 14
1.15. Everhardt-Thornley detector 14
1.16. Typical EDX spectrum 15
1.17. Liquid metal ion source 16
1.18. Illustration of an ion column 17
1.19. Cross-section of a TEM 22
1.20. Elastic and inelastic scattering 22
1.21. EDX detector 23
1.22. TEM with EELS detector attached 25
1.23. Electron energy loss spectra 26
1.24. Schematic design of a tube scanner 28
1.25. Working principle of a tube scanner 28
1.26. Comparison of line profiles with a fine and dull tip 30
1.27. Influence of the opening angle and impurities on the edges of AFM measurements 30
1.28. Convolution of tetragonal tip geometry in comparison to radial tip geometry. 31
1.29. Tip damage shown on calibration standard. 31
1.30. Position sensitive detector 32
1.31. Lennard-Jones potential 33
1.32. Illustration of the contact mode 34
1.33. Piezo excitation and amplitude and phase at resonance frequency 35
1.34. Tip damping after approach 36

1.35. Basic principle of the phase mode 37
1.36. Basic principle of the Kelvin Probe force microscopy 39
1.37. Characteristic Raman group frequencies 40
1.38. Electromagnetic radiation vector and amplitude 41
1.39. Absorption of electromagnetic radiation 42
1.40. Rayleigh and (anti-) Stokes scattering 43
1.41. Raman scattering process 44
1.42. Molecular motions of a water molecule 45
1.43. Raman active vibrations of nitrate and sulfate 46
1.44. Symmetry operations for water 46
1.45. Grating-based monochromator 47
1.46. Interferometer 48
1.47. Sample arrangements 49
1.48. Knife and sample holder of an ultramicrotome 50
1.49. Glass and diamond knife 51
1.50. Inclination between knife and sample 51
1.51. Polymer example 53
1.52. Branched, linear and terminal parts of a polymer 54
1.53. Dendrite structure 54
1.54. Structural isomerism 55
1.55. Stereoisomerism at polybutadien 55
1.56. Stereoisomerism at polypropylene 55
1.57. Conformal isomerism 56
1.58. Statistic copolymers 57
1.59. Alternating copolymers 57
1.60. Blockcopolymers 57
1.61. Volume change at T_g and T_m 58
1.62. Network of hydrogen bonds in polyamid 60
1.63. Semicrystalline polymer 62
1.64. FEI NOVA 200 nanolab 64
1.65. Used DBM 65
1.66. Comparison of serpentine and interlacing strategy 66
1.67. Standard TEM lamella preparation 67
1.68. AFM used 68

2.1. Chemical formula and DSC of PP and HDPE 73
2.2. Chemical formula and DSC of PP and HDPE 75
2.3. Light microscopy image of PEO 76
2.4. Chemical forumla and DSC of EVA 77
2.5. Chemical forumla of PS 78
2.6. Milling depths and side wall angles 79
2.7. Removal rate vs. beam dwell time experiment on PP 81
2.8. Removal rate vs. beam dwell time experiment on PP at RT and CT . . . 81
2.9. Removal rate vs. point pitch for PP and different DTs 83

2.10. Polymer comparison of removal rate experiments 84
2.11. Raman summary for polypropylene 85
2.12. Raman summary for HDPE, EVA and PMMA 86
2.13. AFM height images of ultramicrotomy cuts 87
2.14. Polished cross-section 88
2.15. FEM simulation of the surface temperature 90
2.16. Saturation of temperature at multi-point simulations 91
2.17. Interaction volume and energy transfer 93
2.18. Interaction volume and energy transfer 95
2.19. Calculated surface temperature distribution 97
2.20. Calculated surface temperature distribution 98
2.21. Calculated temperature distribution for PMMA and HDPE 99
2.22. Temperature accumulation 101
2.23. AFM height images with regular and interlacing strategy 102
2.24. Concept of interlacing 102
2.25. Interlacing point pitch variation 103
2.26. Smart interlacing strategy 104
2.27. Interlacing point pitch variation 105
2.28. Comparison of Raman integral intensities at RT and CT 106
2.29. Comparison of Raman integral intensities for HDPE and PMMA 106
2.30. Material related effects comparison of HDPE and PMMA 108
2.31. Material related effects comparison of HDPE and PMMA 110
2.32. Cross sectional scheme of an OTFT 111
2.33. TEM image and t/λ map of the OTFT lamella 112
2.34. HAADF and EFTEM image of the OTFT 113
2.35. TEM image and relative thickness map of the final OTFT 114
2.36. Fully polymeric layered structure 114
2.37. STEM image and EELX / EDX analysis of polymeric layered structre . . 115

3.1. Comparison of classical and interlacing patterning strategy 119

List of Tables

1.1. Brighness of different electron sources 4
1.2. Comparison of typical tip and cantilever properties 29
1.3. Different forces acting between the tip and the surface at different distances 32
1.4. Linear substituents influence on T$_g$ 63
1.5. Embedding materials used for ultramicrotomy cuts. 70

2.1. Calculated maximum temperatures for differen polymers 89
2.2. Simulated radial and longitudinal interaction volume 92
2.3. Simulated energy transfer 94
2.4. Material properties used for thermal spike calculations and maximum temperature 96
2.5. Radial and depth values for volatized and modified regions for all polymers 98

Introduction and Motivation

During the last few decades focused ion beam (FIB) processing has developed into a well-established tool for site-specific preparation of ultrathin lamellae for transmission electron microscopy [4, 11, 26]. But it has also attracted enormous attention as a method for (analytical) 3D metrology and 3D surface structuring from the micro- to the nano-scale [4, 11, 26, 38]. Beside these central points, the highly flexible direct-write character and, furthermore, the ability to design subtractive 3D structures with spatial nanometer resolution even on non-flat surfaces makes this method particularly important for prototyping applications in science and technology [4, 18, 22, 30, 35, 46, 47, 49]. However, beside these undoubted advantages of FIB processing, problems arise such as spatially confined ion implantation [11, 26], surface amorphization [4, 22, 27, 34, 35, 49] and partial high thermal stress [29, 44, 49]. Ion implantation and surface amorphization are intrinsic properties for the ion-sample interaction and are therefore invariable for a specific set of parameters. On the other hand, the in part enormous local heating effects may alter the morphology and / or damage the chemical structure of sensitive samples, such as nano-scale devices, thin films or materials with low melting points such as polymers and biological samples [13, 44, 52].

A possibility for decreasing this thermal stress is the use of a low temperature stage down to liquid nitrogen temperatures. The successful application of such stages was impressively demonstrated for polymer samples, compounds and biological materials [24, 25, 29, 31, 42, 43]. Another, more straightforward strategy for a thermal stress reduction is a careful adaption of process parameters, primarily via an ion beam current decrease and reduced dwell times in the microsecond range and below, as Gianuzzi et al. [11] impressively proved. Furthermore, Kim et al. [17] demonstrated a relation between the chemical damage and the ion beam doses used on thin films of PS-b-PMMA block copolymers. They almost eliminated the chemical damage by using low ion beam current and low sample temperatures of - 100 °C. Furthermore, Bassim et al. [6] revealed the decrease of chemical damage by an increased point-to-point distance of consecutive pattering points, which proves the influence of a variety of FIB process parameters on the chemical damage. These influences were already reported in literature by some authors [7, 19], but only a few include different patterning sequences of the FIB processing. Due to the fact that high temperatures can induce phase transitions, interdiffusion, melting, creeping and chemical degradation [32] for soft materials, FIB has often been considered to be very complicated or even incompatible in combination with sensitive samples, such as polymers, biomaterials or nanoscale devices.

In this thesis, we explore new pathways of FIB processing which re-opens the door for use with sensitive and / or low melting materials. Beside the careful adaption of primary process parameters, the central part of this thesis deals with additional heating effects introduced by the classically-used patterning strategies such as raster or serpentine procedures. In particular, the influence of the patterning strategy on morphological and chemical stability is investigated [39] in detail followed by the introduction of an alternative patterning strategy leading to drastic reduction of thermal effects during FIB processing. To fully understand and push this technique further towards its full capabilities, it is indispensable that a very close look be taken at local temperatures and their spatial and temporal evolution [40]. Different ways of local temperature estimation and calculation as well as its spatial evolution on the processing time scale have been applied in the past. One semi-empirical approach introduced by Volkert et al. [49] estimates the steady-state temperature using $T = P/(\pi\alpha\kappa)$ with α as the beam radius, P the beam power and κ the thermal conductivity of the sample. With this approach a maximum temperature can be estimated, but the spatial and temporal evolution is not accessible.

By using the thermal spike model, as shown by Vineyard et al. [48], the spatial and temporal aspects can be included. This method has gained more and more importance due to the increasingly powerful simulation hardware and due to the fact that different physical problems have been modeled, especially the study of the thermal properties of irradiated materials. A detailed correlation between theoretical and experimental results of the thermal spike model in pure crystalline metals has successfully been demonstrated by Wang et al. [50]. Also, Dufour et al. [8] have described the evolution of latent track radii on the basis of the thermal spike model using the electronic stopping power S_e as a new and successful approach. Both strategies have obtained very good agreement between theoretical calculations and experimental data. Another successful application of the thermal spike model was performed by Amirkhanov et al. [5] who modeled a two-layer material system and estimated the local melting regions in the target material. There are many more studies confirming the reliability and applicability of the thermal spike model for modelling inorganic materials and compounds, but to the best of our knowledge, it has never been used for the description and prediction of the behavior of soft matter such as polymers as is successfully introduced in this thesis in the second main part.

In the first part of this thesis, the thermal spike model is used for the simulation of the temporal temperature evolution with a laterally resolved character and the findings are compared with experimental results, as is also shown in [40]. Initially, the energy dissipation mechanism for FIB processing within the specimen will be discussed. The extracted data are then used as spatially-resolved input data for the thermal spike simulations, which give insight into the temporal temperature evolution of poly(methyl methacrylate) (**PMMA**) and high-density polyethylene (**HDPE**) as representatives of soft matter materials. They have been chosen due to the fact of their fundamentally different processes during heating, namely scissioning and cross-linking, respectively, as shown in detail by Orthacker et al. [32]. These simulation data are then compared with the FIB experiments revealing very good agreement and proving both the validity of the thermal spike model as well as the predictability, which ultimately allows for calculation-aided optimization of the process strategy.

The second part of this thesis has an of experimental character making use of the systematic variation of point pitches and dwell times as main process parameters. In this way, a technically-induced heating effect is identified,which is caused by the standard patterning sequences which massively alter and destabilize surface morphologies and chemically degrade the polymers used. Based on these findings, an alternative patterning strategy is introduced [39] which leads to a reduction of temperature effects towards the intrinsic and unavoidable limit given by individual ion-matter interactions. As will be shown, this alternative patterning strategy reveals a very high performance even for harsh patterning conditions on low melting polymers.

In the third and last part of tis thesis this alternative interlacing strategy is applied to the well-established application of TEM lamella preparation for materials with which massive problems habe been experienced during classical, though careful FIB processing. Specifically, ultrathin organic thin film transistors (OTFT) and soft material stacks (polymer-metal-polymer-polymer-polymer-printed OTFT) are demonstrated to be processable by this new approach without the typical problems of delamination or chemical interlayer mixing. Also, conventionals surface structuring is demonstrated by interdigital structures on low melting polymers, which is practically impossible to accomplish via classical strategies.

1. Fundamentals and Methodology

1.1. Fundamentals of Dual Beam Microscopy

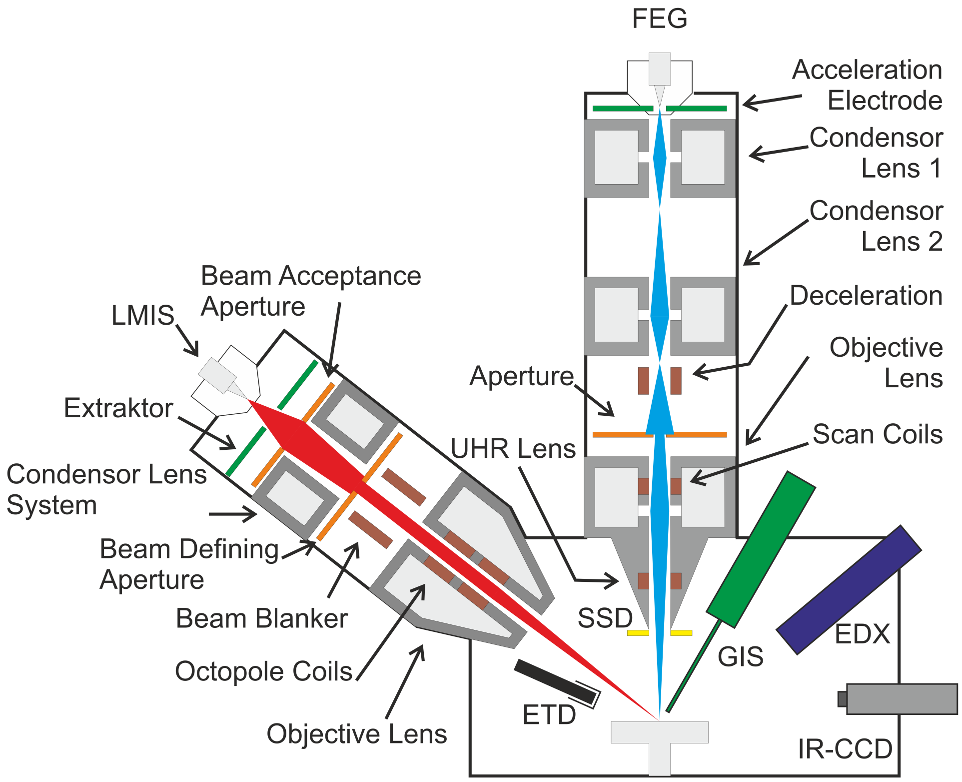

Figure 1.1.: *Schematic illustration of a dual beam microscope revealing the main parts: vertical electron column and the tilted ion column (both with emitters, extractor/accelerationo electrode, lens and aperture systems).*

The integration of a focused ion beam (**FIB**) expands the usefulness of a conventional scanning electron microscope (**SEM**), forming a dual beam microscope (**DBM**). By using a particle beam in combination with a patterning engine and focusing it onto the surface, very complex and 3-dimensional structures can be fabricated. This has found application in the fields of rapid prototyping, nano-electronics and the fabrication of functional surface structures. Another very important application is the investigation of Cross-sections, which allows a view underneath the sample surface, as well as site-specific TEM lamella preparation as an essential part in research, development or failure analysis. Beside this negative structuring, positive nanostructures can be produced by using special precursor gases in combination with either focused-electron beams or focused-ion beams.

Due to the countless and unique facilities, the complex platform and the in-situ control enabled by the dual beam system, a DBM is often referred to as a nanolab and is an essential part of modern science in a diverse range of research areas. The fundamentals of DBMs will be discussed in the following sections. A schematic illustration of a DBM is shown in Figure 1.1 revealing the main parts of the microscope.

1.1.1. Scanning Electron Microscopy

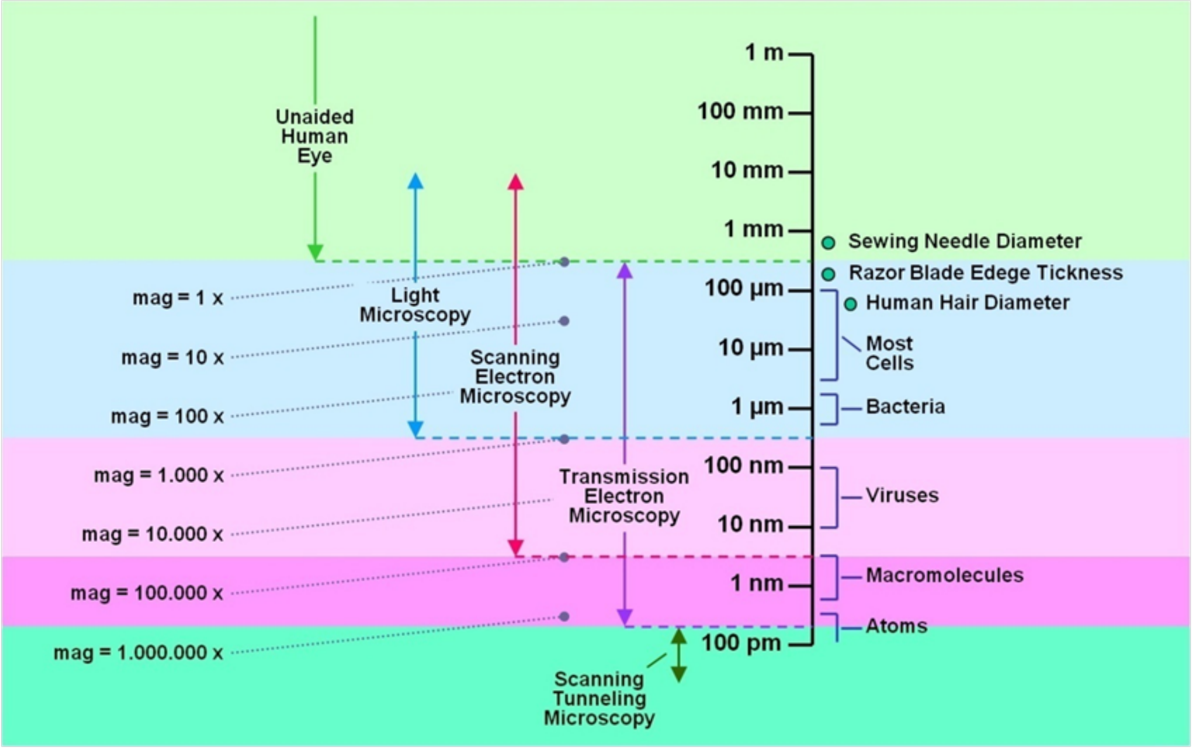

Figure 1.2.: *Resolution capabilities of different microscopy techniques starting with the naked human eye, ending with the transmission electron microscope and the scanning tunneling microscope enabling sub-atomic resolution.* [12]

A scanning electron microscope uses a finely focused electron beam for imaging a sample surface by systematic scanning. Electron microscopes are superior compared to optical microscopes due to their short wavelength used, allowing lateral resolutions down to 5 Å thereby making it one of the highest resolving microscopy techniques as summarized in Figure 1.2. The resolution limit δ itself is described by the Rayleigh criterion:

$$\delta = \frac{0.61\lambda}{\mu sin(\beta)} \rightarrow \delta \approx \frac{0.61\lambda}{sin(\beta)} \tag{1.1}$$

with λ being the electron wavelength (e.g. in the range of 0.04 Å for 100 kV) and β the opening or convergence angle. The resolution limiting factors are discussed in section 1.1.1.2 and are mainly related to lens imperfections.

Typically, bulk specimens are analyzed in a SEM where the electrons are not able to transmit through the material. Hence, detectable species are re-emitted from the surface as electrons with different energies and X-ray photons, giving topographical, structural, chemical and in part, functional information, such as electric conductivity.

In general, a SEM consists of the electron source, electron lenses and detectors, which will be described in the following sub-sections.

1.1.1.1. Electron Source

First of all, there must be an electron source that generates an electron probe, which is demagnified and subsequently focused through the lens system. This electron source can be established by different arrangements of electron guns. Various effects are responsible for electrons being emitted and the three main types of sources are discussed below. A characterizing factor of these emission tips is the brightness describing the current density per unit solid angle:

$$\beta = \frac{i_e}{(\pi d_0 \alpha_0)^2} \tag{1.2}$$

where d_0 is the beam diameter at the crossover, α_0 is the semi-angle of divergence from a source and i_e is the cathode emission current. A comparison of the different electron sources´brightness is shown in Table 1.1.

Tungsten Hairpin: This is the most common type of electron source, in which a tungsten hairpin filamentis used, shown in Figure 1.3, that is heated by causing a current

Table 1.1.: *Comparison of brightness for different electron sources in electron microscopes.*

Electron Source	**Brightness** [A/m^{2}sr]
Tungsten Hairpin	10^8
LaB$_6$	10^9
Schottky Emitter	$5 * 10^{10}$
Cold FEG	10^{13}

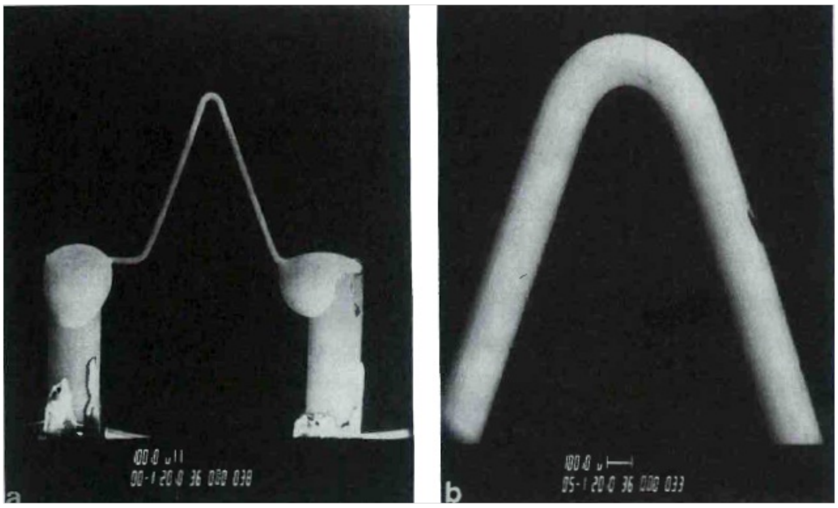

Figure 1.3.: *Tungsten hairpin acting as a thermionic electron source [12].*

to pass through the filament reaching up to 2500°C. This heating leads to a thermal emission of electrons from the tip of the filament. The filament is about 0.1 mm thick and in comparison to the other sources, it is not expensive. The advantage of such guns is their good stability at high current, making them preferable for X-ray measurements, whereas the coarse tip size and the short lifetime are major drawbacks.

Lanthanum Hexaboride Electrode: This type of electron source consists of a heated block of LaB$_6$, as can be seen in Figure 1.4,is also operated by means of thermionic emission. However, in comparison to the tungsten hairpin, the LaB$_6$ filaments have a larger maximum beam current and an increased brightness, since LaB$_6$ has a lower work function than tungsten. Another advantage is the beneficial source size as well as the decreased energy spray compared to the tungsten hairpin.

Field Emission Gun: The field emission gun (**FEG**) has a different working mechanism than the first two types of electron sources. It is also formed by a very fine tungsten tip

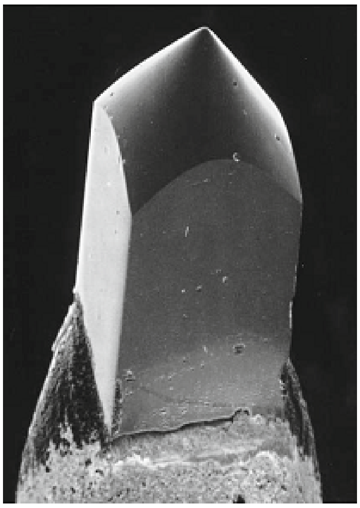

Figure 1.4.: *SEM image of a* LaB_6 *crystal as an electron source [53].*

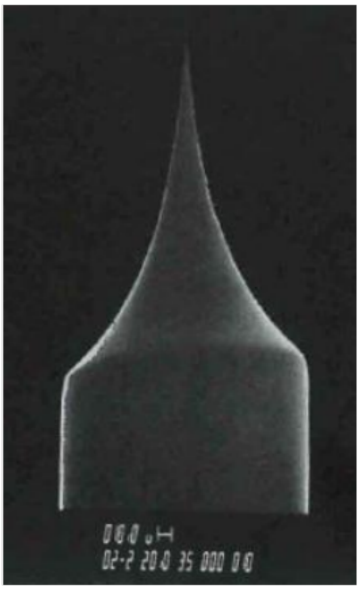

Figure 1.5.: *SEM image of a tungsten tip acting as a field emission gun [12].*

with a tip radius of approximately 0.1 - 1 μm there are three different working principles: a cold FEG, a thermally-assisted FEG and a Schottky emitter. Such a FEG can be seen in Figure 1.5. The cold FEG is not heated and it is only when an external electrostatic field is applied that the electrons can tunnel through the potential barrier and leave the tip, whereas with the thermally-assisted FEG, the tip is heated up to approximately 1800°C, which induces the electron emission. A Schottky FEG is further coated with an additional ZrO_2 layer, decreasing the work function from 4.5 eV for tungsten to 2.7 eV for ZrO_2, thereby enhancing emission. This coated type of electron gun increases the stability in comparison to a cold FEG, thus resulting in an enhanced lifetime, whereas the cold FEG provides the greatest brightness. A drawback of this type of tip is that a vacuum better than 10^{-10} Torr has to be provided at the gun, whereas a thermionic emitter only needs 10^{-6} Torr.

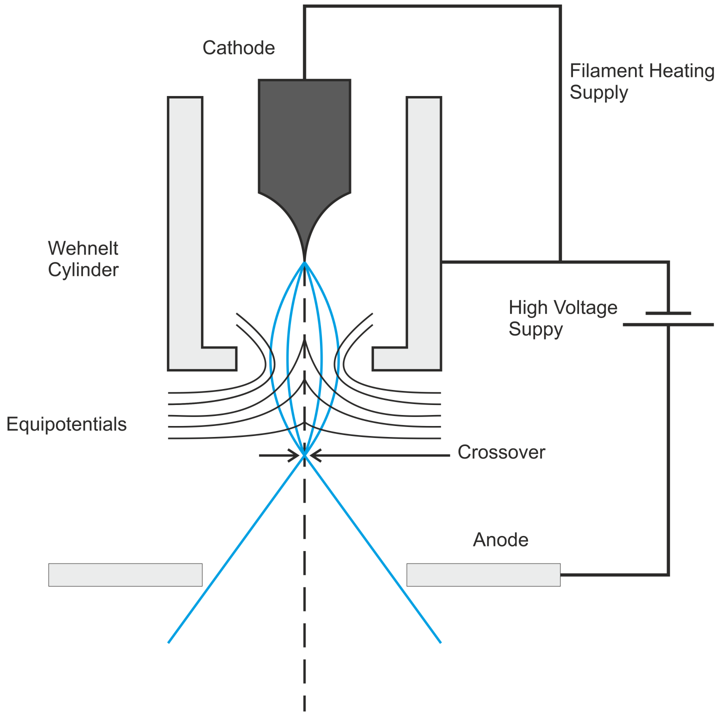

Figure 1.6.: *Schematic illustration of the working principle of an FEG with the Wehnelt cylinder and the first crossover.*

The electron source is situated inside a Wehnelt cylinder, which is a special construction in order to provide the crossover d_0, which is the point where the electrons are focused initially. To achieve this, a negative voltage is applied to the Wehnelt cylinder, followed by anode plates, which are responsible for the acceleration of the electrons up to an energy of typically 30 kV for an SEM. The general scheme of such a cylinder is shown in Figure 1.6.

1.1.1.2. Electron Column

Basically, an electron column consists of two or three electromagnetic condenser lenses which demagnify the electron probe focused at the crossover. The scan coils are the second main part of the column and are responsible for the raster-like motion of the electron beam over the sample. Such an electron lens is made of coils with an axial magnetic field with rotational symmetry. The minimum achievable beam diameter is limited by aberrations and not by the wavelength and these aberrations can be partly corrected. The most important of these, spherical aberration, chromatic aberration and astigmatism are discussed below.

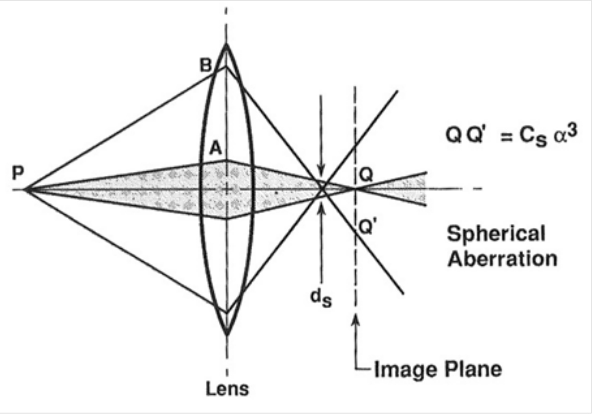

Figure 1.7.: *Illustration of spherical aberration [12].*

Spherical Aberration: This effect occurs when electrons pass the lens at different distances from the optical axis. Due to a different bending of electron trajectories on and near the axis and further away from the optical axis of the lens, there is no convergent focal distance for all of the electrons, as can be seen in Figure 1.7. A correction of this aberration can be achieved with a special multi-pole lens and can be found in virtually all modern, high-end transmission electron microscopes. Alternatively, this aberration can be decreased by the use of a small aperture, which has the drawback of small electron currents.

Chromatic Aberration: Chromatic aberration is an effect caused by different refractive indices for different wavelengths and therefore varying electron energies. For lower energetic electrons, the focal plane will be closer to the lense than the focal plane of higher energetic electrons, resulting in a beam blurring, as revealed in Figure 1.8.

Astigmatism: Due to mechanical errors, magnetic inhomogeneity of the polepieces and asymmetry in the windings, the electromagnetic lenses do not exhibit perfect rotational symmetry. This results in a shift of the focal plane of vertical and horizontal lines at two different distances, thus creating an elliptically shaped deformation of circular structures, as illustrated in Figure 1.9. This aberration can also be corrected using additional lenses.

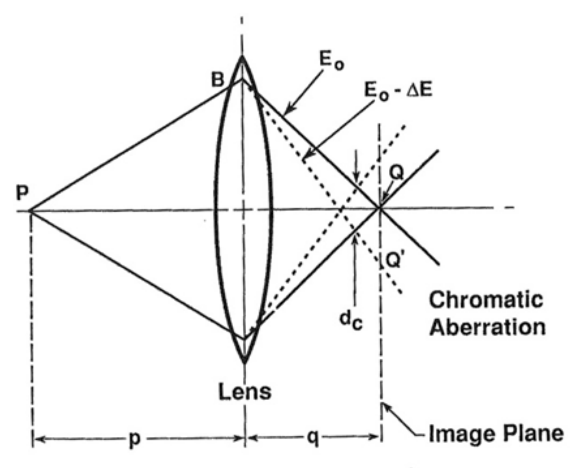

Figure 1.8.: *Illustration of chromatic aberration [12].*

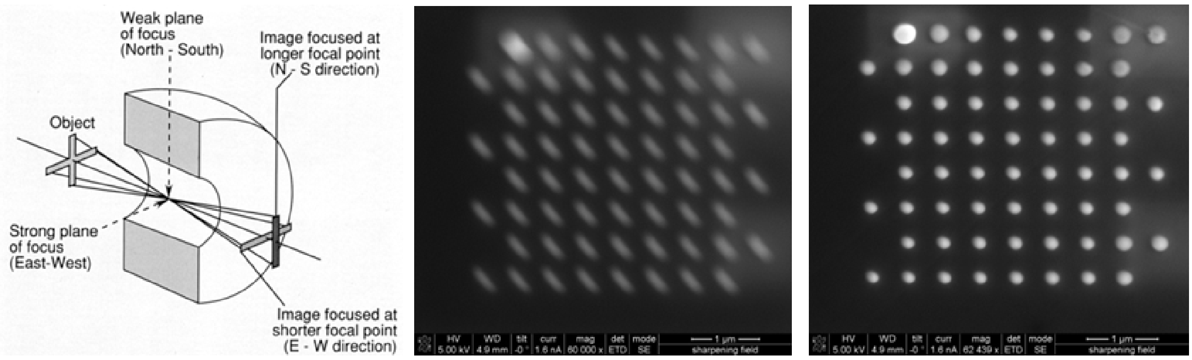

Figure 1.9.: *Illustration showing astigmatism (left [12]), an uncorrected SEM image of a focusing pattern (middle) and a focusing pattern with astigmatism corrected(right).*

1.1.1.3. Electron Beam – Sample Interaction

Electrons which are impinging on the sample can be scattered elastically and inelastically. Both of these processes disturb the direction of propagation, which, in combination with the statistical character of this process, leads to a drop - shaped interaction volume, which may extend from less than 100 nm up to 7 μm into the surface depending on the primary beam energy. A typical Monte Carlo simulation of interaction volume for 5 kV of primary beam energy is shown in Figure 1.10, revealing different types of electrons. Some may be scattered back out of the sample, shown in red, and some becine stuck inside the specimen, indicated in blue. These two scattering processes, elastic and inelastic, will be discussed below and schematically illustrated in Figure 1.11.

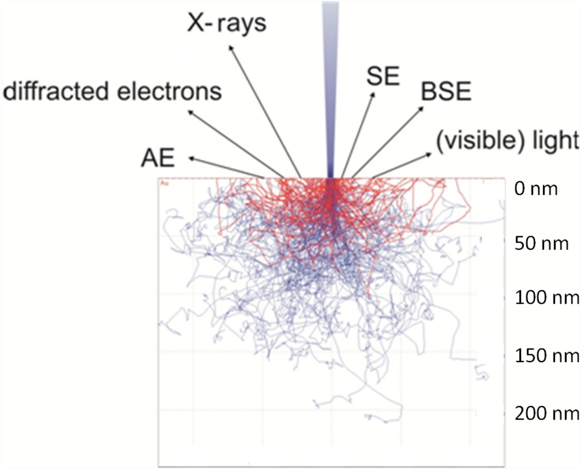

Figure 1.10.: *Interaction of the 5 kV electron beam with the sample visualized using a Monte Carlo trajectory and interaction simulation.*

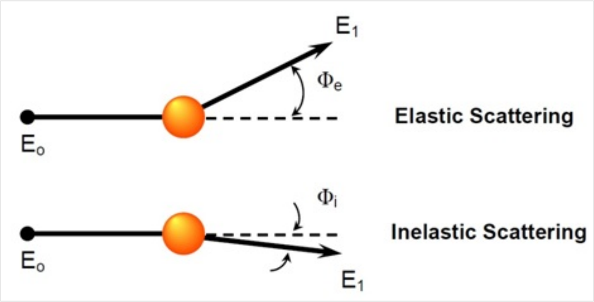

Figure 1.11.: *Schematic illustration of the elastic and inelastic scattering processes [41].*

Elastic Scattering: Electrons are deflected through the atomic nucleus coulomb field with no loss of energy by an elastic scattering process. This type of scattering is characterized by a high angle of deflection. Due to this high-angle scattering, the probability of being scattered back out of the sample is increased. These electrons are called "back scattered electrons" (**BSE**).

Inelastic Scattering: In contrast to the elastic counterpart, the electrons are not only scattered into smaller angles, but also lose part of their energy to one of the following processes: The energy can be transferred to molecule oscillations or phonons, which produce heat. Another process is the ionization of inner atom shells, which are refilled by electrons from outer shells, producing characteristic X-rays. This allows for qualitative and quantitative analysis of the chemical composition. This energy loss is in the range of 50 eV - 100 eV. Furthermore, a release of outer shell electrons through an energy transfer of 50 eV and less is also possible. These free electrons are then called ”secondary electrons” (**SE**).

1.1.1.4. Electron Irradiation Damage

Several different effects can be distinguished: electrostatic charging, ionization damage (radiolysis), displacement damage, sputtering heating and hydrocarbon contamination. Generally, the amount of electron beam damage is proportional to the electron dose, but the range of damage depends on the amount of energy deposited in the specimen. These effects will be discussed below.

Electrostatic Charging: Electrostatic charging means the accumulation of surface charges on the sample, but also inside the specimen. The charges cannot leave the sample to an electrical ground, due to low electrical conductivity or a bad contact. This effect of electrostatic charging depends on the net charge overrun inside the sample, which depends on the backscattering coefficient (η) and on the secondary electron yield (δ); thus both elastic and inelastic scattering are involved.

In general, electrically non-conducting or low-conducting samples must be prepared using a conducting coating. This can be simple a carbon coating but also Pt, Au or a mixture with Pd and many other elements can be used. The objective is to eliminate charging artifacts, which can be observed as irregular, featureless bright patches or streaks and cause a decreased resolution.

Atomic Displacement: This effect arises when the electron energy overcomes the displacement energy. This is a property of the specimen material and is influenced, for example, by the bond strength, crystal lattice and the atomic weight of the constituent atoms, and it produces vacancies, such as Frenkel defects. Although in elastic scattering the electron conserves its energy, momentum can be transferred to the nuclei of the host atoms which can be knocked out of their original position (knock-on damage). Due to the high energy required, such as for a carbon atom in the diamond structure, the displacement energy is approximately 80 keV while the threshold energy of the incident electrons is approximately 140 keV. As the highest possible primary energy is 30 kV during FIB processing the effects described are only relevant during TEM investigations [9].

Electron Beam Sputtering: Electron beam sputtering is similar to atomic displacement, but only occurs when the energy transfer from an electron to the atom exceeds the sublimation energy threshold of the atom, which is much higher than the displacement energy. The result is that the atom is knocked out of the sample. This energy threshold for electron beam sputtering is also dependent on the atomic number (Z) and is thus most likely for elements with a low atomic number. In order to avoid this effect, only the use of low-dose or a very thin, heavy element coating as a protection layer is practical.

Electron Beam Heating: The primary electrons lose part of their energy by colliding with specimen electrons during the inelastic scattering process. Within the sample, a considerable part of this energy can be converted into heat and result in a local temperature increase. Thermal damage of the electron beam is not a serious problem; because of the thermal conductivity and the small energy deposition, only a minimal temperature increase is caused by the electron beam. As can be seen in Figure 1.12, the temperature calculation by Hobbs [14] states that the temperature increase is negligible under standard conditions for metals and other good conductors, but may become substantial for insulators.

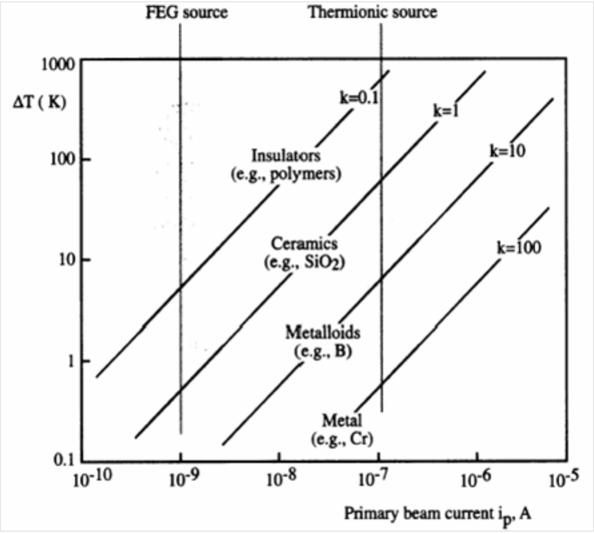

Figure 1.12.: *Schematic illustration of electron beam heating effects [14].*

Radiolysis (Ionization Damage): Impinging electrons can break bonds which may lead to dissociations of molecules. This is a result of an ionization process due to inelastic electron scattering. Especially for polymer samples, this radiolysis is of particular importance and causes severe problems. Due to the breaking of chemical bonds, whereby covalent bonds and Van der Waals bonds are present in a polymer, the molecule changes its shape and position, which affects the crystallinity and causes swelling or shrinking of the specimen.

A reduction of radiolysis may be achieved by coating the specimen with a thin metal layer. Also, an additional cooling to cryogenic temperatures may have some positive effects due to the temperature dependency of the ionization damage. This reduction of radiolysis by a temperature decrease results from a reduced sensitivity of organic specimens to structural damage and mass loss at lower temperatures, but is not a consequence of a varied inelastic Cross-section.

Hydrocarbon Contamination: Incoming electrons are able to polymerize hydrocarbon molecules on the surface of the specimen. These hydrocarbon molecules on the sample surface are virtually unavoidable due to the presence of hydrocarbons in the vacuum chamber of the microscope or because of silicon oils from the diffusion pump, which nowadays are usually replaced by ion getter pumps. Because of these two effects, there are always some residual hydrocarbon molecules, but the amount of these depends on the type of pumps and also on the samples which have been processed in this chamber. The most severe cause of hydrocarbon contamination is that the specimen is contaminated with hydrocarbons, which diffuse along the specimen surface. A typical example of hydrocarbon contamination can be seen in Figure 1.13, which shows the diffusion along the sample to the edge of image formation, where the molecules get immobilized and form the contamination.

Hydrocarbon contamination removal can be done with the assistance of a plasma cleaner, which can also be set up inside the specimen chamber in order to achieve faster processing times [3]. With this plasma cleaner, the specimen is exposed to ions, which cause a cleaning process. The second commonly used technique is a special cold finger inside the specimen chamber, where hydrocarbons and other residual molecules are trapped. Also, every instrument for charging reduction, such as coating or pre-cleaning, assists the avoidance of hydrocarbon contamination [9].

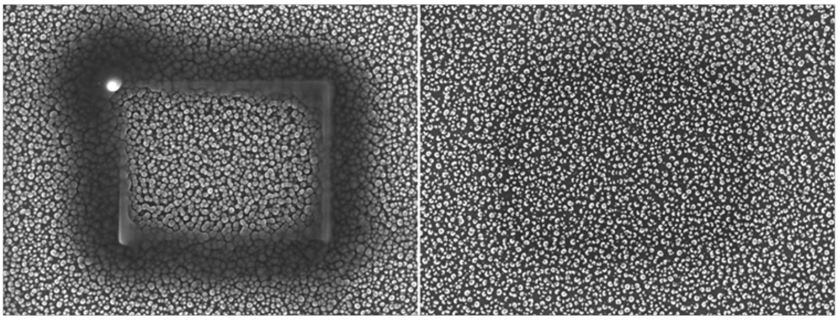

Figure 1.13.: *Typical hydrocarbon contamination showing two locations of a silicon grass sample irradiated for 10 minutes before (left) and after (right) the use of an EVACTRON® anti-contamination device with a field of view of 1 μm. [XEI Scientific, Inc.].*

1.1.1.5. Signal Detection and Imaging

The most important detectable signals induced by electron bombardment are the characteristic X-rays, backscattered electrons (**BSE**) and secondary electrons (**SE**). Beside these, plenty of other signals can be detected, such as the electron beam induced current, cathodoluminescence, voltage-contrast imaging or auger electrons, but these are beyond the scope of this thesis. Thus, in this section only the most important signal generation mechanisms for imaging are discussed.

Secondary Electron and Backscattered Electron Imaging: The most important signal for image acquisition is generated through secondary and backscattered electrons. The volume of the secondary electronsórigin is spatially very well confined to a zone near the surface and the primary electron beam, thus resulting in the best resolution. See Figure 1.10for an illustration of the interaction volume. These secondary electrons are energetically defined as electrons below 50 eV (see Figure 1.14 for energetic distribution of electrons) and they are generated by the inelastic scattering processes of knocking electrons out of sample atoms. The signal generated by this type of electron shows only topographical information, but no material differentiation is possible. The other possibility of signal generation is that of backscattered electrons, which are primary electrons that get scattered back out of the sample mainly by the elastic process. The volume generated compared to the secondary electrons is much more extensive, resulting in a loss of resolution, but the advantage is a material dependence of BSE yield. Thus, material differentiation is possible. The BSEs are characterized by energies higher than 50 eV

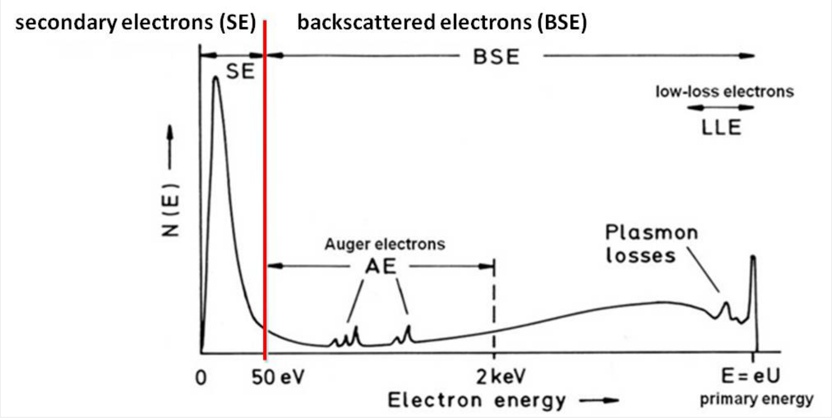

Figure 1.14.: *The energy distribution of electrons produced by the primary electron beam is shown [36].*

Typically, an Everhart-Thornley detector (**ETD**), see Figure 1.15, is used for SE and BSE imaging. This detector consists of a grid for the collection of low energetic electrons. Due to the application of a different voltage on this grid, either SE or BSE can be detected. Behind this grid a scintillator generates photons out of the impinging electrons, which are led through an optical fiber to a photomultiplier. There an electrical signal is generated in dependence on the number of impinging electrons, whichproduces a gray-scale image. As the SE detector is situated on one side of the specimen chamber, edges and planes facing the detector will appear brighter, whereas structures facing in the opposite direction will remain darker. This leads to a topographical contrast. In BSE imaging, the material contrast is achieved by dependence on the atomic number, which leads to a qualitative differentiation.

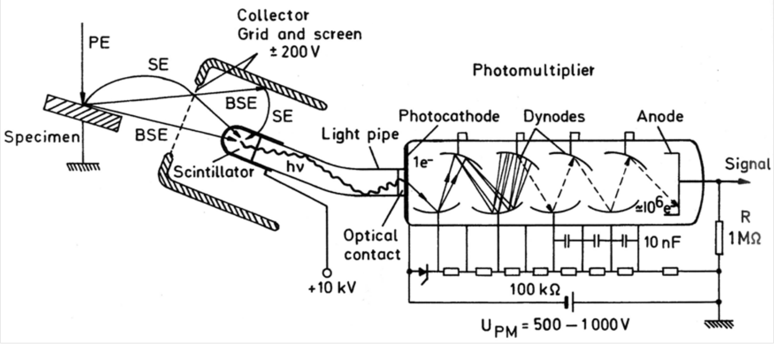

Figure 1.15.: *Schematic illustration of an Everhardt-Thornley detector [12].*

A second possibility for electron collection uses a so-called through-the-Lens detector (**TLD**), which is situated in the lowest part of the electron column. This results in a different angle of observation, suppression of the morphological shadowing effects and a high resolution for special investigations. The TLD is also advantageous for investigations of deep high-aspect-ratio structures, allowing a better insight at the bottom of the structure.

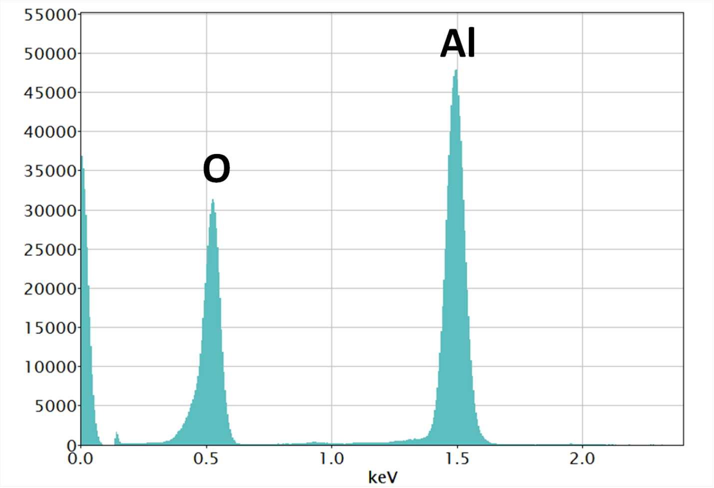

Figure 1.16.: *Typical EDX spectrum with oxygen and aluminum peaks revealing the chemical composition by means of characteristic x-ray peaks for different elements.*

X-Ray Detection: The signal detected from characteristic X-rays is generated as the impinging electron beam knocks out inner shell electrons which are then filled by an electron from a higher energy level. This results in a qualitative and quantitative determination of the chemical composition of the sample. The volume of signal generation compared to SE and even BSE is increased, leading to a loss of resolution. Due to the fact that each atom has different energy levels in their electron shells, this transition results in the emission of X-rays that are characteristic for each material. A typical spectrum of a material containing mainly oxygen and aluminum is shown in Figure 1.16.

A silicon drift detector (**SDD**) can be used for X-ray detection, which consists of a thin Si wafer of approximately 0.3 - 0.5 μm thickness. An impinging X-ray photon generates electron-hole pairs on this wafer. The number of electron-hole pairs generated is proportional to the energy of the impinging photon. The detector geometry induces an electron drift to a central point, where a current can be detected, which is proportional to the photon energy. Via the thin window, a very fast response rate with low noise and high sensitivity is achieved. This detected current is used for gate regulation of a field effect transistor, which amplifies the signal.

1.1.2. Focused Ion Beam Microscopy

Focused ion beam (**FIB**) microscopy is a very versatile technique which is used mainly in semiconductor and materials science for many applications, such as imaging, milling, deposition, site-specific analysis, micromachining, but also for specimen preparation, especially for TEM, of materials. When combined with other analytical instruments, such as an SEM, the possibilities are further increased.

The basic working principle is quite similar to that of an SEM, but the main difference is the beam used to scan over the sample. As an ion beam is used, typically Ga^+ ions, the particle mass and its momentum is much higher than with electrons, which leads to local milling. Also, the vacuum system consists of two different pumping regions, one for the column and one for the sample chamber, ensuring approximately 10^{-8} Torr in the column to prevent electrical discharges and avoid source contamination. High vaccum in the chamber, on the order of 10^{-6} Torr, is essential for maximizing the mean free path of the beam on its way to the sample, because otherwise a resolution break down results.

1.1.2.1. FIB Sources

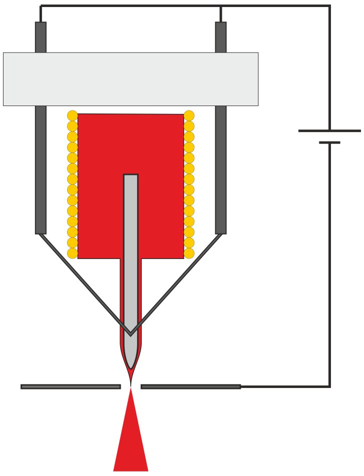

Figure 1.17.: *Schematic illustration of a liquid metal ion source with its gallium reservoir surrounded by heating coils. Liquid gallium flows around a metal tip forming the Taylor cone due to the voltage at the extraction cathode.*

A liquid metal ion source (**LMIS**) is typically used, which consists of a fine tungsten needle with a radius of approximately 2-5 μm and is attached to a reservoir of the metal source material; see Figure 1.17. Most commonly, Ga is used for the following reasons: (i) the low melting point of 29.8°C minimizes the interdiffusion between the tungsten needle and the liquid, (ii) the long source lifetime due to the low volatility of gallium at the melting point (T_m), (iii) the viscous behavior on the tungsten needle due to the low free energy at teh surface, (iv) the ability to use pure Ga because of the low vapor pressure, instead of an alloy source, (v) the excellent mechanical, electrical and vacuum properties and (vi) the high angular intensity due to the emission characteristics of Ga, which allows a very small energy spread.

This reservoir is heated by a coil up to the melting point of the material. The melt wets the tungsten needle due to its liquid behavior and, by applying an electric field via the extractor electrodes, a so-called Taylor cone is formed. This causes ionization and field emission of the gallium atoms.

Typical currents achieved by this kind of source are in the low μA range ensuring a low energy spread and a stable beam. The lifetime is dependent on the amount of material in the reservoir and on the inherent material properties and is approximately 1000 hours.

1.1.2.2. Ion Beam Column

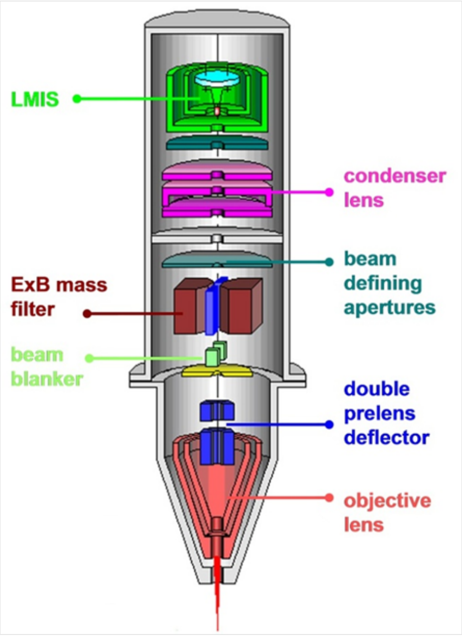

Figure 1.18.: *Illustration of the construction of an ion column [41].*

After the Ga^+ ions are extracted from the LMIS, acceleration to energies of up to 50 kV takes place. In contrast to the electron column, the FIB column, which is shown in Figure 1.18, uses electrostatic lenses for focusing the beam onto the sample. This type of lens is needed to provide sufficiently fast beam movement as a consequence of the much higher ion mass compared to electrons. A column such as this typically consists of two lenses, the condenser lens and the objective lens, which form the probe and focus it on the sample surface, respectively. The beam current can be regulated by an aperture from a few pA up to a few nA.

Due to the fact that the aberrations are the same as with an electron column, special cylindrical octopole lenses may be used for optimizing the performance with respect to beam deflection, alignment and astigmatism correction.

Another component in such an ion column is the E cross B (E×B) filter, which is used for selecting the ion species which are to be directed along a preselected path through the column. This is because the ion source contains some contamination from the material in the reservoir, or some contributions of other materials from the source. In an E×B filter like this, an electric field and a magnetic field is usually at right angles to the ion path leading causing a selection of ion species.

1.1.2.3. Ion Beam - Sample Interaction

When high energetic ions are impinging on the sample various interactions with the sample and also with sputtered material on the sample occur. These depend on the ion energy and can be separated into sputtering, amorphization, swelling deposition, redeposition, implantation, backscattering and nuclear reactions. High radiation damage is induced due to the fact that many effects of the impinging ions occur simultaneously, not only leading to morphological changes, but chemical and intrinsic physical properties (crystallinity, elasticity, conductivity, electrostatic charge, hydrophilicity, surface composition) are also modified or altered inside the interaction volume.

Depending on the material, this interaction volume is in the range of a few nm up to the order of hundreds of nm for 30 kV Ga^+ ions, which are most commonly used. Due to the fact that an ion is much heavier and thus has much more momentum than an electron, the penetration can be altered or hindered by the individual atoms of the sample and it loses energy and momentum due to interaction with these atoms. This energy and/or momentum loss causes atoms to vibrate out of their pristine position or even to break loose, which leads to a collision cascade. This collision cascade model is very widely accepted as a concept for ion-solid interactions. Thus, collisions can be seen as independent binary collisions within the material (binary collision approximation).

By exceeding the displacement energy during the energy transfer to a target atom, the atom is knocked out of its original position, which leads to the creation of interstitial vacancy pairs in a crystalline material. This knocked-out atom can have sufficient energy to create further collision cascades, thereby expanding the interaction volume. Collisions near the surface may force an atom to leave the sample, which is called sputtering.

The high energy which is transferred from the ion to the sample causes various processes, such as ion reflection and backscattering, electron emission, electromagnetic radiation, atomic sputtering and ion emission, specimen damage and specimen heating. These effects occur due to elastic and inelastic interactions. Elastic interactions occur by an energy transfer of ions to electrons in the sample leading to ionization and emission of both electrons and electromagnetic radiation. During inelastic interactions, energy is transferred to target atoms resulting in displacement, vibrations and removal of atoms (sputtering) from the sample surface. Because they lose their energy, the ions typically become stuck in the solid, which leads to an ion implantation. In the following sections, the primary mechanism of ion irradiation will be discussed.

Sputtering: The primary mechanism of material removal is sputtering. The sputter yield (**Y**) describes the number of ejected atoms per impinging ion. Y is increased by the ion energy and an increase in the angle of incidence also leads to enhanced sputter yields, with a maximum at 80°, however it decreases rapidly as the incident ange approaches 90°. The sputter yield is also dependent on the ion weights and the surface binding energies, in other words, on the target material.

To estimate the interaction volume and sputtering yield, a software package called SRIM/TRIM [1] is commonly used. It employs a Monte Carlo algorithm for the ion-target collision to calculate the stopping range of ions in matter. These calculations are in very good agreement with the experimental data. Further insight into this package and its algorithm is given in section 1.6.

Amorphization: If the energy transfer or the dose level of incident ions is not sufficient for sputtering of target atoms, amorphization of crystalline samples and swelling occurs. This amorphous phase is often metastable and dependent on the unit cell size and the complexity of the chemical ordering.

---

[1] Stopping and Range of Ions in Matter / Transport of Ions in Matter

This effect is of particular importance for the TEM lamella preparation of crystalline structures, as it leads to misinterpretation due to the very thin character of such samples and the extended amorphization zones for high energetic 30 kV ions. By lowering the ion energy, these amorphous zones can be spatially confined, which suggests a strategy of decreasing the ion beam energy incrementally for TEM lamella preparation.

Ga^+ Implantation: Because of the energy loss, the Ga^+ ions become stuck inside the specimen and are not scattered back. This region of contamination with Ga^+ ions extends the amorphous depth for low energies. Thus, a low energy removal of amorphous zones will also lead to Ga^+ implantation.

This implantation of ions influences the local composition of the specimen resulting in a concentration of up to 20 at.% of gallium several nanometers below the surface and still more than 2 at.% at a depth of up to 50 nm [16]. Furthermore alteration and structural changes are achieved by implanting ions, resulting in variations of thermal, electrical, optical or mechanical properties, for example.

The implantation of Ga^+ ions can also be used intentionally in a dual beam system, which can be a key parameter for FIB processing of microelectronic devices [51]. Here the ions are used as a dopant implanted into an Si substrate for the modification of conductivity.

For the reduction and prevention of unwanted implantation, a protective layer is often deposited onto the sample, first by focused electron beam induced deposition (**FEBID**) with a thickness of a few hundred nm, followed by a focused ion beam induced deposition (**FIBID**). For electron-sensitive materials, such as PMMA (see section 1.7) a different strategy must be applied for the sputtering of a protective layer, such as Pt/Pd.

Specimen Heating: A major part of the kinetic energy of impinging ions is converted into heat. At timescales larger than the order of nanoseconds and distances larger than approximately 100 nm, the ion beam can be seen as a continuous heat source. A good and fast temperature estimate is achieved by the following formula from [49]:

$$T = \frac{P}{\pi \alpha \kappa} \tag{1.3}$$

Here we have the beam power P, sample thermal conductivity κ, and α as the radius of the circular ion beam profile on the surface. According to this equation, the temperature can range from negligible to enormous values, depending on the samples thermal conductivity. The thermal effects take on particular importance for polymers, due to their low thermal conductivity and melting point; see section 1.7. A detailed discussion of specimen heating and temperature effects on polymers will be given in section 1.8.

Redeposition: Most of the sputtered material is pumped out of the specimen chamber by the pumping system. However, due to the fact of not being in thermodynamic equilibrium in the gas phase, the sputtered particles (neutral atoms and ions) tend to condense back into the solid phase on the sample surface forming redeposition near but also at the patterned area.

The extent of redeposition is dependent on the sticking coefficient of the removed material mixture and the relevant surface chemistry. Furthermore, the pattern footprint and in particular the intended aspect ratio, meaning the depth to lateral width ratio, is of particular importance. This can easily be understood by the fact that for high aspect-ratios the removal of sputtered material becomes very complicated and eventually stagnates entirely [45]. Since this effect is very complex, detailed knowledge about the sputtered particle chemistry, sputtering direction, mass charge and kinetic energy would be needed to optimize the FIB process parameters which are often inaccessible. Therefore, careful pre-tests are indispensable for estimating the unwanted contributions.

To remove artifacts of redeposition during TEM lamella preparation, a special polishing step is applied as a last step in the process. This is performed similar to the normal thinning procedure but with low ion energy, e.g. 5 keV, and low current, e.g. 70 pA [37].

1.2. Transmission Electron Microscopy

The transmission electron microscope (**TEM**) has been developed for structural and chemical analysis on the nanoscale and below. Figure 1.19 shows a technical cross-section scheme of a TEM which uses electron sources, similar to an SEM, like thermal emitters or field emission guns, where electrons are extracted and accelerated up to an energy of 300 kV. They are focused via condenser lenses into the sample plane as a spot beam (scanning transmission electron microscope - **STEM**) or as a parallel beam (conventional TEM). As the specimen is thin enough (10 nm - 100 nm) for electron transmission with

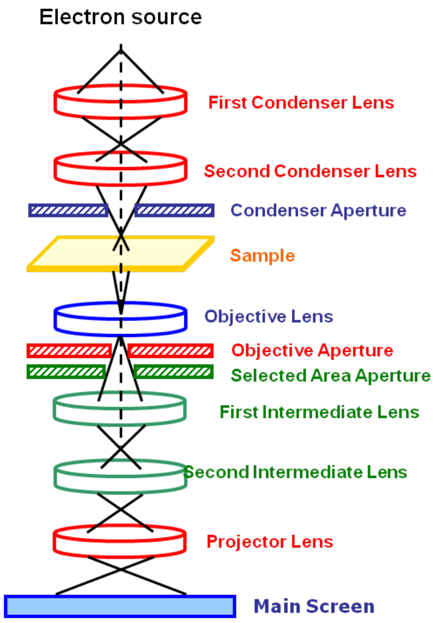

Figure 1.19.: *Cross-section illustration of a transmission electron microscope [41].*

single scattering events in ideal cases, the objective lens below the specimen generates an intermediate image of the sample with low magnification. This image is then magnified by the following lenses and displayed on a fluorescence plate or a CCD for digital image generation.

With this technique, atomic resolution is achievable in high resolution TEM mode, which allows the imaging of crystal lattices or defects. By electron diffraction, a full characterization of the crystal structure with high lateral resolution is possible. In this thesis, the main focus lies on analytical methods which use the inelastic scattered electrons (see Figure 1.20).

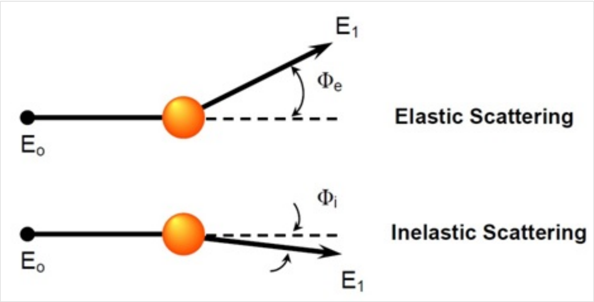

Figure 1.20.: *Comparison between elastic and inelastic scattering [41].*

This energy loss can either be detected directly via electron energy loss spectroscopy (**EELS**) or as a secondary process of a transition from an excited state to the ground state accompanied by the emission of X-rays using energy dispersive X-ray spectroscopy (**EDXS**). It is possible to use both methods for a laterally-resolved qualitative and quantitative analysis. The two techniques complement each other in that EDXS is more suitable for middle and high Z elements, whereas the EELS method is more appropriate for light elements.

1.2.1. Energy Dispersive X-Ray Spectroscopy

Energy dispersive X-ray spectroscopy is used for quantitative and qualitative chemical analysis. In this approach chemical information is obtained via the ionization of sample atoms caused by impinging, high-energy electrons. Filling this inner shell electron-free position with an outer shell electron leads to the ground state of the atom. The energy difference of the electron states can be emitted as a photon, which leads to the characteristic X-ray radiation. Due to the different energetic levels between the diverse shells, the energy of the X-ray radiation is dependent on the element and thus allows chemical analysis.

1.2.1.1. X-Ray Detectors

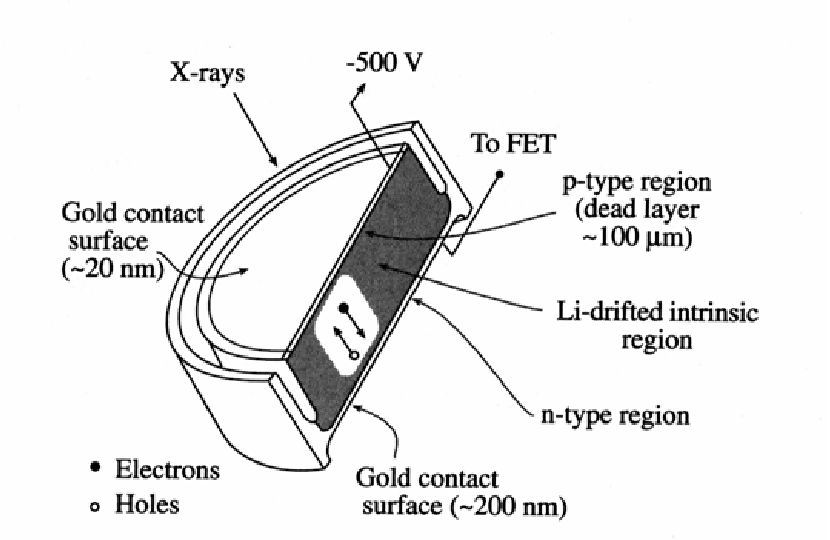

Figure 1.21.: *Schematic Illustration of an energy dispersive X-Ray detector [41].*

Most commonly used is a semiconductor detector made out of Si(Li) or high-purity Ge (HPGe). See Figure 1.21 for the setup of an EDX detector. These semiconducting materials are indirect semiconductors and possess a fully filled valence band and a largely unfilled conducting band. Impinging X-rays are able to excite electrons from the valence to the conduction band and thus increase the electrical conductivity. By applying a voltage, these generated electron hole pairs can be separated and conducted to the electrodes resulting in a bias. This signal is furthermore amplified, digitalized and shown as a spectrum.

1.2.1.2. X-Ray Spectra

In an X-ray spectrum both characteristic X-ray radiation and bremsstrahlung can be found. By means of the position of the characteristic X-ray peaks in the spectrum, an explicit and fast identification of elements (qualitative analysis) incorporated in the sample is possible. Via the intensity of the detected X-ray quanta, conclusions about the element concentrations can be drawn (quantitative analysis). Depending on the electron beam radius, sample areas in the nanometer range up to a few micrometers can be analyzed chemically. Figure 1.16 shows an example of an X-ray spectrum of a sample, revealing the bremsstrahlung and the chemical analysis via the characteristic position of the peaks.

A quantitative analysis of a sample can typically be done with an accuracy of a few percent, but is in general dependent on the elements incorporated in the sample. Generally, a detection sensitivity cannot be stated, due to its dependency on the measurement time, the analyzed element and the sample composition, but in most cases, elements down to 0.1 to 1 wt.% and in special cases even elements in the 100 ppm range can be detected.

1.2.2. Electron Energy Loss Spectroscopy

Beside EDXS, electron energy loss spectroscopy (**EELS**) is the second, powerful method for analyzing chemical compositions with (sub) nanometer resolution. Due to inelastic scattering, the high energetic electrons (60-300 kV acceleration voltage) which can pass through the < 100 nm thick sample lose part of their energy. For measuring the electrons which has lost some of their energy, an electron loss spectrometer is installed on the bottom end of the microscope. A schematic illustration of such an electron loss spectrometer is shown in Figure 1.22, which uses a magnetic field for separating the electrons according their energy loss and magnetic lenses for magnification to the CCD-detector.

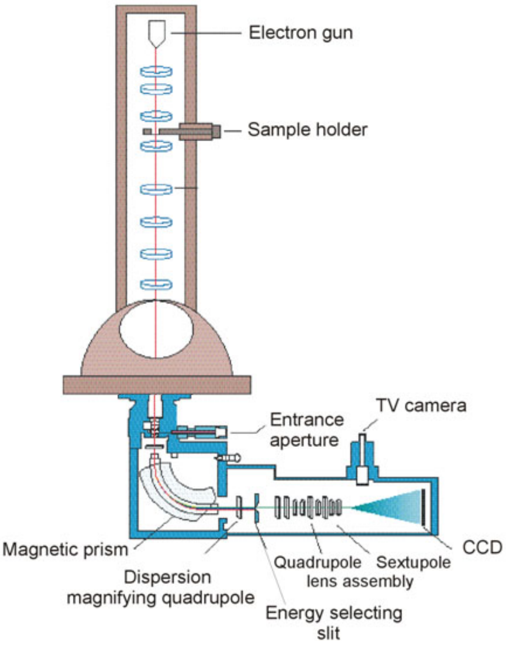

Figure 1.22.: *Schematic Illustration of a TEM with an electron energy loss spectrometer at the bottom[41].*

EELS is capable of analyzing Li to U, however light elements, transition metals and rare earth metals are detected most efficiently. H, He and some heavy elements, from Rh to Bi, are not always detectable. Due to this constraint, EELS and EDXS are often combined for chemical analysis.

1.2.2.1. Electron Energy Loss Spectra

A definite element analysis is possible due to the ionization of sample atoms by the high energetic primary electrons, whereby the primary electrons lose a characteristic amount of energy and appear as an edge in the spectra; see Figure 1.23 for exemplary spectra. This characteristic ionization edge is situated on a rather high background, which makes it necessary to optimize experimental setup experimental setup to obtain an adequate signal-to-noise ratio (**SNR**) for reliable EELS spectra.

A quantitative analysis with the intensities of the ionization edges can be done with accuracy down to a few percent and the detection sensitivity is very dependent on the chemical composition of the sample and the sample thickness. Typically, values down to 0.1 to 1 at.% can be achieved, in special cases even detection in the ppm range is possible. In addition to the ionization edges and the composition analysis, the edge

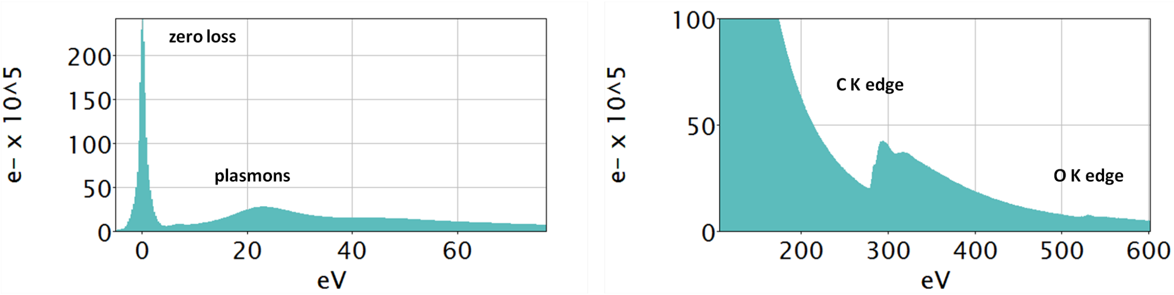

Figure 1.23.: *Low loss (left) and high loss (right) energy loss spectrum revealing the zero loss peak and plasmonic peaks in the low loss spectrum and the C K edge (at approximately 300 eV) and the O K edge (at approximately 530 eV).*

fine structure allows conclusions regarding the chemical binding of the excited atom. A subdivision into the energy-loss near edge fine structure and the extended energy-loss fine structure is constituted and with these two regions, a determination of electronic states, coordination number, oxidation state and bonding lengths is possible. By integrating a monochromator in the TEM electron column, an energy resolution lower than 0.3 eV is achieved and the information gain is enhanced, see Figure 1.23.

The low loss region below 50 eV of an EEL spectrum is based on the inelastic interaction with electrons of the outer energy levels, respectively the valence and conduction band, and provides information about the electronic and physical properties of the sample. Beside the excitation of collective electron oscillations in conductive samples (plasmons), intra and inner band transitions as well as the band gap of semiconductors are also accessible. The low loss region can be described by the dielectric function with its imaginary part representing the absorption leading to a correlation between EELS and optical material constants such as the refractive index or the absorption coefficient.

The major advantage of EELS is the excellent lateral resolution, which depends on the primary beam diameter and on suitable sample thicknesses which provide single interaction events during imaging. While the former is no longer not the limiting factor (meanwhile in the sub-Å range) the latter often represents the critical factor together with beam damage effects due to the exteremely thin beam diameter.

1.3. Atomic Force Microscopy

Since the invention of atomic force microscopy (**AFM**) in 1986 by Gerd Binnig, Calvin Quate and Cristoph Gerber as well as through further development, this is has become a well-established method in the field of surface characterization and manipulation in the micrometer and nanometer range. The most important advantage compared to other surface characterization methods is the quantitative 3D information down to spatial (sub-)nm resolution. Also, the ease of sample preparation and the non-destructive character for most cases are responsible for the wide range of use enjoyed by atomic force microscopy.

Due to the development of additional measurement modes, the accessible information goes beyond surface morphology and often can be obtained in a simultaneous manner. This additional information includes mechanical, electrostatic, chemical, electronic and magnetic properties.

In principle, the idea behind AFM is the raster-like measurement of the morphology with a very fine tip which is mounted on a fine and soft bar, called a cantilever. The bending of this cantilever due to the surface morphology is detected and processed to form a 3-dimensional image of the surface. In the following section, the basic principles and components of an AFM are discussed.

1.3.1. Components

1.3.1.1. Motion System

For a reliable motion on the nanometer scale with sub-nm accuracy, the system in the background has to be able to master even finer motions in the Ångstrom range. Thus most AFM motion systems are built using piezoelectric ceramics.

The piezoelectric effect describes the induction of a surface charge due to mechanical deformation, and vice-versa. This voltage application can be used for crystal contraction or expansion, as can be seen in the top part of Figure 1.24. By sophisticated arrangement of such materials, a very well-defined 3-dimensional motion can be executed.

One of these designs is the tube scanner, illustrated in the lower part of Figure 1.24, which is a very commonly used design for an AFM motion system. In a tube scanner like this the topmost ring is responsible for vertical Z-motion, whereas the lower part enables motion in the X and Y-directions. To achieve a motion in the X-direction, a counter voltage is applied to the opposing electrodes so that one side expands and the other contracts. Thus an elongation and a shortening of the opposing sides is achieved, resulting in a defined motion in the X-direction, as can be seen in Figure 1.25. Using the same principle, motion in the Y-direction is also possible and a 3-dimensional scanner

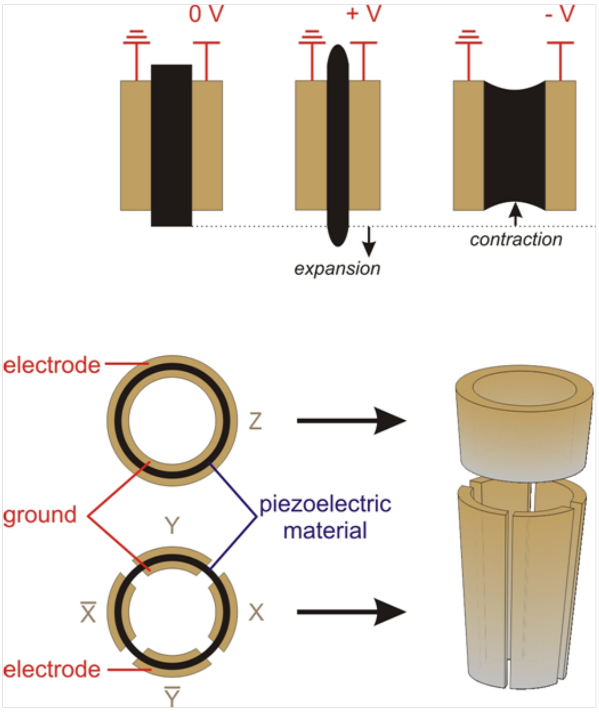

Figure 1.24.: *Schematic design of a tube scanner [2].*

is the result. The major issues of this design are interdependent mechanical influences, electrical coupling and the fact that the X and Y-motion is not performed on a planar level, but rather on a spherical surface, which must be corrected by software.

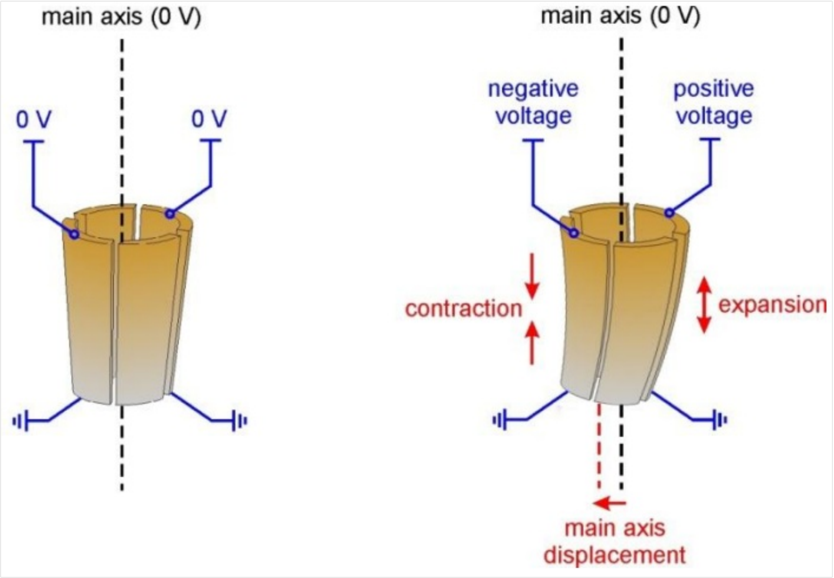

Figure 1.25.: *Schematic design and working principle of an AFM tube scanner [2].*

1.3.1.2. Cantilever and Tip

As described before, the cantilever is an essential part of AFM, because its detection is an indication for the probe-sample interaction. The cantilever deformation can be described by Hookes law $F = C_0 * x$ very well, where the spring constant C_0 is a factor that quantifies the flexibility of the oscillating cantilever.

Table 1.2.: *Typical properties of different tips used for different imaging modes.*

	Mode	Length [μm]	Spring constant [N/m]	Resonance frequency [kHz]
Sinlge bar	Tapping	160	42	360
Single bar	Tapping	240	2	70
Triangular	Contact	100	0.02	10
Triangular	Contact	200	0.6	70

Typically rectangular or triangular cantilevers are used, which possess different spring constants from very hard to very soft, respectively. A triangular cantilever also reduces massive torsion around the cantileverś main axis. Table 1.2 lists the cantilevers typically used in dependence on the working mode.

The geometry of the tips used demands special attention. In order to resolve the finest surface structures laterally, a tip with a very fine radius has to be used. Ideally the tip should be delta-shaped. Typical commercially available tips have a radius of approximately 5 - 10 nm and an opening angle of approximately 30°with a 3- or 4-sided pyramidal geometry.

Because of this less-than-ideal geometry, one has to deal with some limitations and influences of the geometric form of the tip. Mathematically, the measured signal can be obtained by a convolution of the tip geometry and the sample surface. In the following paragraphs, different convolution effects for obtaining a deeper insight into the challenging job of interpretation will be discussed.

Tip Radius: As is illustrated in Figure 1.26 a tip radius which cannot be infinitely small results in a convolution to broader and distorted structures. This leads to a limitation of lateral resolution.

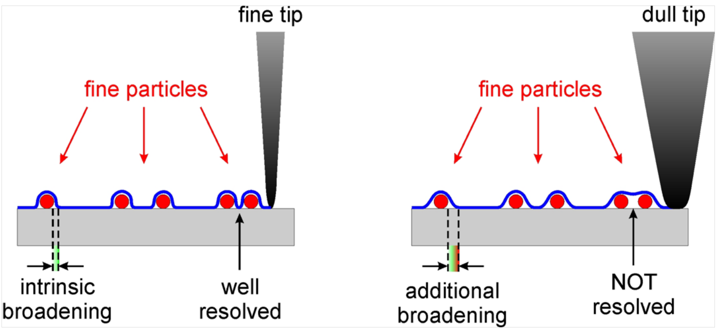

Figure 1.26.: *Comparison of line profiles with a fine and dull tip [2].*

Opening Angle: The opening angle is limiting at steep edges, which cannot be imaged properly, and also very fine holes and trenches are not measured exactly, because the tip is not able to intrude, as illustrated in Figure 1.27. Special tips with a very small opening angle and thus a high aspect ratio are available to deal with this challenge.

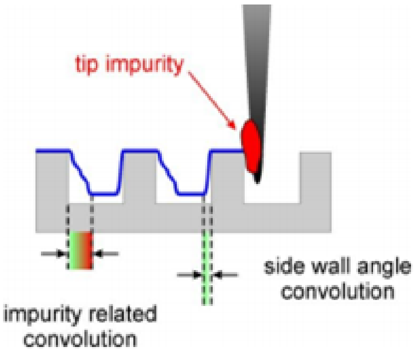

Figure 1.27.: *Influence of the opening angle and impurities on the edges of AFM measurements [2].*

Radial Geometry: Ideally a completely rotationally symmetrical tip is able to reproduce a sample surface properly. Due to the commonly used pyramidal tip, the geometry and the limited aspect ratio of very fine structures are not imaged accurately. In reality, it is the tip geometry which is reflected, as is shown in Figure 1.28.

Tip Damage and Contamination: Another very important resolution and image quality limiting factor is tip damage and contamination, which lead to uncontrolled tip modifications and thus a strong convolution of all effects that contributes to distortions. Typically, double or triple structures can be observed with the same orientation and features with equal shape appear, but a general blurring is also observed. Only changing

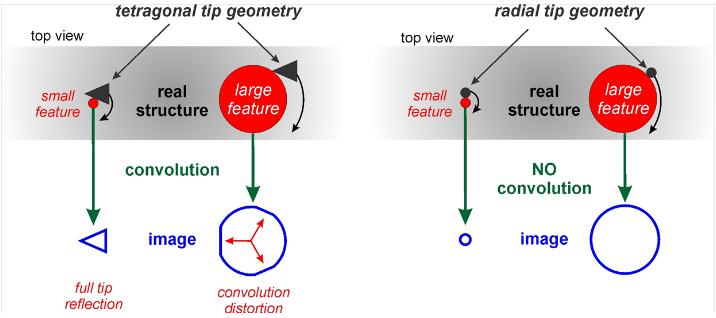

Figure 1.28.: *Convolution of tetragonal tip geometry in comparison to radial tip geometry [2].*

the tip eliminate this limitation factor and improve image quality. Figure 1.29 depicts the tip contamination and damage of a silicon standard which has in reality only vertical edges and only two height levels. The height scan shows distortions leading to an artificial height level and edge slope at opposing edges. The comparison with the real structure reveals a very good image of convolution through a damaged and/or contaminated tip.

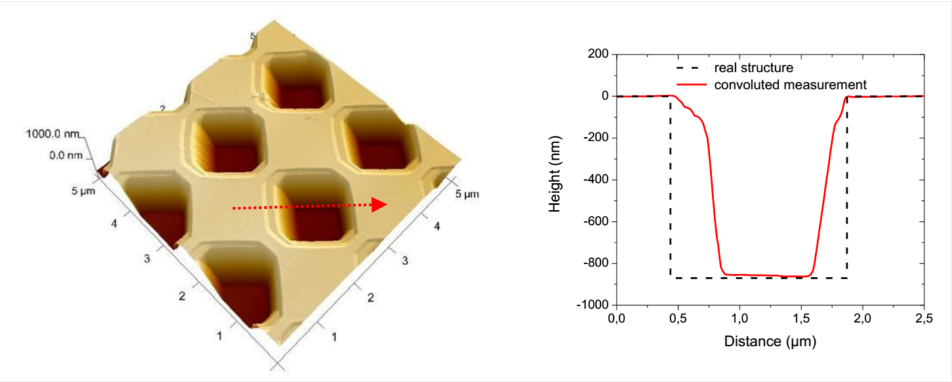

Figure 1.29.: *AFM measurement and Cross-section of a calibration standard revealing the convolution due to impurities and tip shape [2].*

Detector: The detection system has to be very sensitive due to the small movements of the cantilever, such as deflection and torsion in sub-nm range, and because of the small spring constant in Hookes law and the low forces expected in the range of 10^{-9} N. This can be realized by an optical laser detection system, as shown in Figure 1.30. It consists of a laser source and a lens system, which is responsible for positioning the laser on the cantilever. This laser spot gets reflected to a position sensitive detector (**PSD**). Due to a force acting on the tip and thus on the cantilever This laser spot is reflected to a position sensitive detector (**PSD**). Due to a force acting on the tip and thus on the cantilever, it becomes deformed and the position of the laser deflection will change on the

PSD. This, in turn, allows conclusions on the deformation and thus on the forces acting on the tip-cantilever system, thereby making morphological information accessible.

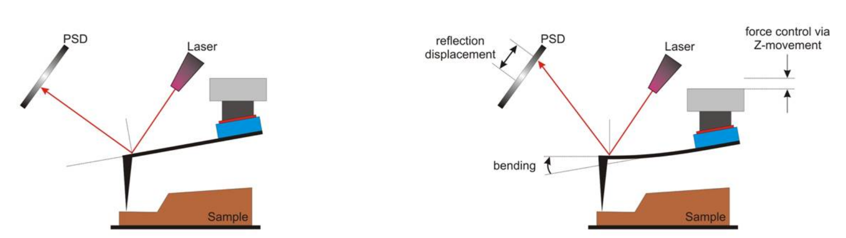

Figure 1.30.: *Schematic drawing of an optical laser detection system showing the light path at different scanner heights [2].*

It is very important that the laser be positioned on the very end of the cantilever in order to get the greatest sensitivity, resulting from the greatest amplitude of deformation. At this point, the laser signal is proportional to the tip motion. The second important issue concerning the positioning is that the intensity is maximized by positioning of the laser centrally on the cantilever. This leads to an optimized signal-to-noise ratio and in addition the thermal load resulting unreflected laser fractions onto the sample is minimized, which is essential for temperature-sensitive samples.

1.3.2. Topographical Imaging

To obtain topographical information, a clear tip-sample interaction is required to entail cantilever deflections which are detected by the PSD. Physically the interaction principle is dependent on the distance between the probe and the sample ranging from electrostatic and Van der Waals interaction to electron-electron interaction by decreasing distance. Table 2.2 reveals the ranges where the different interaction types are dominant.

Table 1.3.: *Different forces acting between the tip and the surface at different distances.*

Distance r tip-sample	Type of interaction	Potential
$> 10\,\mathrm{nm}$	Electrostatics	$\frac{c}{r^2}$
10 nm-5 nm	Van der Waals (dipole-dipole interaction)	$-\frac{a}{r^6}$
$< 2\,\mathrm{nm}$	e^--e^- interaction (Pauli principle)	$\frac{b}{r^{12}}$

Typically, during topographical imaging, the tip-sample distance is less than 10 nm leading to negligible electrostatic and magnetic contributions. In contrast a Lennard-

Jones (**LJ**) potential is used for the description of the tip-sample interaction; see the blue line in Figure 1.31.

$$V_{LJ} = V_{rep} + V_{VdW} = \frac{b}{r^{12}} - \frac{a}{r^{6}} \tag{1.4}$$

The LJ potential is a superposition of the repulsive and the Van der Waals (**VdW**) interaction, as shown in Figure 1.31 in red and green. By differentiation of this potential, one can get the force acting on the probe.

$$F_I = \frac{\partial V_{LJ}}{\partial z} = -\frac{12b}{r^{13}} - \frac{6a}{r^{7}} = -V_{rep} + V_{VdW} \tag{1.5}$$

This force leads to an attractive VdW interaction and a repulsive interaction for distances below 0.2 nm. Thus this force can be divided into an attractive and a repulsive regime (green and red regions in Figure 1.31, respectively). When approaching the sample, the cantilever is attracted to the sample due to the attractive force. Through further approach the tip becomes retracted due to the repellent effect caused by the Pauli principle, leading to a repulsive interaction at low tip-sample distances and, in turn, to an upward bending of the cantilever.

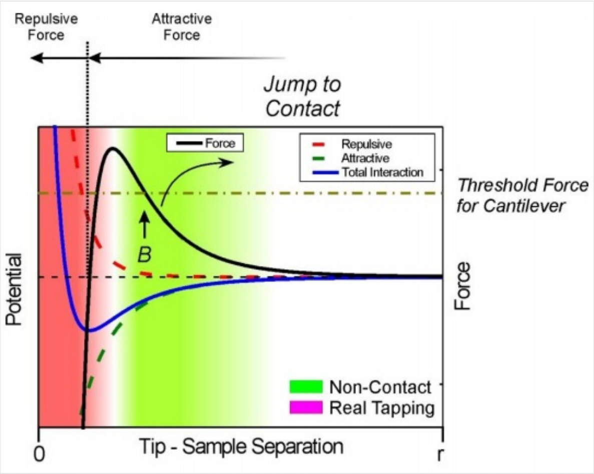

Figure 1.31.: *Lennard-Jones potential and actual force acting to describe the interaction between the tip and the surface [2].*

For the image formation it is important that the tip approach the surface at a point where a distinct, stable force acts on the tip. The cantilever will get deflected to a certain position which is detected by the laser reflection on the PSD. In the next step, the motion system moves the tip along the X-direction and, depending on the morphology, the cantilever deflection changes and this is detected by the PSD. The motion system now regulates the vertical scanner position in such way that the laser reflection will end up in the same position as for the previous point on the surface, ensuring the same forces between the surface and tip at both positions. The vertical Z-position of the scanner for every point (X,Y) can be interpreted as a topography image.

1.3.3. Contact Mode

In contact mode the tip is in permanent contact with the sample. The setpoint parameter is used to adjust the force acting on the sample, which the system holds constant. Technically, this constant force is equal to a constant deflection of the cantilever and thus a constant position of the laser is reflected on the PSD.

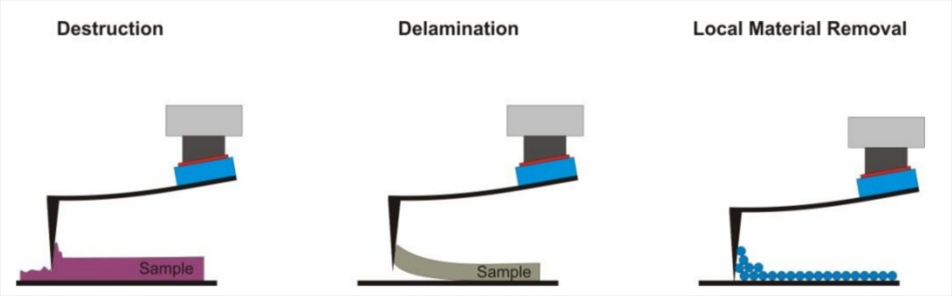

Figure 1.32.: *Schematic drawing of possible damage caused by direct tip-sample contact [2].*

One of the outstanding properties in this mode are the high scan rates that can be achieved and which nevertheless allow atomic resolution on adequate samples like mica and graphite even at atmospheric conditions. One major disadvantage is that the tip is in permanent contact with the sample surface. This may induce some problems, such as destruction due to the hard and sharp tip, especially on soft materials, delamination of thin layers or fragmentation, particularly with weak adhesion to the substrate, or even local material displacements on samples with small particles are possible, as is illustrated in Figure 1.32.

To avoid these disadvantages, another imaging mode was developed, which will be discussed in the following section.

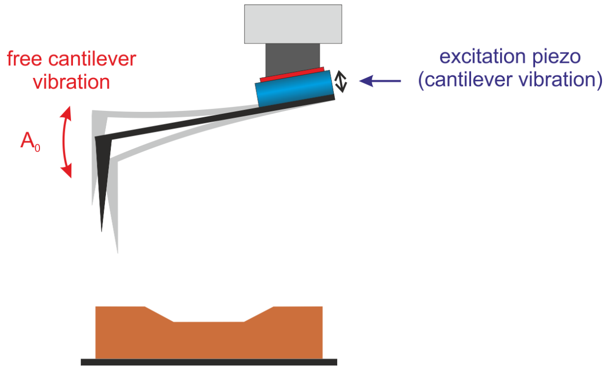

Figure 1.33.: *Schematic drawing of the excitation of the cantilever by a piezoelectric crystal [2].*

1.3.4. Tapping Mode

In order to reduce the tip-sample interaction which can induce sample damage, this alternative principle of measurement uses a cantilever oscillating at its mechanical resonance frequency ω_0 instead of a static deflection. The advantage is that this type of measurement is able to work in real non-contact conditions by providing spatial (sub-)nm resolution. This oscillating behavior is maintained by an additional piezoelectric crystal, as is illustrated in Figure 1.33, which excites the cantilever to resonance while the laser induces an alternating current on the PSD. Thus, the root mean square amplitude (**RMS**) can be used to control the tip-sample distance. The resonance frequencies of commonly-used cantilevers are listed in Table 1.2.

When the oscillating tip approaches the sample, the interacting forces lead to a damping of the amplitude, which is illustrated in Figure 1.34. This decrease in amplitude is a result of the energy dissipation due to the (partial) contact between tip and sample and the shifting of the resonance frequency ($\omega_0 \rightarrow \omega_{coupled}$) through the electrostatic coupling between tip and sample, which can be described by a shift of the spring constant. This damped amplitude is detected by the PSD and used to keep the amplitude constant for each point (X,Y) leading to a topographical image.

An important advantage of this mode is the ability to tune the interaction for the desired working regime and thus tap very gently on the sample, minimizing sample damage. During the approach, the first regime is the non-contact or attractive regime. The tip does not make contact with the sample in this regime, but high resolution is achievable, and the tip-sample interaction is mainly attractive. The benefit of this regime is of particular importance for soft materials and samples where the surface is very

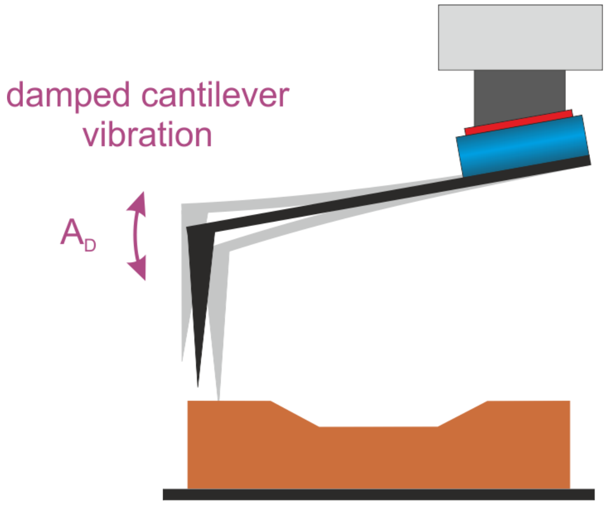

Figure 1.34.: *Schematic drawing of the damped cantilever vibration of the tip after approach [2].*

sensitive to mechanical damage. The other regime, where the tip-sample distance is decreased compared to the attractive regime, is the intermittent regime, where the probe taps onto the surface and the repulsive interaction becomes predominant. This may be favorable with an adhesive sample for pushing through the water layer on the sample.

This water layer on the sample and the oscillating tip may cause a meniscus to form when the tip touches the sample. This disadvantageous effect may disturb image acquisition by means of unstable measurement conditions and/or direct imaging of the surface wetting layer instead of the underlying features of interest.

Another major advantage is the ability to measure laterally resolved material properties at the same time using phase imaging, to be discussed in the next section.

1.3.5. Phase Mode

The development of the phase mode was an instrumental extension, which allows laterally resolved imaging of material distribution or varying phases (amorphous, crystalline) simultaneously to the topographical information in tapping mode. The principle of this mode is based on an enforced, damped oscillation of the cantilever, whereby the cantilever phase lags the exciting phase from the piezoelectric crystal, as can be seen in Figure 1.35 (left). The resonance frequency of the cantilever is shifted by a tip-sample interaction, which leads to a displacement of the phase curve. Due to the constant excitation frequency, the phase lag is shifted, which can be detected with a so-called

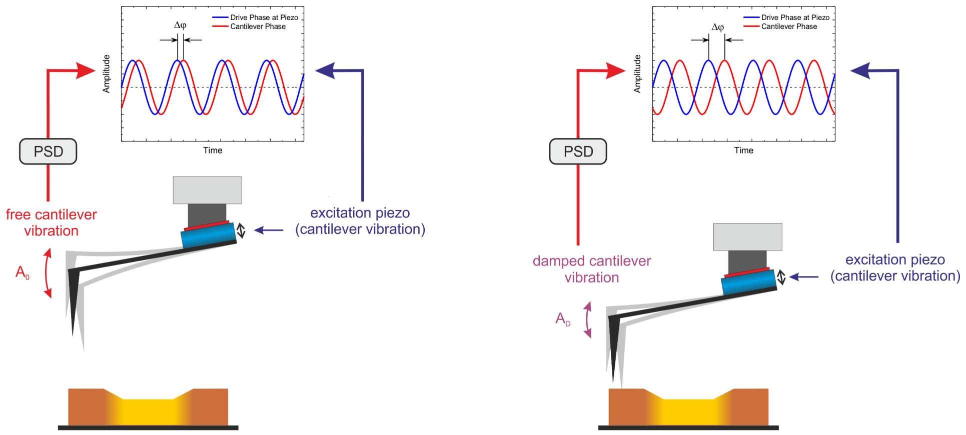

Figure 1.35.: *Basic principle of the phase mode (a) with free cantilever phase lag and (b) material dependent damped phase lag [2].*

lock-in amplifier at the PSD. The phase lag is varied by the material-tip interaction. Thus a material determination is possible, which is illustrated in Figure 1.35 (right). The working regime in tapping mode is a very important information that is gained from the phase lag since the algebraic sign of the phase lag identifies repulsive or attractive regime conditions allowing selection of the appropriate situation.

1.3.6. Kelvin Probe Force Microscopy

In Kelvin Probe force microscopy (**KPFM**), which is a widely used method for electrostatic measurements, the contact potential difference (**CPD**) between the probe and the sample surface can be measured, according to [23, 33]:

$$V_{CPD} = \frac{\Phi_{tip} - \Phi_{sample}}{-e} \tag{1.6}$$

where Φ_{tip} and Φ_{sample} are the working functions of the tip and the sample, respectively, and e is the electric charge.

By moving the conductive tip toward the surface an electrostatic force is generated due to the balancing of the different Fermi energy levels. This force is given by:

$$F_{es}(z) = -\frac{1}{2}\Delta V^2 \frac{\partial C(z)}{\partial z} \tag{1.7}$$

where ΔV is the potential difference between the voltage applied to the tip and the surface and z is the direction normal to the sample surface. C denotes the capacitance between the tip and the sample, which depends on the tip-sample distance. With an electric excitation of the cantilever to its intrinsic resonance frequency with:

$$V_{tip} = V_{DC} + V_{AC} sin(\omega t) \tag{1.8}$$

the potential difference between the tip and the surface is given by:

$$\Delta V = V_{tip} \pm V_{CPD} = (V_{DC} \pm V_{CPD}) + V_{AC} sin(\omega t) \tag{1.9}$$

By inserting this potential difference ΔV into the electrostatic force, given by Equation **??**, the force acting can be described in three parts:

$$F_{es}(z) = F_{DC} + F_{\omega} + F_{2\omega} \tag{1.10}$$

$$F_{DC} = -\frac{\partial C(z)}{\partial z}[(V_{DC} \pm V_{CPD})^2] \tag{1.11}$$

$$F_{\omega} = -\frac{\partial C(z)}{\partial z}(V_{DC} \pm V_{CPD}) V_{AC} sin(\omega t) \tag{1.12}$$

$$F_{2\omega} = -\frac{\partial C(z)}{\partial z}\frac{1}{4}V_{AC}^2[cos(2\omega t) - 1] \tag{1.13}$$

With equation 1.12 the actual V_{CPD} is measured. As one can see, a force F_{ω} arise if $\mathrm{V}_{DC} \neq \mathrm{V}_{CPD}$. Due to the sine modulation at ω, F_{ω} oscillates the cantilever at its resonance frequency, which can be detected by the PSD. By applying an accurate voltage V_{DC} to the AFM tip, the force will be zero and so, the measured amplitude nullifies for $\mathrm{V}_{DC} = \mathrm{V}_{CPD}$. This value V_{DC} is adjusted for each point individually, which yields a laterally resolved map of surface potential. The different cases can be seen in Figure 1.36. Equation 1.13 is useful for controlling the applied voltage, due to the fact that it is the derivative of equation 1.12 and for a small voltage change, it is used to verify in which direction the voltage must be changed [28].

Challenges concerning the KPFM are, first of all, the tip-sample separation, which affects the reliability as the most important parameter.This is due to a convolution of the signal from the cantilever, the cone and the apex in KPFM mode. The spatial resolution is not only limited by the tip apex but is considerably influenced by the cantilever area (additional capacitance). This influence can be decreased by reducing the tip-sample separation to a minimum, in which the tip apex becomes dominant and spatial resolution is optimized. However, for classical ambient conditions, the required tip-sample distances are often limited by the surface wetting layer. Therefore, the most critical KPFM studies in this thesis have been performed in inert conditions which reduce the wetting layer thickness allowing smaller tip-sample distances and thereby increasing the lateral resolution.

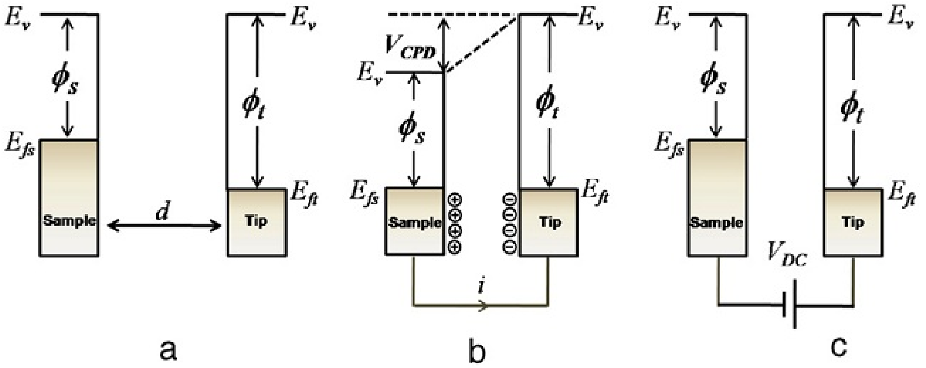

Figure 1.36.: *AFM tip and sample energy levels. (a) no electrical contact due to separation, (b) electrical contact, (c) applied external bias between tip and surface to nullify CPD [28].*

1.4. Raman Spectroscopy

Besides the mid-infrared (**IR**) or near-IR, a very common technique of vibrational spectroscopy is Raman spectroscopy. With both mid-IR and Raman spectroscopy (**RS**), characteristic fundamental vibrations are used for the molecular structure elucidation and a wide range of sample types and research issues can be carried out, ranging from simple identification to an in-depth, full spectrum, qualitative and quantitative analysis. One of the outstanding advantages of these vibrational spectroscopy methods is the relative ease of sample preparation since bulk or microscopic samples can be investigated over a wide range of physical states and temperatures, resulting in a very broad range of applications, even in challenging analytical problems.

Due to the complementary aspect of Raman and IR spectroscopy, a combination of both is usually required for a complete analysis of the vibrational modes of a molecule. The complementary aspect arises from the different processes and different selection rules, although some vibrations are active in both Raman and IR spectroscopy. Generally, during IR spectroscopy the asymmetric vibrations of polar groups are responsible for activity, while in Raman spectroscopy, the symmetric vibrations of non-polar groups are measured.

This difference is due to the basic principle of excitation. In principle, during IR spectroscopy, the transition between molecular vibrational energy levels resulting from absorption is responsible for the generation of Raman active modes / transitions, which can be seen as an interaction between light and matter in resonance resulting from an electric dipole transition between vibrational energy levels. In contrast, the Raman spectroscopy results from a two-photon inelastic light scattering event. Here, Raman active transitions are a result of energy loss to molecular vibrations of the incident photon, while the remaining energy is scattered as a photon with reduced frequency. Hence, this interaction is off-resonance and the Raman spectroscopy is based on the change of the polarizability of the molecule.

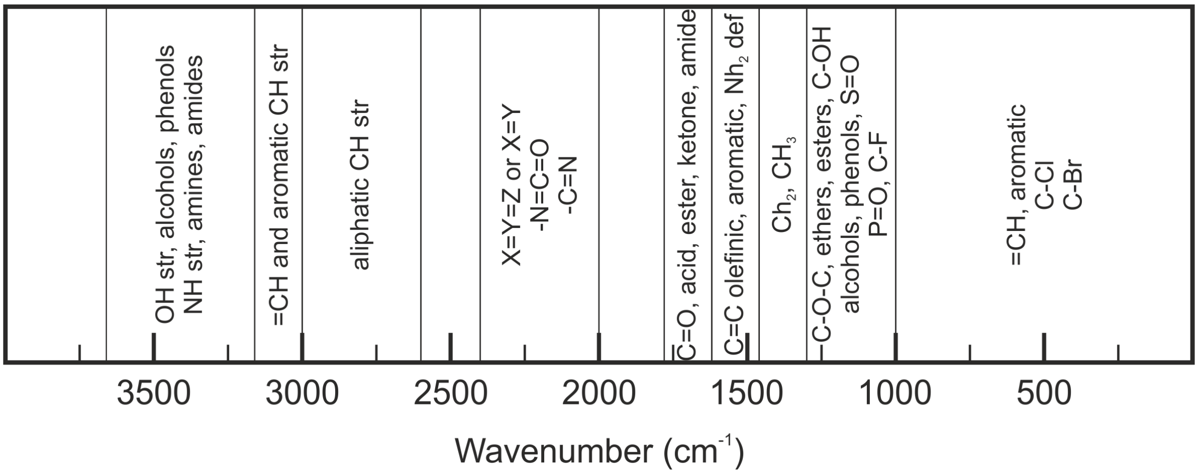

Figure 1.37.: *Regions of the fundamental vibrational spectrum with some characteristic group frequencies.*

The characterization of vibrational bands is achieved by their frequency/energy, intensity and band shape. Due to the unique character of each molecule and its vibrations, the spectra serve as a fingerprint for each particular molecule, since the vibrational energy depends on the masses of the atoms, their geometric arrangement and the strength of the chemical bond. A coarse classification of the vibrational spectrum and its typical regions is shown in Figure 1.37.

1.4.1. Basic Principles

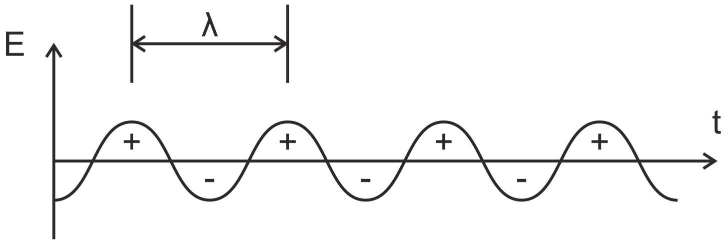

Figure 1.38.: *The amplitude of an electric vector of electromagnetic radiation as a function of time.*

Since light is an electromagnetic wave, it consists of alternating electric and magnetic fields which describe a continuous sinusoidal wave-like motion. For understanding IR and Raman spectroscopy, only the electric field is of importance. Thus the magnetic component will be neglected, as shown in Figure 1.38. For a description of electromagnetic waves, the wavelength λ, the frequency ν, and the wavenumbers $\bar{\nu}$ are relevant parameters, which are related according to Equation 1.14 with c being the speed of light and n is the refractive index.

$$\bar{\nu} = \frac{\nu}{\frac{c}{n}} = -\frac{1}{\lambda} \tag{1.14}$$

Quantum theory describes radiation as discrete units emitting from a source, so-called photons with energy E_p and with h as Planckś constant.

$$E_p = h\nu \tag{1.15}$$

By an energy transfer from or to molecule vibrations, photons of specific energy can be emitted or absorbed, respectively.

$$\Delta E = E_p = h\nu = hc\bar{\nu} \tag{1.16}$$

This energy transfer ΔE results in an excitation from ground states schematically illustrated in Figure 1.39. Such excitations are typically rotational or vibrational electronic molecule states. In IR and Raman spectroscopy, the energy range of the impinging photon is in the range of vibrational transitions for condensed matter, while in gas phase samples, rotational transitions are also included. For higher and lower photon energies, electronic and rotational transitions have to be considered, respectively.

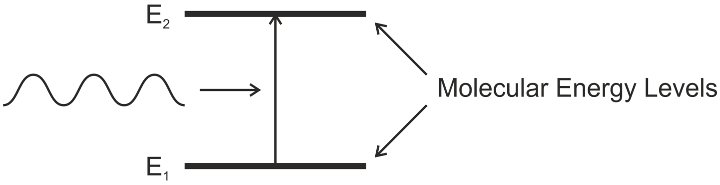

Figure 1.39.: *Absorption of electromagnetic radiation.*

1.4.1.1. The Raman Scattering Process

In classical physics, the scattering of light is described by electromagnetic radiation as a result of an oscillating dipole which is induced by the incident EM fields of radiation. The induction of a dipole moment is strongly dependent on the molecular polarizability α, which is the deformability of the electron cloud of the molecule by an external field. This photon scattering consists mostly of Rayleigh scattered light, revealing the unchanged energy of the scattered photon, and a very small amount of Raman scattered light, which describes the higher or lower energetic photons with respect to the incident energy. To observe Raman scattering, the polarizability must be shifted by the molecular vibration.

In both cases, an incident photon is absorbed by the molecule leading to an excitation into v́irtualśtates. Relaxation down to the ground state generates a new photon with the same energy as the incident photon, which is the so-called Rayleigh scattering. This is also an elastic scattering and is the most probable event with an intentsity that is approximately 10^{-3} less than the original incident radiation, as is schematically illustrated in Figure 1.40. With 10^{-6} less intensity than the incident beam, the far less probable Raman scattering occurs after a transition to virtual states and to excited states of molecular vibration, which is called Stokes scattering. Here, the scattered photon has less energy than the incident photon ($hc(\bar{\nu_L} - \bar{\nu_m})$), as can be seen in Figure 1.40. Anti-Stokes scattering occurs as a result of a transition from an excited state of vibration to the virtual state and back to the ground state, where the created photon is of higher energy than the incident one ($hc(\bar{\nu_L} + \bar{\nu_m})$).

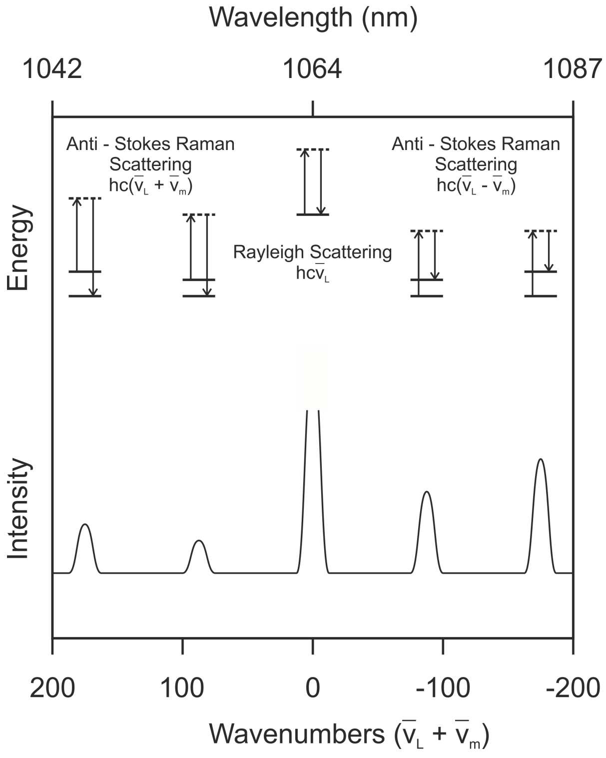

Figure 1.40.: *Schematic illustration of Rayleigh scattering as well as Stokes and anti-Stokes Raman scattering.*

In the classical description of the Raman effect, the electromagnetic field perturbs the charged particles, which results in the induction of a dipole moment, with α the polarizability, E the electromagnetic field and μ the induced dipole moment:

$$\mu = \alpha E \tag{1.17}$$

As the electric field of the radiation is oscillating at the frequency ν_0, the induced dipole moment will follow this oscillation, as is illustrated in Figure 1.41 (a). In addition the polarizability varies slightly with the molecular vibrational frequency ν_m, leading to an amplitude modulation of the dipole moment oscillation of the molecule; see Figure 1.41 (b) and (c). This modulated oscillation can be mathematically described by three components with steady amplitude and frequencies of ν_0, $\nu_0 + \nu_m$ and $\nu_m - \nu_m$, which can be seen in Figure 1.41 (d). This modulation of the dipole moment is responsible for the emission of radiation at the same frequency, which is the Rayleigh scattering, and increased and decreased frequency, which are the Raman anti-Stokes and Stokes scattering, respectively. Molecules with no shift in polarizability caused by the molecular vibration induce no change in the dipole moment amplitude and thus no Raman scattering occurs.

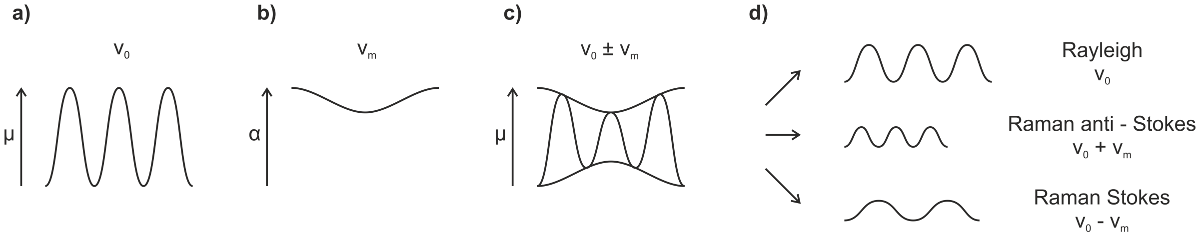

Figure 1.41.: *Schematic drawing of Rayleigh and Raman scattering. (a) incident radiation, (b) molecular vibration changes polarizability which causes changes in amplitude of dipole moment oscillation, shown in (c) as amplitude modulated dipole moment oscillation, (d) components of the emitted electromagnetic radiation.*

1.4.1.2. Molecular Motion-Degree of Freedom

The characteristic vibrations of molecules can be described by the internal degrees of freedom, which are 3n - 6 and 3n - 5 for vibrations of non-linear and linear molecules, respectively. This is a result from 3 degrees of freedom for each atom in the molecule with n the number of atoms reduced by three degrees of translation and rotation. These internal degrees of freedom can be seen as motions of atoms leading to a variation of distance and/or angle between the atoms. In Figure 1.42, the vibrations and molecular motions of a water molecule (H_2O) and a carbon dioxide molecule (CO_2) are illustrated with 3 and 4 degrees of freedom, respectively. Some vibrations are the normal mode of vibrations; because each atom goes through the equilibrium position simultaneously, the center of mass is not oscillating and the molecule does not rotate. For the H_2O molecule, many different types of vibration exist:

In-Plane Stretching Movements: These vibrations can occur in symmetric and asymmetric form. A vibration is called stretching when the length of a bond is changing, such as H-O in the water molecule, C-H or C-C, as is illustrated in Figure 1.42 indicated by V_{ip}.

In-Plane Bending Movements: A bending vibration is defined by a change of the angle between two bonds, such as the angle between H-O-H in a water molecule. These vibrations can be subdivided into rocking and scissoring types, where the molecules

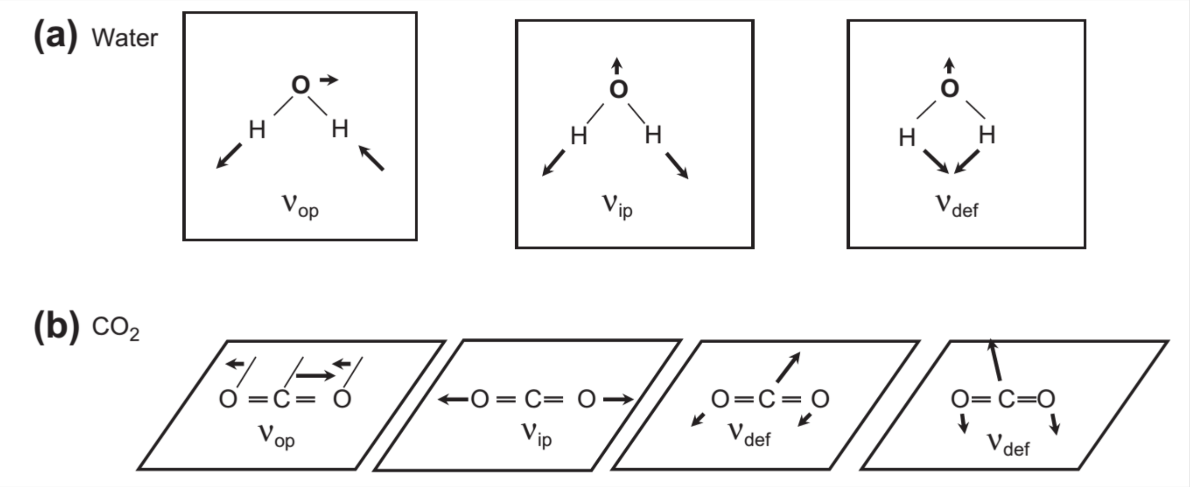

Figure 1.42.: *Molecular motions which change distance between atoms for water and CO_2.*

vibrate in the same direction or contrary to each other, as can be seen in Figure 1.42 indicated by V_{def}.

Out-of-Plane Bending Movements: In out-of-plane bending vibrations the molecules vary their position out of the plane of a planar molecule. These are subdivided into a twisting and a wagging vibration, which is a change in angle between the plane of two groups of atoms or one group of atoms, respectively, and is illustrated in Figure 1.42 indicated by V_{op}.

1.4.1.3. Raman Active Vibrations

A very important property determining whether a vibration is Raman active or inactive is the symmetry of the molecule. Generally, the vibrations have to be symmetric or in-phase, but also non-polar groups are Raman active. Symmetry elements include planes of symmetry, axes of symmetry and a center of symmetry. The center of symmetry can be defined by starting at one atom and by going through the center of the molecule, another identical atom must be found on the other side. Figure 1.42 shows the center of symmetry for H_2O and CO_2 as a determining factor, as to whether they are Raman active or not. A vibration is in principle Raman active when the center of symmetry is retained, generating a change in the polarizability during vibration.

Molecules without a center of symmetry may possess other symmetry elements leading to Raman active vibrations, as can be shown by in-phase stretches of inorganic nitrate

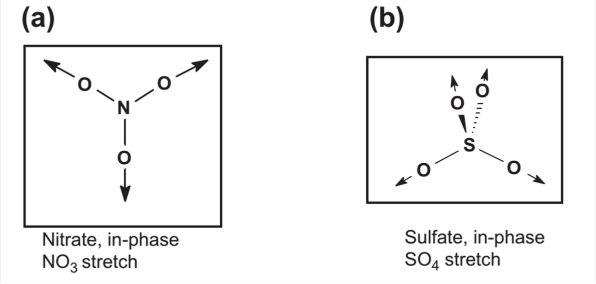

Figure 1.43.: *Raman active nitrate and sulfate vibrations.*

or sulfate in Figure 1.43. Here, the oxygen atoms vary their position radially and simultaneously leading to no change in the dipole moment. Additional symmetry elements of an H_20 molecule are shown in Figure 1.44, revealing a plane of symmetry for a two-fold rotational axis of symmetry and an identity operator. All of them lead to a reordering of the symmetrically arranged hydrogen atoms.

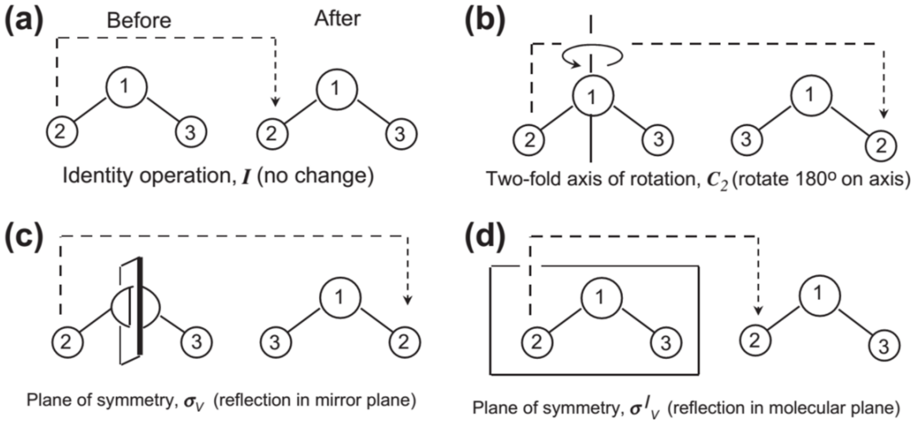

Figure 1.44.: *Symmetry operations for an H_2O molecule in the equilibrium configuration.*

1.4.2. Instrumentation and Sampling Methods

Basically, a Raman instrument is made up of a laser excitation source, an optical collection system, a spectral analyzer and a detector. In RS, a laser beam is focused on the sample and the focused emitted light is collected by a spectrometer. In Fourier transform (**FT**) instruments, an interferometer is used, whereas in dispersive instruments, a monochromator is responsible for the dispersion. Generally, interferometer-based and grating-based instruments are commonly used with a multi-channel detector. When designing a Raman instrument, the maximization of the conflicting parameters, the optical throughput and the spectral resolution, must be considered, while using highly sensitive array detectors dramatically improves the performance of dispersive Raman systems.

1.4.2.1. Dispersive Systems

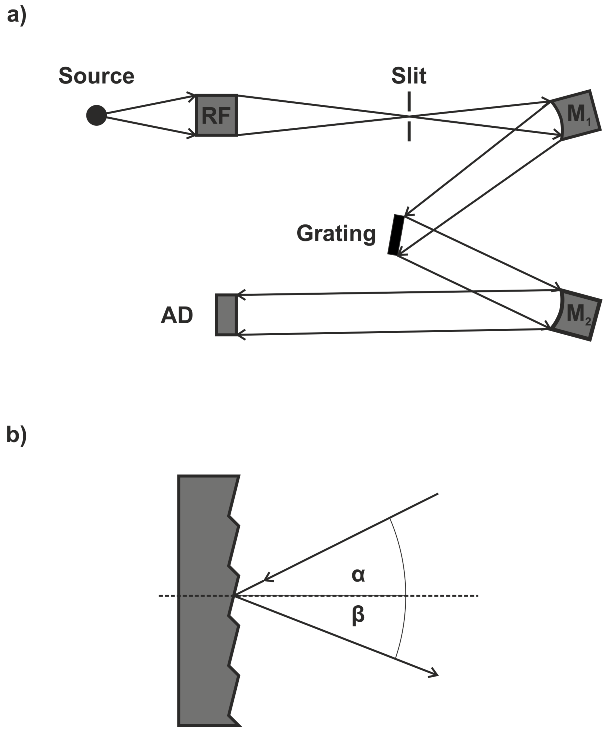

Figure 1.45.: *(a) schematics of a single monochromator-based Raman instrument, (b) schematic drawing of a diffraction grating.*

Grating-Based Dispersive Raman Instrumentation: Due to the predominant, but unwanted Rayleigh scattered light, a filtering element (see Figure 1.45 (a) for a schematic overview) must be used for analyzing the weak Raman scattered radiation. The wavelength-selecting element starts with an entrance slit, which isolates the wavelength range transmitted to successive elements, followed by a mirror for deflecting the radiation to a parallel beam onto the diffraction grating, which consists of many parallel lines or grooves spaced approximately by the wavelength on a reflective planar or concave plane. Thus, the incident light is only reflected when the path length of radiation falling on adjacent grooves is a multiple integer of the wavelength. This path length difference depends on the groove spacing, the angle of incidence α and the angle of reflectance β of the radiation, as is shown in Figure 1.45 (b). The reflected light is then deflected to an array detector by a second mirror. This detector consists of an array of photo diodes or CCDs, each element detecting a different spectral range. Due to the limited number of detector elements (typically 256, 512 or 1024) an entire spectral range can only be covered with low resolution, while it is possible to record a limited spectral range with high resolution. This problem can be avoided in a multi-channel instrument by adding high resolution spectra.

Interferometric Spectrometers: Fourier transform measurements are attractive due to the simultaneous measurement of light, which results in a multiplex advantage. Another important advantage is the high throughput, which is realized by the entrance slit. Technically, these advantages are achieved by the use of a Michelson interferometer, which is schematically shown in Figure 1.46. This interferometer consists of a beam splitter and a fixed and a moving mirror. The beam splitter divides the incident light beam equally into two components, one deflected towards the fixed and one towards the moving mirror. Both mirrors reflect these components and send the beams back to the beam splitter, where 50 % of both are sent to the detector. By a defined movement (Δl) of the moving mirror the path difference, called optical retardation, between the two different routes (moving and fixed mirror) is varied, which causes a phase-dependent interference between the two light beams. The interfering light is recorded by the detector causing an interferogram with the varying optical retardation.

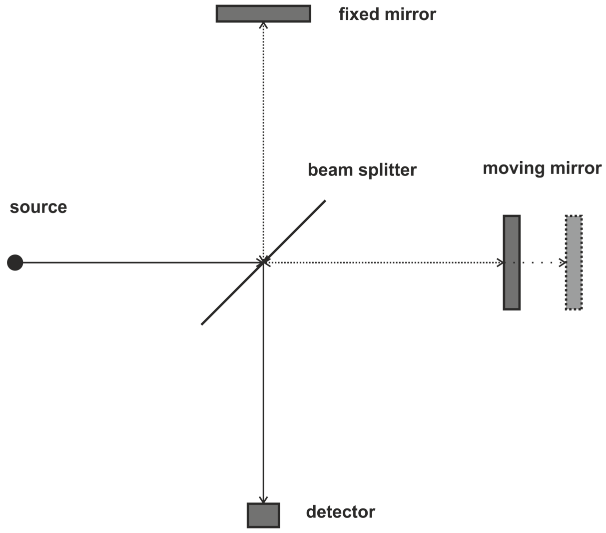

Figure 1.46.: *Schematic illustration of a Michelson interferometer.*

For a single monochromatic light source with wavelength λ with an identical path length on the fixed and moving sides, the two beams will interfere constructively in phase resulting in a maximum signal at the detector. Constructive interference will also occur for an integral wavelength of optical retardation (λ, 2λ, 3λ,...). Each time the path difference is changed to $\lambda/2$, $3\lambda/2$,... the beams will interfere destructively and will result in a minimum signal at the detector. By Fourier transformation of this interferogram, which is sinusoidal for a monochromatic light source, the characteristic frequency can be measured. With a polychromatic source the interferogram will be a superposition of multiple sine functions which correspond to the wavelengths contained in the source. Only for zero path difference will each component interfere constructively, resulting in a very strong center burst, which is rapidly damped with optical retardation. The Fourier transformation is then used for spectrum acquisition.

1.4.2.2. Sample Arrangements and Preparation

In principle, Raman scattered light occurs in all directions, but typically 90°and 180°collection angle configurations are used, as can be seen in Figure 1.47. In FT-RS and Raman microscopes, the 180°optics setup is the optimum sample arrangement as a result of narrow band self-absorption in the near-IR region.

One important advantage of RS is the minimal requirements for sample preparation and handling. Typically cuvettes, tube holders, solid holders or clamps are used for sample handling, but often the Raman spectra can be measured directly on the sample without any additional preparation.

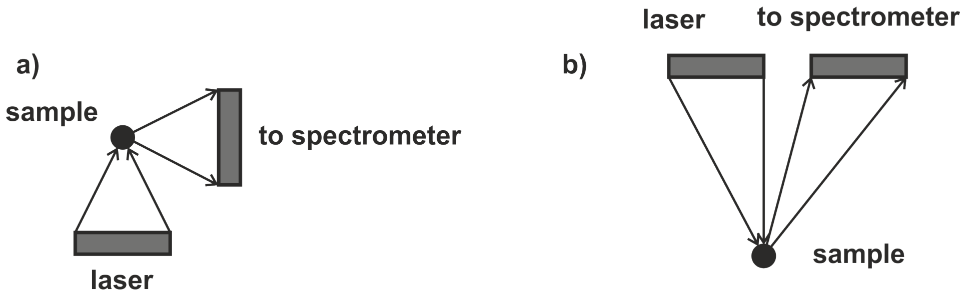

Figure 1.47.: *Two different collection options for Raman spectroscopy (a) 90°collection geometry and (b) 180°collection geometry.*

1.5. Ultramicrotomy

Microtomes are precision preparation tools typically used for the fabrication of thin cuts with a diamond or glass knife having a thickness of 1 to 10 μm, 1 to 0.25 μm for semi-thin and 150 to 50 nm for ultra-thin cuts. Generally, the thickest slices are used for histologic cuts for light microscopy or IR Raman spectroscopy, while the thinnest cuts are used for TEM investigation.

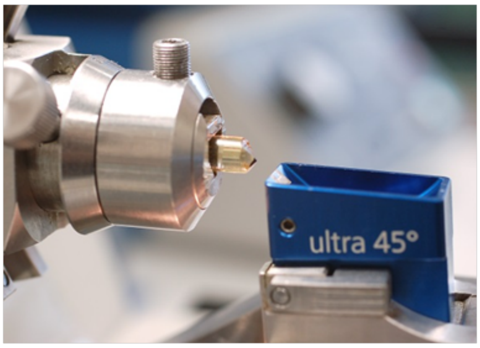

Figure 1.48.: *Knife and sample holder of an ultramicrotome [1].*

Such an ultramicrotome consists of a body for stabilization and the progression mechanism. Furthermore, the sample holder and the knife holder are mounted on the body; see Figure 1.48 for an image of the knife and sample holder. Microtomes in which the specimen is moved against the knife and vice versa are commonly used, but basically the sample or the knife is moved at a certain speed relative to the sample and produces a cut with a predefined thickness. For each cut, the knife-sample distance has to be regulated by the progression mechanism for ensuring the same cut thickness. A very important component of this method is the knife, which can be made out of diamond or glass.

Glass Knife: The production of glass knives is carried out using a knife-maker, which is a tool for breaking the glass in a first step into squares out of a glass bar. This square is then cut in a second step diagonally to the actual knife. This is also called a triangle knife due to its shape; see Figure 1.49 (left).

Diamond Knife: This knife is made out of a polished diamond; see Figure 1.49 (right). With these, a cut thickness down to 60 nm can be achieved. Ultrathin cuts can only be processed with a wet knife edge, which makes the need to combine the knife with a liquid

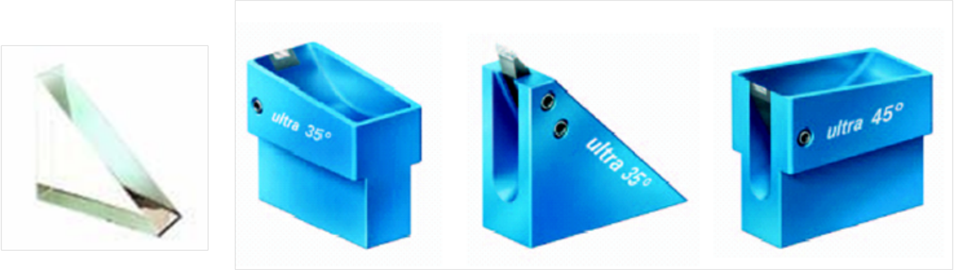

Figure 1.49.: *Glass (left) and diamond knife in various geometries for an ultramicrotome [1].*

reservoir obvious. With this fluid, it is possible to bring the cuts away from the knife scratch-free.

A very important parameter of the cutting process is the inclination, which is the angle between the knife and the sample plane. For achieving optimal results, typically, a small opening angle of a few degrees between the sample and the knife is set up, otherwise it is too flat or steep, which is illustrated in Figure 1.50. But the optimal angle is also dependent on the knife geometry, the sample itself and the cutting speed. With too flat of an angle, the knife will produce irregular cuts or a thicker part of the knife will make contact with the sample and smear over the sample. In contradistinction, with angles that are too steep, the knife will not glide smoothly through the sample producing periodic thickness variations in the cut. With extremely high inclination angles, such a high lateral load on the knife edge can lead to break outs.

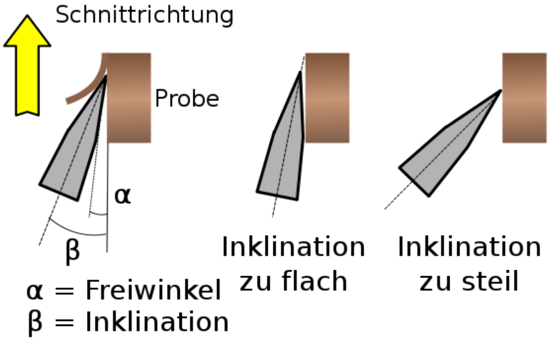

Figure 1.50.: *Schemtic illustration showing the importance of the correct angle between knife and sample [1].*

Sample preparation typically requires pre-embedding of the specimen, which can be done at room or elevated temperature, depending on the sample requirements. This embedding protects the specimen from damage during the preparations steps and generally leads to a good edge quality. It is also possible to produce standardized sample geometries, which makes the handling easier. Typically duroplasts, which are hardened non-reversibly, or thermoplasts, which are hardened reversibly, are used.

Cryo Ultramicrotome: A special modification of a conventional ultamicrotome adds the possibility of cooling down the sample to nearly the temperature liquid nitrogen.This sample cooling decreases the temperature to below the glass transition temperature in order to achieve optimized sample hardness. For optimization, the temperature can be controlled between - 180°C and room temperature.

1.6. Simulations

The stopping range of ions in matter can be calculated with the ǵolden standardśoftware package, SRIM [54]. This package is based on binary collision approximation and the impact parameters of the next colliding ion are selected randomly. The incoming ions and the target atoms have a screened Coulomb collision including exchange and correlation interactions between overlapping electron shells. The long-rang interaction of ions is included with the generation of excited electron and plasmons within the target using a description of the targetś collective electronic structure and interatomic bond structure. Furthermore the charge state of the ion within the target is described by the concept of effective charges, including long-range screening due to the collective electron sea of the target and a velocity-dependent charge state. For a full description of the calculation, see [54].

The assumptions of the software for the calculation of cascades, target displacements, replacement collisions, etc are defined below:

First of all, the atomic number of the incident ion is Z_1 and its energy E. The atom within the target with which the incident ion collides has an atomic number of Z_2. After the collision, E_1 is the energy of the incident ion and E_2 is the energy of the target atom. Furthermore, the displacement energy is E_d, the binding energy of a lattice atom to its site is E_b, and E_f is the final energy of a moving ion or atom, below which it is stopped.

With these definitions, a displacement occurs if $E_2 > E_d$ and a vacancy is formed if $E_1 > E_d$ and $E_2 > E_d$. Thus, a displacement is formed when the target atom is given enough energy to leave the site and a vacancy occurs when both atoms have enough energy to leave the site. The incoming and the target ion/atom become moving atoms of the cascade. For further collisions, energy E_2 of the target atom is reduced by its binding energy E_b. If energy $E_2 < E_d$,the target atom, which does not has enough energy, leaves the site and vibrates back to its original site by releasing E_2 as phonons.

The incoming ion will remain at the site of the target atom if $E_1 < E_d$ and $E_2 > E_d$ and $Z_1 = Z_2$, which is called a replacement collision, and energy E_1 is released as phonons, which is common in single element targets with large recoil cascades. If the energy relations are the same and the atomic numbers are different, $Z_1 \neq Z_2$ the incoming ion with Z_1 becomes a stopped interstitial atom.

The last assumptions made concernethe case of $E_1 < E_d$ and $E_2 < E_d$. In this case, the incoming ion becomes an interstitial and the energy $E_1 + E_2$ is released as phonons.

1.7. Polymers

Typically, a polymer is a molecule which consists of directional, covalent bond components, called monomers; see Figure 1.51. The number of monomers of which a polymer must consist is clearly defined, but the degree of polymerization, which is the number n of monomer units, must be high enough so that a change by one monomer does not affect the physical or chemical properties of the macromolecule. The properties of such polymers depend on various factors, such as the monomer units contained, the degree of polymerization or the nature of the chemical binding.

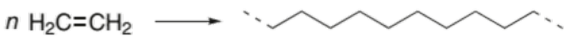

Figure 1.51.: *Example of building a polymer by repeating a monomer [20].*

1.7.1. Polymer Structures

1.7.1.1. Linear and Branched Polymers

Beside the wide range of chemical properties, polymers can be distinguished by their molecular architecture, which can be 1) linear, 2) unbranched with exactly two ends or 3) cross-linked, which is achieved during synthesis by adding a trifunctional monomer for the generation of branching sites. In this case, one can define three different sites depending on the proximity behavior: linear, branched and terminal parts, which is

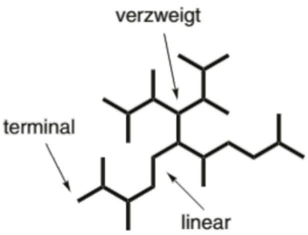

Figure 1.52.: *Schematic illustration of linking, including branched, linear and terminal parts of a polymer [20].*

illustrated in Figure 1.52. The higher the ratio of linear to branched segments, the higher the branching factor is, which leads to an ideally branched, symmetric macromolecule, which grows from a central point outwards like a dendrite, see Figure 1.53, to a point where the density of links suppresses further growth.

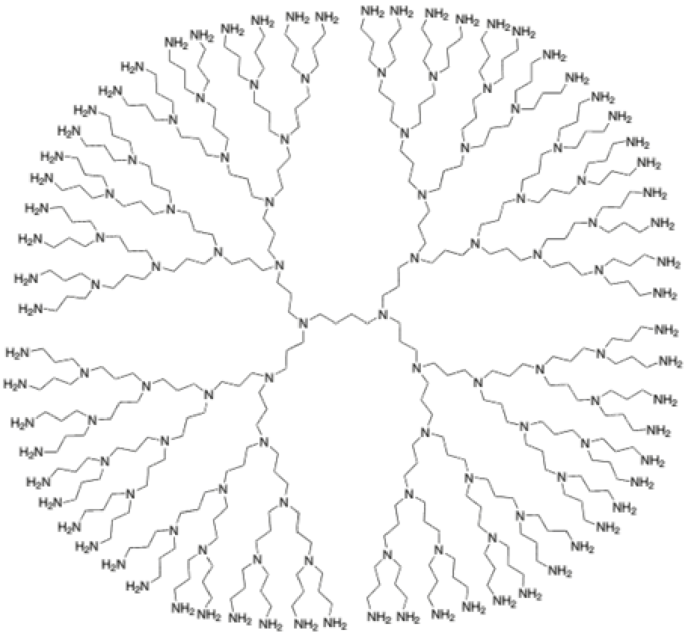

Figure 1.53.: *Schematic drawing of a dendrite structure [20].*

1.7.1.2. Isomerism of Polymers

From a chemical point of view isomers are molecules with a different chemical structure, but with the same molecular formula, which can affect the polymer properties considerably. For macromolecules one can distinguish between different types of isomerism:

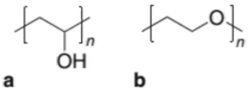

Figure 1.54.: *Structural isomerism using the example of polyvinyl alcohol (a) and polyethyleneglycol (b) [20].*

Structural Isomerism: The distinguishing feature of this type of isomerism is the nature of the covalent bonding between atoms, as can be seen in Figure 1.54. Typically, these isomers do not occur in pure form, thus most of the polymers consist of a variety of structurally varied isomers.

Stereoisomerism: These constitutionally equivalent molecules are distinguished based on their geometric arrangement. What is important for polymers is basically the cis-trans-isomerism with a double bond at the backbone, as is illustrated by polybutadien in Figure 1.55.

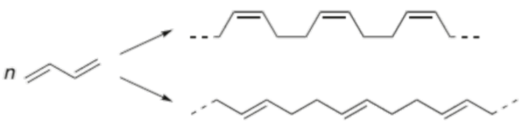

Figure 1.55.: *Cis-trans-isomerism of (a) cis- 1,4- polybutadien and (b) trans-1,4-polybutadien [20].*

Figure 1.56.: *Stereoisomerism of polypropylene: isotactic, syndiotactic and atactic polypropylene [20].*

A second type of stereoisomerism is enantiomerism, which occurs, in polypropylene (**PP**) for example. During the synthesis of PP a backbone is built, which formally is planar. The methyl groups can be arranged upwards or downwards and, depending on the configuration of these methyl groups, isotactic (it), syndiotactic or atactic (at) PP is formed; see Figure 1.56. While it-PP is highly crystalline and the melting point is approximately 160°C, at-PP has a very irregular structure and forms an amorphous, gluey material.

Conformational Isomerism: In macromolecules, molecule groups can rotate around single bonds, as can be described by the simplest organic polymer, polyethylene (**PE**). The all-trans conformation is actually enthalpically preferred, but, due to the extremely high number of variation possibilities, very unlikely. Thus, a significant part will consist of gauche conformation, forming a ball-like molecule structure, as is illustrated in Figure 1.57.

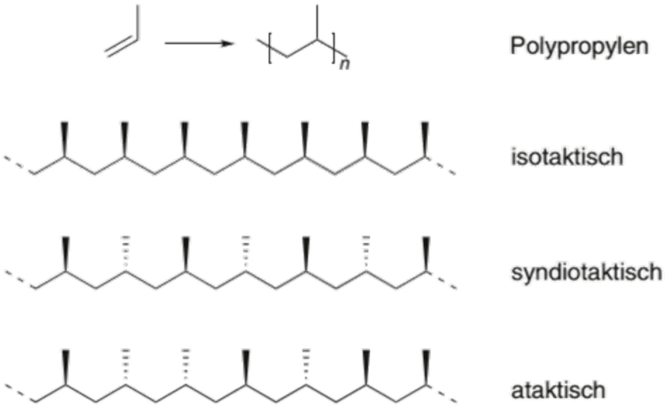

Figure 1.57.: *(a) all-trans- conformation and (b) ball - like conformation of polyethylene [20].*

1.7.1.3. Copolymers

Copolymers are polymers that consist of at least two chemically different monomers. By combining different monomers, a wide range of macromolecules with various properties can be synthesized. Not only the types of monomers are important, but the arrangement of the different units is a key factor for varying polymer properties.

Statistical Copolymers: A statistical copolymer consists of monomers which are arranged randomly to form the polymer, as is shown schematically in Figure 1.58. Only the ratio of reactivity of the monomers during the synthesis affects the sequence.

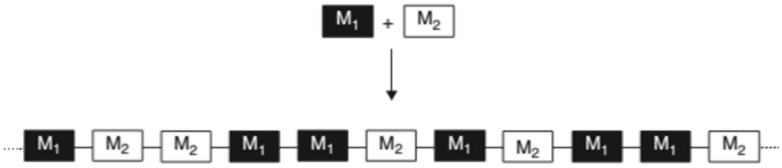

Figure 1.58.: *Statistical copolymer built from 2 monomers M1 and M2 [20].*

Alternating Copolymers: These special types of polymers consist of monomers which are arranged alternatingly and regularly to form the polymer backbone; see Figure 1.59. This sort of polymers is mainly synthesized from monomers, which can only react with other monomers but not with themselves.

Figure 1.59.: *Alternating co-polymer consiting of monomers M1 and M2 [20].*

Block Copolymer: The monomers are arranged in blocks completely separate from the polymer backbone so that each block is formed of just one type of monomer, as is illustrated in Figure 1.60. Depending on the number of blocks, these are called di -, tri-or multiblockcopolymers.

Figure 1.60.: *Block copolymer formed from two monomers M1 and M2 [20].*

1.7.2. Phase Transition in Polymers

Basically, polymers in a solid state can be classified into three categories: mono-crystalline, semi-crystaline and amorphous. The mono-crystalline state can only be achieved during crystallization out of a dilute solution and is of minor importance. The crystallization of polymers is a very complex and slow process due to the long molecule chains and the entanglements which have to be healed. Typically, a full crystallization is not achieved; thus, the polymer stays in the semi-crystalline state, in which crystalline and amorphous parts exist.

A very important distinguishing feature is the phase transition. In crystalline materials, heating involves a melting point (T$_m$) at which the crystalline structure is dissolved into an unordered state and volume and properties are changed dramatically. Thisis a first order phase transition. In contrast, an amorphous polymer is innately in an unordered state and no change in structure occurs by heating. The temperature at which polymer chain rearrangement occurs is called the glass transition temperature (T$_g$). This type of transition is of second order because no transition enthalpy is required for breaking up the crystalline structure. Thus semi-crystalline polymers possess both a melting and a glass transition temperature, whereby the glass transition temperature is always lower than the melting temperature. Otherwise a melt would solidify to a glassy state and by cooling a transition to a crystal would have to occur, but below T$_g$ the energy is too low for a rearrangement of the polymer chains and thus crystallization is suppressed.

1.7.2.1. Determination of T$_g$ and T$_m$

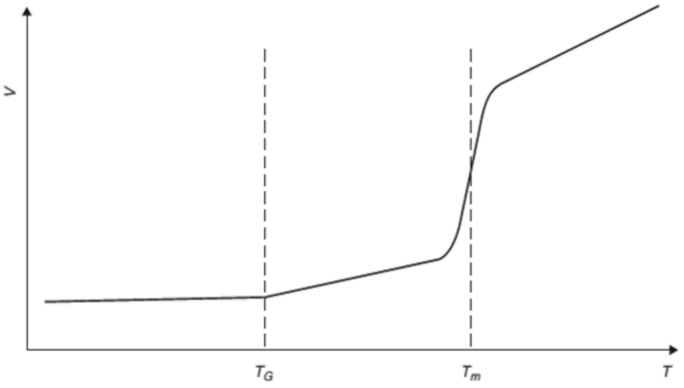

Figure 1.61.: *Schematic representation of the volume change at the glass transition temperature and melting point for a semi - crystalline polymer [20].*

A very commonly used technique for the determination of T$_g$ and T$_m$ is differential scanning calorimetry (**DSC**). This method is based on the measurement of the conduction of heat which is required for a constant heating rate. This conduction of heat correlateswith the heat capacity, which is the heat required for a change of temperature. At T$_g$, a kink of the heat capacity slope in a plot vs. temperature is observed, whereas at T$_m$ latent heat has to be supplied, which leads to a constant temperature during the melting process until the crystalline structure is completely melted and the change to an anisotrope melt is completed. Thus, formally the heat capacity divergesto infinity leading to a peak in DSC and the area beneath the peak can be assigned to the latent heat of fusion. A very important advantage of DSC is the ease of use and the small amount of sample required for measurement. A schematic DSC graph is shown in Figure 1.61.

1.7.3. Semi-Crystalline Polymers

Due to the fact that during crystallization a transition to a highly ordered state occurs, the entropy of the transition is negative. This has to be compensated by a negative enthalpie of crystallization and an exothermic crystallization implies an interaction of the polymer chains in the crystalline state. This can be achieved by either symmetric chains due to the high packing density, or by strong interaction between chains. Thus, polymers which are rather flexible tend to build amorphous phase or crystallization is going on very slowly. Classically, crystallization is a two-step process: first is the nucleation, where nuclei of crystals are formedwith a critical minimum size. This nucleation can also be achieved by adding additional substances, which initiates initial crystallization effects. The second step is the growth of these crystal nuclei, which is substantially dependent on the process temperature. In the following, factors are described which influence the melting temperature.

1.7.3.1. Influences on the Melting Temperature

Crystallization Condition: Crystallization can be achieved in a temperature range of approximately 30°C above to 10°C below the melting point. Any further below this, the mobility is too constrained, for a polymer to crystallize, whereas at higher temperatures, the mobility is too great for crystallization. Basically the crystallization of polymers is a slow process compared to low-molecular materials; thus, the degree of crystallization can be controlled by the cooling rate. With a fast cooling rate, the polymer will cool down too fast to form a well-ordered system. In extreme cases, the polymer can even end up in a totally amorphous state. Beside this effect, fast cooling rates cause many very small crystalline segments to be formed. This decrease the melting temperature due to their high surface energy compared to larger crystals. Thus T_m can be decreased up to 30°C by high cooling rates. These effects are mostly suppressed by a slow cooling rate, forming a more precise melting point.

Chain Flexibility: The chain flexibility has an essential influence on the enthalpy of crystallization. As the degree of order in a crystal is higher than in a melt, the loss of entropy is more pronounced with a higher amount of conformations, which can be generated out of a polymer chain. Thus, if the difference in energy between trans states and gauche states is low, see section 1.7.1.2, the polymer tends to become ball-like and a low melting point results.

Symmetry: Asymmetric polymer backbones cannot be perfectly fitted into a crystal structure, thus T$_m$ will be decreased by the distortion of crystallinity. This effect is even more distinct for polymers which tend to exhibit bending of the polymer backbone.

Chain and Chain Segment Interaction: The formation of hydrogen bonds or dipole-dipole interactions leads to a severe change of the melting point. For example in polyamide 6,6, see Figure 1.62, a strong network of hydrogen bonds is formed throughout the whole material leading to a melting point of 267°C, whereas polyethylene, without hydrogen cross-linking melts at 137°C.

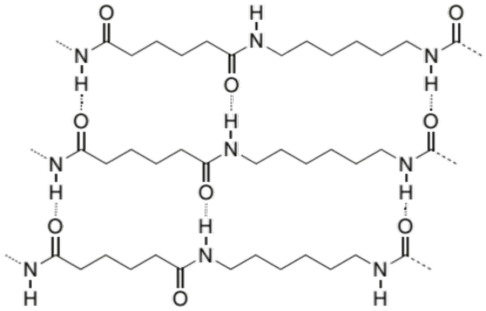

Figure 1.62.: *Schematic drawing of a network of hydrogen bonds in polyamid 6,6 [20].*

Tactility: Isotactic polymers are basically formed of a helical superlattice to minimize interactions between the outpointing substituents, and the helices form the crystalline structure. For syndiotactic polymer chains, these substituents are farther apart leading to a more zig-zag like conformation. In principle, atactic polymers cannot crystallize due to their irregular structure.

Branching Generally compact and branched side chains lead to a stiffening of the polymer chain and thus to an increase of T$_m$, whereas long and flexible side chains induce a distortion of the crystal lattice and thus are responsible for a decrease of T_m. Another important point is that a branched polymer chain leads to a decrease of packing density and thus the enthalpy of crystallization as well as the melting point is decreased. A good example for this effect is polyethylene (**PE**). Through branching to low-density polyethylene (**LDPE**) a melting temperature of 110°C is achieved, while linear low-density polyethylene (**LLDPE**), which is less branched, melts at 122°C.

Molar Mass: Polymer chain ends are rather mobile in comparison to the segments at the center of the chain; thus the crystal lattice is disturbed and crystallinity is distorted. A decrease of T_m with low molar masses is a result of thermodynamics superposed by kinetic effects, as polymers with very high molar masses tend to crystallize very slowly.

All these determining factors lead to a different melting temperature of chemically identical polymers. Especially the molar mass, the degree of branching, the tactility and the thermal history are of particular importance.

All these determining factors lead to a different melting temperature of chemically identical polymers in literature. Especially the molar mass, the degree of branching, the tactility and the thermal history are of particular importance.

1.7.3.2. Morphology of Semi-Crystalline Polymers

In principle, the entanglement of polymer chains is primarily responsible for the failure to generate a fully crystalline material during the cooling process of a melted polymer; in contrast, amorphous segments are formed, which can vary in size. The crystalline part of the polymer system primarily forms a lamellar structure. These lamellas are usually approximately 100 nm thick and the thickness increases with the crystallization temperature. In principle, the polymer backbone is aligned orthogonally to these layers; see Figure 1.63. Critical for crystallization into this layered structure is the fact, that the entanglement of neighboring polymer chains cannot be fully distorted. Thus, the complete polymer backbone is not able to get aligned to a crystal structure, but segments of the chains can be aligned parallel without changing the position of the chain leading to solidification.

As already covered in section 1.7.2, the amorphous part of a polymer forms a high viscous melt above the glass transition temperature, while in contrast, the crystalline domains remain solid until the melting temperature is reached, which is higher than

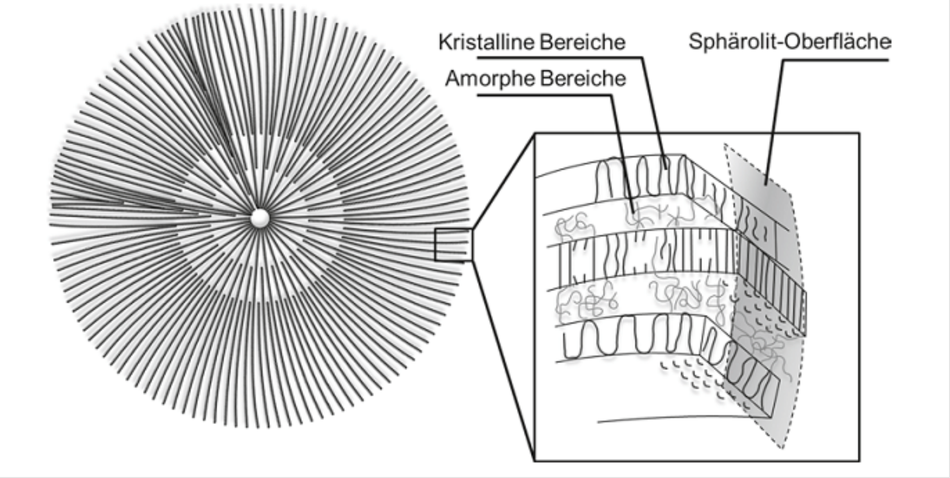

Figure 1.63.: *Drawing of a spherulitic superstructure of a semi-crystalline polymer [20].*

the glass transition temperature, leading to a stable concomitance of a liquid and a solid phase. This phenomenon leads to outstanding mechanical properties, such as a very high ductility of polymers between T_g and T_m. The crystalline lamellas often form superlattices, such as spherulites, which are ball - like structures, shown in Figure 1.63. Beside these spheres, also one and two dimensional superlattices, such as fibers or disks.

1.7.4. Amorphous Polymers

In the amorphous phase the polymer chains are fully entangled and thus the mobility of the chain segments is suppressed leading to a very high brittleness. Thus, a low percentage of strain will already result in a cracking of the polymer sample. In a frozen state, the polymer chains do not have any short or long-range order.

1.7.4.1. Glass Transition Temperature

Below T_g the entanglement inhibits the motion of polymer chains, leading to this very brittle behavior, whereas above this temperature, a transition to a state with polymeric motion occurs resulting in a very high viscosity of the material. Due to the inhomogeneous material in an amorphous polymer, some parts of the sample will become mobile earlier than others, leading to an instable transition range in which the mechanical properties, or other factors such as the specific volume, the heat capacity or the refraction index, can vary severely and abruptly. Factors affecting T_g are discussed below.

Chain Flexibility: In principle more flexible chains are more mobile, resulting in low glass transition temperatures. This chain stiffness can be increased by adding stiff segments into the polymer backbone as aromatic rings, as is shown in Table 1.4.

Table 1.4.: *Influence of linear substituents on the glass transition temperature of polymers with a (CH_2-CH-X)$_n$-structure.*

-X	**T_g [°C]**
-H	-93
-CH_3	-20
-C_2H_5	-24
-C_3H_7	-40
-C_4H_9	-20

Steric Effects/Substituents: By varying flexible side chains, the free volume available for motion is increased and thus the glass transition temperature is decreased. Due to the tendency of polar substituents to form hydrogen bonds and dipole-dipole interactions, T_g is influenced by the stronger fixation of the polymer in its position. Due to this decreased mobility, T_g will be decreased.

Softener: A softener is a low-molecular, non-volatile bond added to a polymer to influence the sample properties, such as inducing a lubricating effect between polymer chains. This additional component leads to increased mobility, which results in a decrease of T_g.

1.8. Methodology

1.8.1. Dual Beam Microscope

The FEI NOVA 200 nanolab dual beam microscope shown as a photo in Figure 1.64 (and illustrated in Figure 1.1), was used for the fabrication of structures with the ion beam and the investigation with the electron beam as well asthe TEM lamella preparation. The electron source in this microscope is a field emission gun (**FEG**) and is capable of electron energies in the range of 1-30 kV. The electron current can be varied from 2.5 up to 37,000 pA resulting in beam diameters down to 1.2 nm (FWHM). The ion beam column uses Ga$^+$ ions and is capable of varying the ion beam energy from 5 to 30 kV with a beam current of from 0.15 up to 20,000 pA resulting in a beam diameter down to 7 nm.

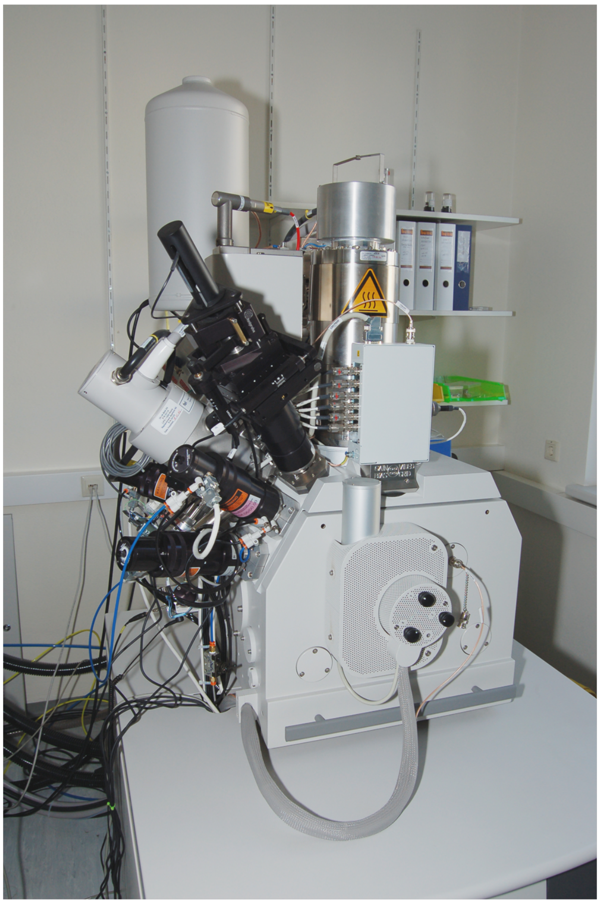

Figure 1.64.: *Dual beam microscope used, FEI NOVA 200 Nanolab.*

The DBM is equipped with a ETD and a TLD detector and both were used as imaging detectors for the electron beam imaging and ion beam imaging. Electron beam imaging was done, if not described elsewise, with 5 kV and 98 pA, which is a rather low current, but was used to minimize electron beam damage on the polymer samples as a higher current is harmful. The ion beam imaging was done with 30 kV and a current of 10 pA leading to a good compromise between sputtering and image quality in the sense of contrast. In the ion beam imaging, only one frame was recorded to minimize unwanted structure deformation in the imaging process.

1.8.1.1. Patterning

All the structuring was performed at the eucentric height of 19.3 mm. If not otherwise stated, the fabrication of structures was performed at 30 kV and 500 pA, which were chosen due to provide a good compromise between the evolution of the investigated effects and the time consumed for producing the structures. Other experiments with 50 pA are also presented later and in the optimizing process of the interlacing strategy the current was also varied.

For cryogenic temperature experiments at -150°C the variable temperature stage designed in-house was used. To ensure reliability, the samples were kept on the stage for one hour after reaching the target temperature before focused ion beam structuring started.

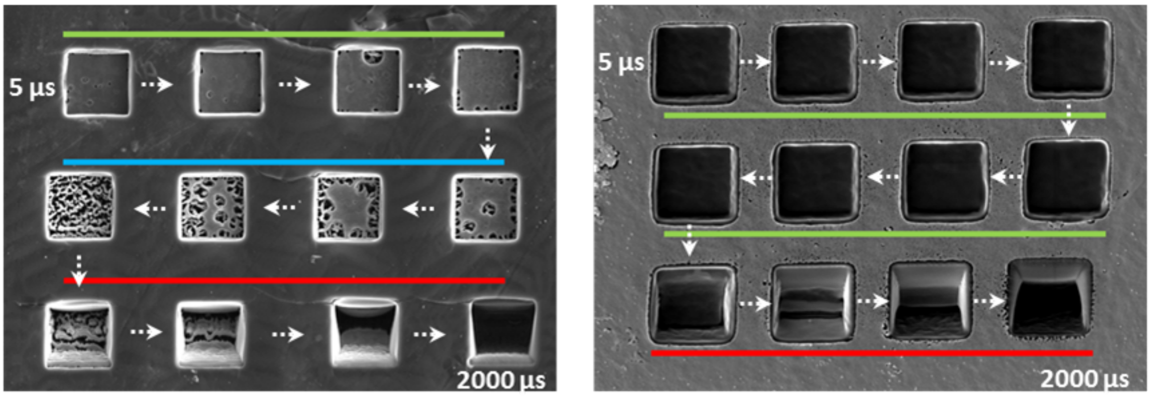

Figure 1.65.: *$5\times5\,\mu m^2$ structures with different DT ranging from 5 to 2000 s on PMMA (left) and HDPE (right) with a colored marking of the three different regimes revealing different morphologies: green is the short thermal/degrading regime, blue is the middle thermal/degrading regime and red the high thermal/degrading regime. See [32] for further details.*

For the dwell time (DT) and point pitch (PoP) sweep, a 12 field array was used, as shown in Figure 1.65, and the values were varied from 5 to 2000 μs, respectively. The structures have been fabricated in a $2\times2\,\mu m^2$ squared shape allowing the investigation via SEM, Raman spectroscopy and atomic force microscopy.

For generating a cross-section via ultramicrotomy structures of $2\times10\,\mu m^2$ have been fabricated, due to the difficulty of finding the structures in the ultramicrotome. The total exposure time was adapted leading to the same dose per area as in the squared structures.

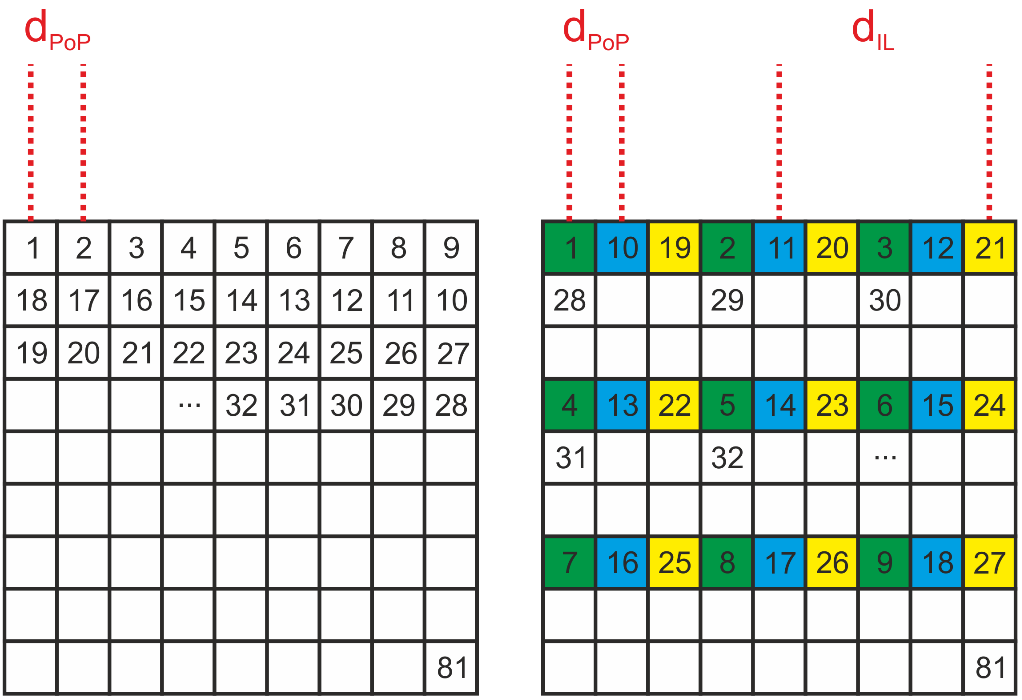

(a)

(b)

Figure 1.66.: *(a) Schematic illustration of a classical serpentine scan and (b) schematic illustration of the alternative interlacing strategy.*

The internal patterning engine was used for the standard processing offering 16-bit resolution for points in the X and Y direction, whereby the interlacing strategy invented was applied via stream files which control the D/A patterning board directly. The standard rectangle is rastered in a serpentine manner, as is illustrated in Figure 1.66 (a), and the new interlacing (**IL**) strategy uses an interlacing point pitch (**ILPoP**) large enough to prevent pattern induced effects. After such an IL frame has been finished, the entire pattern is shifted by a small value according to the desired PoP; see Figure 1.66 (b) for an illustration. For ease of operation, a stream file generator was programmed first in C++ and further developed with MatLab routines and a graphical user interface was created via Visual Studio 2012.

1.8.1.2. TEM Lamella Preparation

The DBM is additionally equipped with gas injection systems, from which the trimethyl-methylcyclopentadienyl-platinum (MePtCpMe3) precursor was used for the fabrication of a protective layer in the TEM lamella preparation. The TEM lamella preparation, see

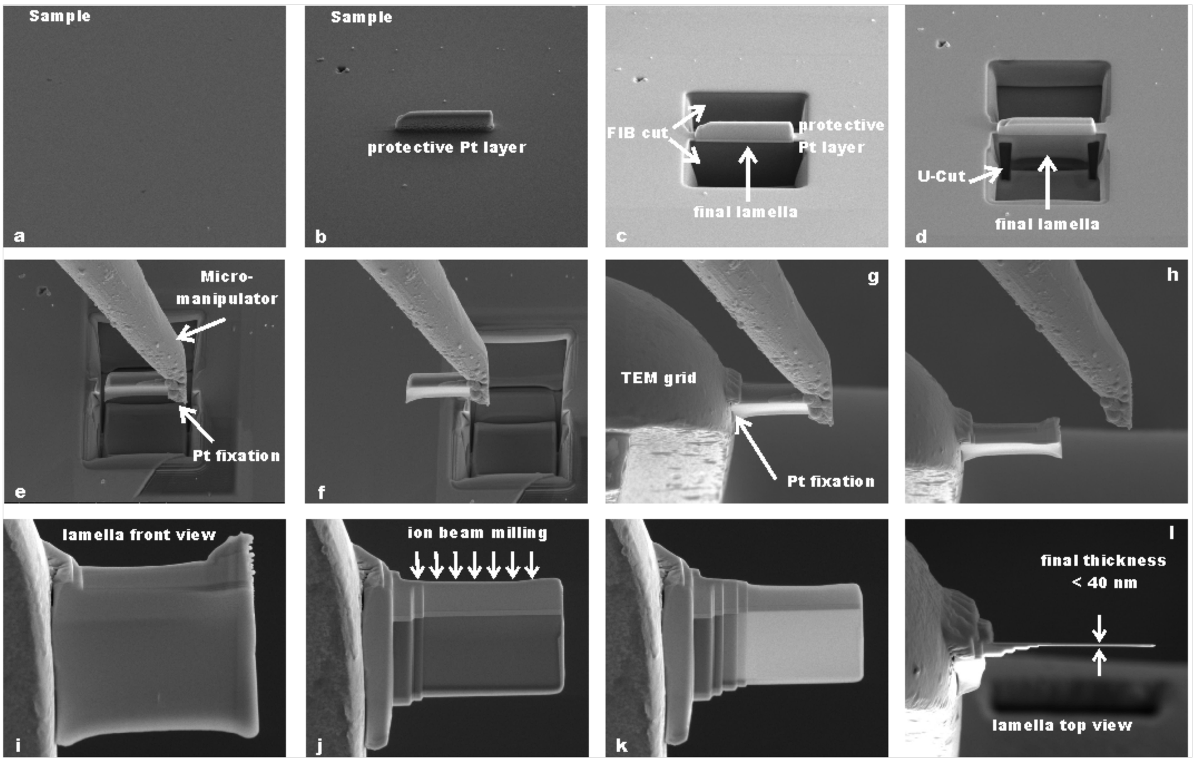

Figure 1.67.: *(a) sample position to be investigated, (b) deposition of a protective Pt layer, (c) milling of coarse lamella, (d) precutting of the lamella, (e) bonding to omniprobe and disconnecting from sample, (f) lift out, (g) fixing the lamella to a TEM specimen holder, (h) disconnection of the omniprobe, (i) approximately 500 nm thick lamella on the TEM specimen holder, (j) & (k) thinning to electron transparency, (l) 40 nm or thinner lamella ready for TEM investigation.*

Figure 1.67, was performed with the most commonly used technique by depositing a Pt protective layer and milling a coarse lamella. Afterwards, the lamella was precut by a so-called U-cut and bonded to a micromanipulator. By cutting it free, the lift-out can be performed and it can be fixed on a TEM grid. On this grid the lamella then is thinned down to a thickness of approximately 50 nm. OMNIPROBE 3 post copper grids have been used as TEM grids, in which fall posts except the center position were cut away with a scalpel or the upside-down preparation.

1.8.2. Transmission Electron Microscope

For TEM investigations, an FEI Tecnai F20 (S)TEM was used. It was equipped with a Schottky FEG operated at a high voltage of 200 kV. Furthermore it is equipped with a monochromator, a high angle annular dark field (**HAADF**) and a bright field (**BF**) detector and a high resolution Tridiem Gatan Imaging Filter (**GIF**) for EELS and energy filtered TEM (**EFTEM**) and a conventional EDXS (SiLi) detector from EDAX for chemical analysis.

The second TEM used was a FEI Titan^3 60 - 300 (S)TEM which is equipped with a X-FEG high brightness Schottky field emission source and was operated at 300 kV. In this microscope a monochromator, a Cs-probe corrector for high resolution STEM imaging, several HAADF and BF detectors and a Gatan GIF Quantum energy filter system for EELS and EFTEM imaging were employed. For further chemical analysis ChemiSTEM technology was used, which is a combination of the X-FEG, a special silicon drift EDX detector and fast mapping electronics.

1.8.3. Atomic Force Microscope

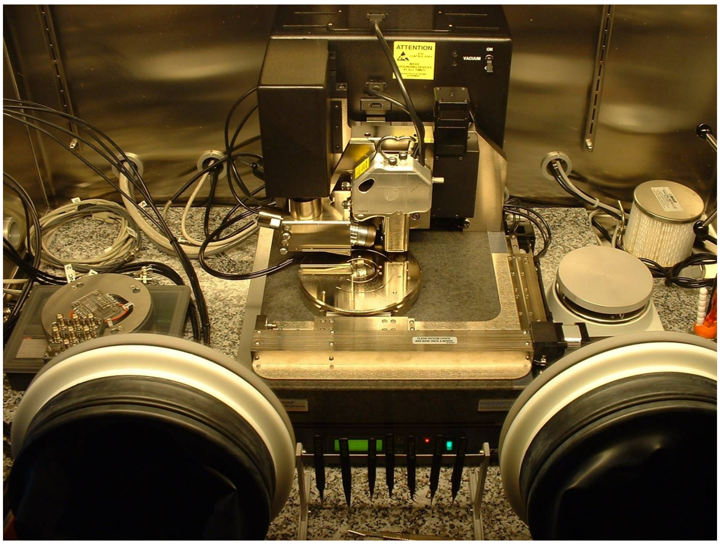

Figure 1.68.: *Atomic force microscope used - Bruker AXS Dimension 3100 with Nanoscope IV controller.*

For AFM investigations, a Dimension 3100 System from Bruker AXS with a Hybrid XYZ scan head was used; see Figure 1.68. This AFM was placed on an active vibration isolation plate to minimize mechanical vibrations and was equipped with an Nanoscope IV controller, which was placed in the room next to the operating room, to avoid acoustic and mechanical vibrational influences.

NanoScope Analysis v1.20 was used for analyzing the recorded files and Gwyddion 2.30 was used for reprocessing by flattening and plane fitting to obtain a proper image quality.

A cross-section of the structures was measured to obtain the structure depths. Image resolution was kept constant at 512 pixels and lines, also allowing KPFM measurements in interleave mode with this resolution

For botz, topographical and KPFM measurements, Olympus tapping tips (OMCL-AC240-TS) were used, which have a resonance frequency of approximately 70 kHz and a spring constant of approximately 2 N/m. Their tip radius is less than 10 nm.

1.8.4. Raman Spectroscope

Raman spectra were measured using a Horiba Jobin Yvon LabRam 800 Hr spectrometer with an Olympus BX41 microscope and a 633 nm He-Ne laser excitation with a 17 mW nominal power output. The objective used was an Olympus MPlan N x100 with NA 0.9. The slit width was 100 μm and the pinhole was closed to 200 μm.

In order to avoid any damage caused by the laser beam, an ND 2.0 filter was used for the measurements. Comparability was ensured by performing all measurements under identical conditions and by collecting the spectra within the region of 2500-3000 cm^{-1} at 3×150 s integration time. The integral intensities were calculated using the standard integration function supplied by the LabSpec software. The spectral region between 2700 and 3000 cm^{-1}, related to CH_2 and CH_3 stretching modes, was chosen as a measure for the remaining polymer. Integral intensities were calculated as the area above a linear background between the two border frequencies.

1.8.5. Ultramicrotomy

Ultramicrotomy was performed on a MICROTOME not for the preparation of ultrathin cuts for TEM investigations, but to produce Cross-sections of FIB produced structures for the AFM investigations. Therefore the HDPE sample was embedded in different materials shown in Table 1.5 as they are embedding materials for cold embedding. All of them are made out of two components, but EPOFIX and SPEZIFIX contain Cl. Their hardening time and temperature can be seen in Table 1.5.

In additions a temperature variation was performed for optimizing the cutting process and getting the best results for AFM investigations, which requires very flat surfaces, especially when investigations with Kelvin Probe Force microscopy are needed. Also,

Table 1.5.: *Embedding materials used for ultramicrotomy cuts.*

Material	**Temperature** **°C**	**Time** **h**
SPURR	70	8
EPOFIX	60-70	12-24
SPEZIFIX	40-60	3-4

preparations with or without an oscillating knife were performed to get rid of highly unwanted artefacts.

1.8.6. Simulations

1.8.6.1. Finite Element Simulations

First simulations with the FEM method were performed with the software package ANSYS V13 for PP samples only. The sample was modeled by an axissymmetric line with a length of 1 mm and a depth of 1 mm and later was meshed by the software's automatic meshing algorithm. In order to reveal temporally resolved temperature distribution in a first approximation, a hemispherical volume according to the FWHM beam diameter of the ion beam provided by the manufacturer at 39 nm was heated up to a predefined target temperature according to the estimation by Volkert et al. and Kim et al.[17] within a time corresponding to the beam dwell time. Thermal conductivity and specific heat capacity were assumed to be 0.22 $\mathrm{Wm^{-1}K^{-1}}$ and 2.5 $\mathrm{kJkg^{-1}K^{-1}}$, respectively, in compliance with Khoury et al. [15].

Subsequently, the temporal and radial temperature distribution was normalized to the starting value in order to provide relative values instead of absolute temperatures, which are extremely complicated to verify through experiments. In order to get a more sophisticated estimation, a calculation considering Gaussian ion beam profiles instead of circular area as well as SRIM simulations as input data was performed, as is discussed in the following section.

1.8.6.2. Combined Thermal Spike Approach

In this approach the interaction volume and the phonon distributions were simulated using the SRIM/TRIM 2013 package resulting in a spacial resolution of 1.5 . The $\mathrm{Ga^+}$

ion beam was simulated at 30 kV with a Gaussian beam profile normal impinging on the sample and a FWHM of 40 nm, which is the beam diameter provided by the manufacturer. All simulations were performed via 10,000 ions to derive individal interaction volumes and phonon distributions. Although the latter notation is not fully applicable for amorphous polymers, the term phonons is used in this thesis for simplicity to describe atoms which temporarily leave their original position due to inelastic scattering in analogy to crystallographic materials. The related energy is transferred to oscillations of the polymer backbone by returning to its primary position. Thermal spike calculations were performed using MATLAB release 2012b and using the phonon distribution of SRIM/TRIM simulations as the energy loss input. The calculations were done for a radial-depth 2D plane and 0.2 ps was used as a time scale for the thermal spike. For the thermal conductivity and specific heat capacity used, see section 1.7.

2. Results

2.1. Pristine Polymer Sample Characterization

The polymers for this study have been chosen considering various aspects: morphological, chemical, and thermodynamics. The morphology aspect can first be covered via AFM and does not imply any restrictions. Fast characterization via SEM, however, is much more prone to material damage and limited the material selection. Second, thermodynamic characterization was performed via STA which also does not limit the material selection in general. However, to allow reliable material characterization by means of glass transition points T_g, melting points T_m and volatizing thresholds T_v (as described in section 1.7) chemical simple polymers were preferred. The volatizing threshold was measured at the onset of material loss in the TGA measurements. In particular, as temperature effects are the focus of this thesis with the purpose of structuring polymers with the lowest melting points, materials have been chosen with melting points from 65°C up to 270°C. Chemical investigations via TEM but in particular via Raman spectroscopy as a very sensitive method for varying chemical bonds further confined the range of appropriate polymers. The most important aspects, however, were the chemical behavior during heating, which can basically be divided into chain scission and cross linking as extreme processes. Taking all demands into account, we chose 6 polymers in total: polypropylene (**PP**), polyethylene (**PE**), polymethylmetacrylat (**PMMA**), polyethylene oxide (**PEO**), ethylene vinyl acetate (**EVA**) and polystyrene (**PS**). These materials are discussed in the following concerning their thermodynamic behavior and its suitability for dedicated experiments.

For FIB experiments, all materials were initially embedded in standard embedding material (EPOFIX) unless otherwise stated. Subsequently, the samples were mechanically polished with a coarse-grained abrasive paper followed by a stepwise decrease of grain size, resulting in a very flat surface roughness. This is essential for investigations in AFM but also beneficial in SEM and RS. All process steps were done with slow rates and with water co-flow whenever possible to reduce an increase of temperatures, which could alter the polymers already during preparation. Due to the low electric conductivity of polymers, coverage with a thin carbon layer ($< 10\,\mathrm{nm}$) was essential to provide SEM / FIB operation without massive charging and often entailed material degradation due to excessive local charging.

2.1.1. Polypropylene

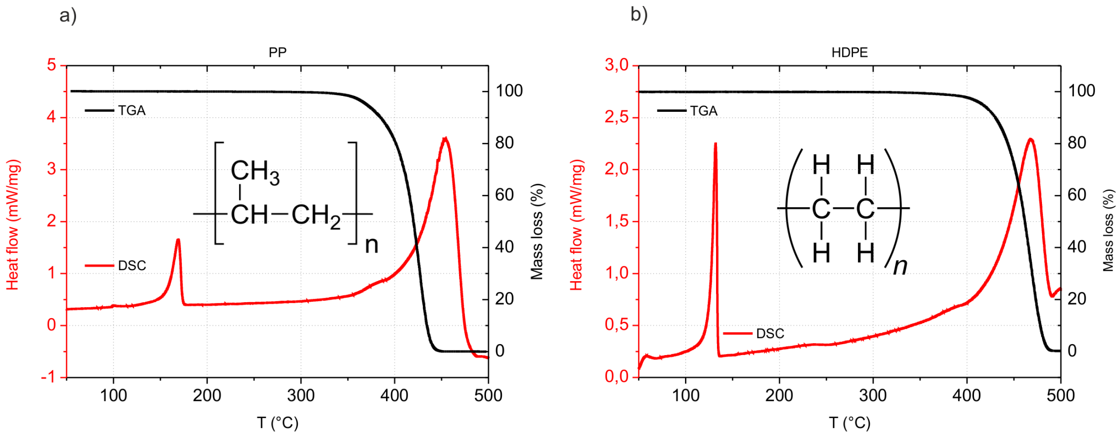

Figure 2.1.: *Chemical formula and combined DSC (red) / TGA (black) characterization of (a) polypropylene (PP) and (b) high-density polyethylene (HDPE).*

Polypropylene (**PP**), see Figure 2.1 (a), is one of the most commonly used types of polymers. It is used commercially in a wide variety of applications, such as packaging, labeling, textiles, re-usable containers but also in laboratory equipment or polymer banknotes. Due to the fact that it is made of the monomer propylene, it is chemically very stable and resistant to many chemical solvents, bases and acids.

Typically the PP used is isotactic and semi-crystalline, with a crystallinity between low-density polyethylene and high-density polyethylene. Depending on the crystallinity and the atacticity the melting point is in the range of 160 - 170°C. We used three different kinds of PP, which differ only in terms of their molecular mass, leading to slightly different T_m and T_v. As an example, the TGA and DSC of the PP with the intermediate molecular mass can be seen in Figure 2.1 (a). In our case, three different polypropylene samples were used with variation in the average molecular weight and thus in the mass flow index. Due to these slightly varying thermodynamic properties with a constant chemical structure, fine investigations of removal rates using different process parameters and sample temperatures (room temperature → - 150°C) were possible, which was the main reason for choosing this polymer.

Due to the large sample size, no embedding was necessary which reduced the preparation to careful mechanical polishing and subsequent carbon film coating.

2.1.2. Polyethylene

Polyethylene (**PE**), see Figure 2.1 (b) for the chemical structure, is used in more than 70 % of the total plastics market and it is used in a wide variety of applications, such as many household products. Many different isomers of PE exist, such as high-density (**HD**), low-density (**LD**) and linear low-density (**LLD**) PE, which differ in terms of branching. LLDPE has the lowest branching and thus lowest packing density while a high packing density is obtained through highly-branched chains. The branching is suppressed by an appropriate choice of the catalyst and reaction conditions.

In our case, HDPE was chosen due to the mid-range melting point of 130°C, whereas LLDPE and LDPE have a T_m in the range of 110-120°C. Figure 2.1 (b) also shows the DSC and TGA of the HDPE used, which was ordered from "ALFA AESAR" revealing its T_m and T_v. HDPE is known for its high strength to density ratio, with a density ranging from 0.93-0.97 g/cm^3 and due to its high density and thus melting point it can withstand higher temperatures than (L)LDPE. The sample expanded PP investigations at varying sample temperatures (room temperature → - 150°C) due to its different thermodynamic properties.

Preparation was done by embedding in epoxy, cutting and mechanical polishing. Afterwards the sample was coated with an approximately 5 nm thin layer of carbon and fixed with conductive carbon tape on a SEM sample holder, allowing charge transfer from the sample to ground of the DBM, thus minimizing charging effects. The sample preparation for the low temperature experiments was done in the same way as for PP.

2.1.3. Polymethylmethacrylate

Due to the its suitability as a resist for photo- and e-beam lithography polymethylmehtacrylate (PMMA), see Figure 2.2 (a), is the most challenging material used in this thesis. As it undergoes an extremely clean scission process with a monomer yield of almost 100 % during exposure to an energetic electron beam and/or applied temperature,

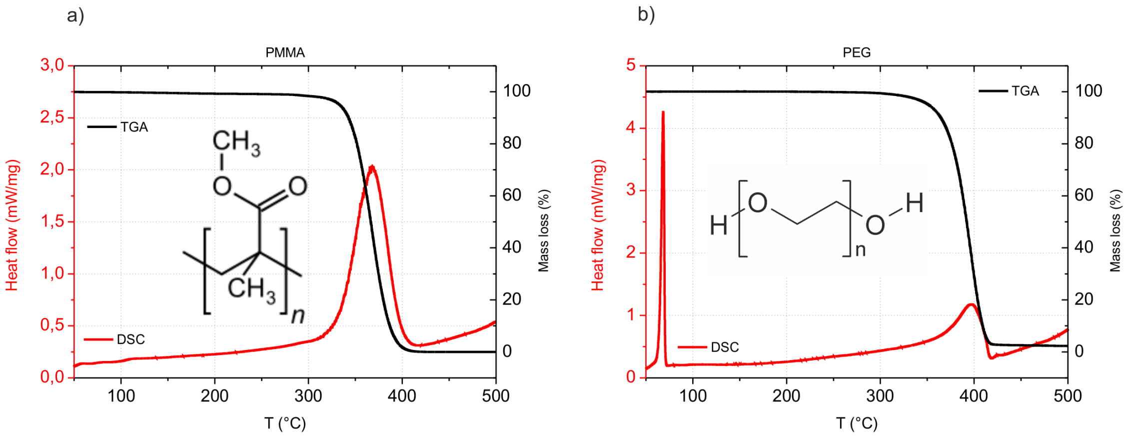

Figure 2.2.: *Chemical formula and combined DSC (red) / TGA (black) characterization of (a) polymethylmethacrylate (PMMA) and (b) polyethylene oxide (PEO).*

material modification is very fast. Thus, care had to be taken during preparation and processing while e-beam inspection was entirely prevented. The volatizing threshold and glass transition temperature were also determined by STA analysis, see Figure 2.2 (a), revealing a T_v of 310°C and a T_g of 120°C.

2.1.4. Polyethylene Oxide

polyethylene oxide (PEO or polyethyleneglycol PEG), see Figure 2.2 (b), is a non-toxic, water soluble polymer which is often used in biological and especially medical contexts. PEO is a very good example for crystallization to spherulites. Results in [10] indicate packed antiparallel helical strands with opposing handedness in which oxygen atoms reside in the core of the helix with surrounding hyrdophobic methylene groups. The growth of these spherulites can be understood to be a continuous folding action after a single crystal is formed and crystal defects lead to a lamellar twisting and branching. Fibrillar helical structures are thus formed which successively twist around, and continuous growth yields a spherulite which then grows as a sphere.

PEO is very reactive to exposure to energetic e-beams and/or temperatures leading to a slightly dominating chain scission. PEO exists in a variety of average molecular masses which change its physical properties, especially the melting point. In our case an average molecular mass m_w of 35,000 gmol^{-1} was used with a melting point and volatizing threshold of 68°C and 330°C respectively, as revealed by STA measurements in Figure 2.2 (b).

The preparation of PEO was different compared to the other samples due to the fact that it was only available as flakes. Thus it had to be melted on a hot plate at 110°C between two silicon substrates to ensure a very flat sample surface. This sandwich-like construction was then shock cooled in liquid nitrogen to prevent phase transitions observed at slow cooling. By taking off the top silicon wafer, a very flat surface of PEO was obtained, although crystallization to spherulites could not be prevented, as representatively shown in Figure 2.3 by light microscopy.

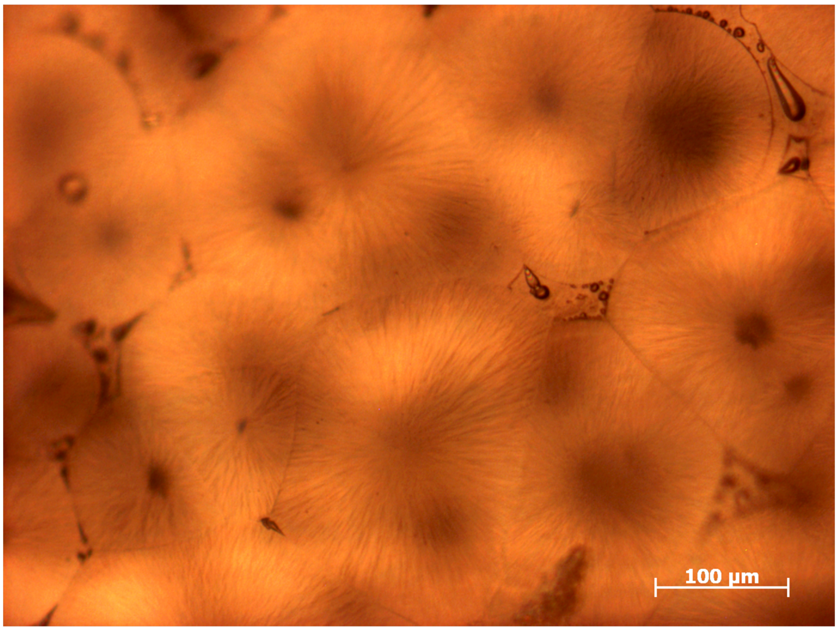

Figure 2.3.: *Light microscopy image revealing spherulite formation of PEO even via rapid cooling preparation.*

2.1.5. Ethylene Vinyl Acetate

To complete the range of polymers with a melting point between 160°C and 65°C ethylene vinyl acetate (**EVA**), see Figure 2.4, was used. As it is a copolymer consisting of ethylene and vinyl acetate (**VA**), a variation of the percentage of VA can be used to vary the melting point. Two different species are used, one with 9.3 % and one with 25 % VA, resulting in melting points of 100°C and 78°C respectively, which can be seen in the STA curves in Figure 2.4.This also shows the volatizing threshold of 421°C and 429°C respectively.

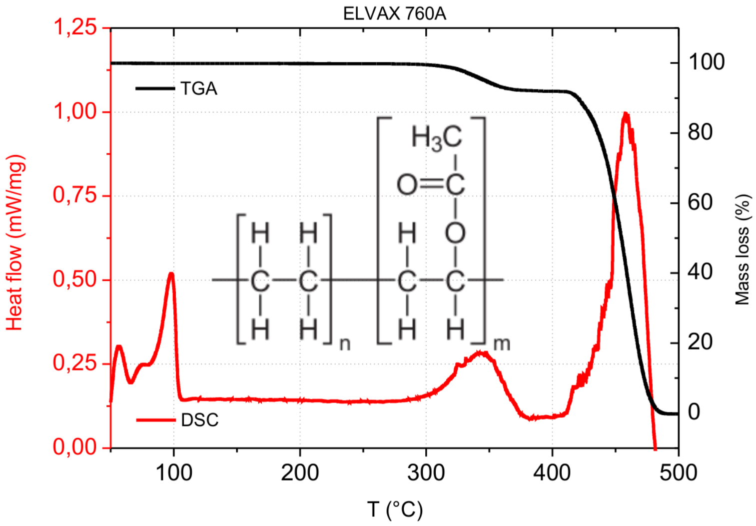

Figure 2.4.: *Chemical formula of ethylene vinyl acetate together with combined DSC (red) / TGA (black) characterization.*

As the EVA with a lower VA percentage consists of a high fraction of ethylene, its properties are very similar to those of LDPE. By increasing this VA portion, it becomes more and more amorphous and the properties change to those of thermoplastic rubbers.

When exposed to radiation, EVA will first decompose to an acetic acid which is produced during a cross-linking mechanism that starts at approximately 300°C and is based on ester pyrolysis. There is a loss of mass during the heating, which is due to the formation of acetic acid. Thus, the material with a higher portion of VA has a higher loss of mass. The second step is a scissioning of the polymer chains. The idea behind this polymer was to investigate a polymer having both scission and cross-linking at the same time.

2.1.6. Polystyrene

The last polymer sample used was polystyrene (PS), see Figure 2.5. It was chosen because it has been well investigated in TEM via EELS showing a very distinct plasmon peak at 6 eV allowing damage tracking via TEM. Thus, it was mainly used as a control sample for the application of TEM lamella preparation. It is a synthetic aromatic polymer made from the monomer styrene and can be made rigid or foamed. As it is chemically very inert, it is resistant to many acids and bases, but can be easily dissolved by many chlorinated solvents or many aromatic hydrocarbon solvents.

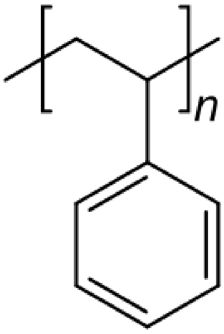

Figure 2.5.: *Chemical formula of polystyrene.*

As with most polymers used in this thesis, PS also suffers during e-beam exposure. Therefore, for TEM lamella preparation a 80 nm thick Pt/Pd top layer was sputtered onto the sample to prevent any damage during initial SEM inspection. Furthermore, such layers tend to induce curtaining effects during conventional TEM lamella thinning. Hence, to prevent this effect, upside-down thinning was performed for these samples with a minimum of e-beam exposure during the thinning process.

2.2. Damage Characterization in Standard Patterning

2.2.1. Morphological Instabilities

As a starting point, individual effects are representatively discussed for polypropylene. For demonstrating morphological issues, $2 \times 2\,\mu\text{m}^2$ box patterns were fabricated using standard serpentine patterning strategies at 30 kV, 500 pA and 50 pA. The high current was used due to practical reasons as such currents allow rapid processing. At the same time, it is very complicated to process polymers with this current, but degrading effects were demonstrated very clearly. The two main parameters which were varied in this patterning strategy are the dwell time (**DT**) and the point pitch (**PoP**). To give a first representative insight, the three different types of polypropylene were used which differ in their molecular weight, melting point and volatizing threshold while the chemistry remains the same. This first study comprises DT and PoP variation at room and cryogenic temperatures an will finally demonstrate that even the lowest sample temperatures can not prevent local damage.

2.2.1.1. Redeposition Influences

As the removal rate will be used as the key quantity for the following discussion, redeposition effects have been characterized first to exclude a respective convolution. For this purpose, milling depths and side wall angles are first investigated via SEM and AFM in the relevant dose range. As Figure 2.6 shows, the milled depths (red circles) and side wall angles with respect to the surface normal (blue triangles) behave predominantly linearly which confirms weak redeposition contributions. If milling depths show a decreasing behavior for higher doses, redeposition effects start to dominate as the milled material is not able to escape from the relevant trenches. The second indication for not being dominated by redeposition effects is the side wall angle which shows a tendency towards higher angles with respect to the surface normal for the dose range used. This behavior suggests that redeposition effects are present, but are of minor relevance to the geometries used with a final aspect ratio of less than 0.5.

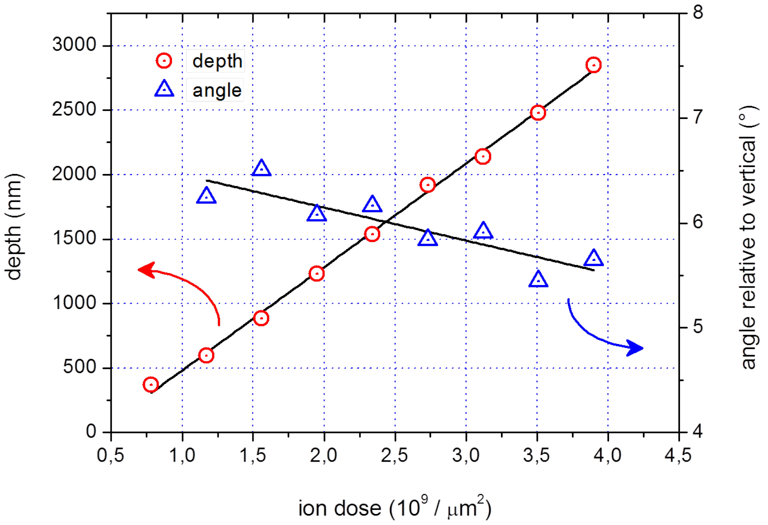

Figure 2.6.: *Milling depths (circles, left axis) and side wall angles (triangles, right axis) as a function of total ion doses on PP fabricated via standard patterning strategies.*

2.2.1.2. Removal Rate Experiments at Room and Cryogenic Temperatures

For these experiments, the removal rate is characterized via measuring the structure depths for DTs between 5 µs and 2000 µs at 20 nm PoP (default values), 30 kV and 500 pA. To provide comparability, identical footprints have been used, which required an adaption of patterning loops for varying DTs to maintain the total dose. The DT dependent removal rates for all PP types are shown in Figure 2.7 (left inset) and show very similar values of about $50 \pm 5\,\mathrm{nms}^{-1}$ for small DTs up to about $200\,\mu$s. Subsequently, a severe removal rate increase by a factor of 7 can be observed which always show a fast increase followed by a more linear region. The important detail, however, is the scaling with the molecular weight: the shortest PP materials (blue) increase the fastest while longest polymers (black) clearly show delayed tendencies. When plotting the removal rates at $660\,\mu$s (increasing part) and $1000\,\mu$s (linear part) versus the molecular weight, one obtains a linear scaling as shown in Figure 2.7 (right inset). This effect clearly shows the different temperature ranges: first, the local heating is clearly below the volatizing threshold which is reflected in the stable removal rate. When the beam pulses increased, local temperatures also increased above the volatizing threshold which led to thermally assisted material evaporation in the proximity of the ion beam. This process then led to a steady state situation given by the thermodynamic properties towards proximal evaporation regions indicated by the more linear tendency for long DTs. This is also consistent with the scaling for the different polymer lengths as shortest chains reach their volatizing length sooner than long polymer chains, which explains the delayed and linearly scaling shown in Figure 2.7.

The most intuitive approach for reducing this effect would be lowering the material temperature down to cryogenic temperatures. For that we designed and fabricated a variable temperature stage allowing stable cryo-temperatures (CT) down to - 150°C. To further support the cooling we used very thin PP slices to further reduce the volume which has to be cooled. A direct comparison of the DT behavior is shown in Figure 2.8 for RT and CT by red squares and blue triangles, respectively. As can be seen even at - 150°C, the same removal rate increase as for RTs can be observed, however, with a delayed character ($\approx 200\,\mu$s). For the highest DTs the CT removal rates again converge to the room temperature data. This effect indicates that lowering the temperature can delay but not prevent the material from volatizing. The reason for this behavior can be found in the low thermal conductivity which is unable to transfer the introduced heat on the given time scales. To investigate the current dependency, Figure 2.8 also shows the removal rate for 50 pA beam currents (black circles, right axis) with same settings. As can be seen, the absolute removal rates are about one order of magnitude lower, however, the same tendency is revealed. This again supports the calculations in section 2.3 and proves local ion-material processes to be the dominating factor which, together with the low thermal conductivities of polymers, led to massive heating.

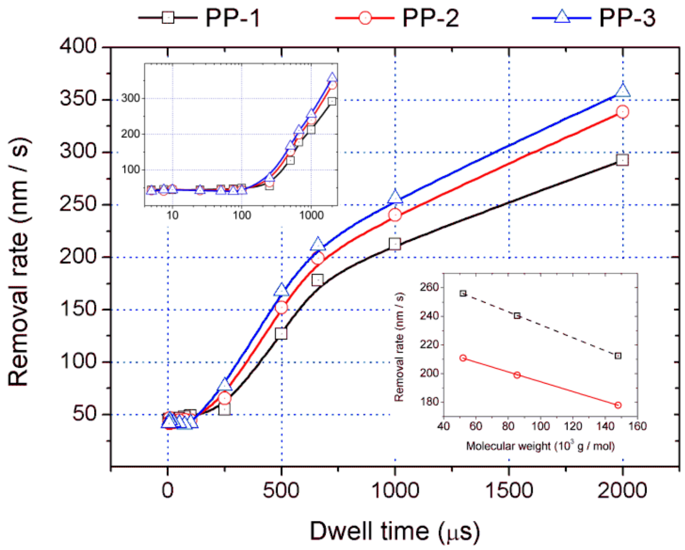

Figure 2.7.: *Removal rate vs. beam dwell time for 500 pA regular patterning at room temperature for the three different PP types (see legend and details in section 2.1.1). The top left inset gives a logarithmically scaled version of the main graph revealing the very constant removal rates up to about 200 μs. The bottom right inset gives removal rates at a 660 μs (red) and a 1000 μs (black) dwell time as a function of molecular weight.*

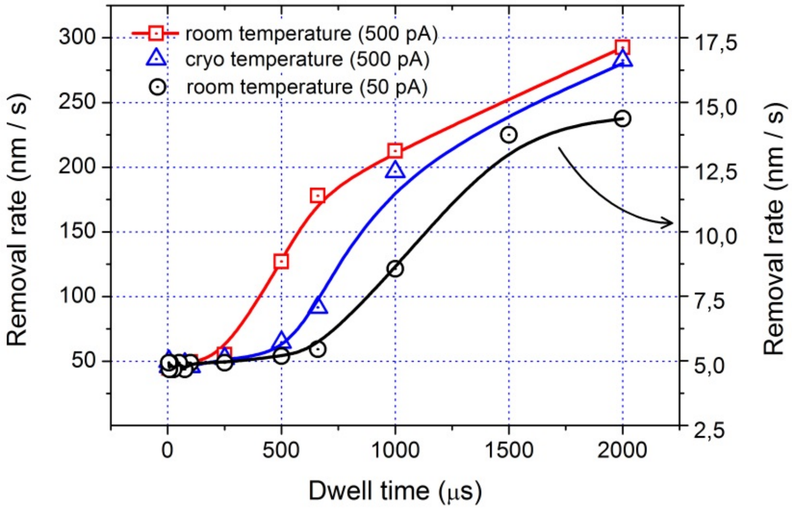

Figure 2.8.: *Removal rate in dependence on pixel dwell times for room temperature (red squares) and cryogenic temperatures (blue triangles) fabricated at 30 keV and 500 pA via standard patterning strategies. The black circles show the same experiment with much lower beam currents of 50 pA (right Y axis).*

The point pitch as the second, very important parameter was also varied at room and cryogenic temperatures from 10 nm up to 150 nm at DTs of 5 μs, 50 μs and 500 μs as summarized in Figure 2.9. As can be seen forthe lowest DTs (bottom panel) the removal rate remains almost constant at 50 ± 5 nms^{-1} for room (black) and cryogenic temperature experiments (blue). By increasing the DTs, one can see that the onset for high PoPs remains constant at approximately this value, whereas for lower DT, below 30 nm and 50 nm for 50 s and 500 μs, respectively, the removal rate is dramatically increased for both RT and CT conditions. As can clearly be seen, they only differ in the amount of increase which is higher for RT conditions than expected. Beside this removal rate modification, the surface roughness is also affected by a PoP variation. As one can clearly see in the AFM height images in Figure 2.9, a PoP increase from the default value of 20 nm up to 150 nm reveals a roughness increase from 0.2 nm to 2.9 nm, which affects the structure obtained negatively.

The results have to be seen in the context of the calculations in section 2.3. Increasing PoPs means that subsequent patterning points start at lower temperatures which effectively reduces the heat accumulation. Thereby the local temperature regimes can be kept below the volatizing threshold reflected by low removal rates. The comparison between RT and CT again demonstrates that local thermodynamic circumstances are predominantly responsible for the final effects while the absolute sample temperature can only delay but never prevent massive heating beyond the volatizing threshold!

2.2.1.3. Polymer Data Comparison

Based on the detailed investigation for PP, we now compare the findings to different polymers as described in section 2.1 to exclude the possibility that the PP findings are material-specific. A summary of all DT and PoP variation experiments for different polymers is shown in Figure 2.10. As is immediately evident, all materials show the same overall tendencies, which proves the discussed behavior to be a general effect during FIB processing of polymers.

Despite the similarity, a close look reveals material-related differences. First, the removal rate increase varies together with the absolute values of base and maximum levels (see Figure 2.10). The strongest exception is PEG, which also shows the lowest melting and volatizing threshold. Following closely, we can find PMMA, which is known to be a very effective scission material. This behavior is not unexpected but ideally fits into the picture of high removal rates for lower melting / volatizing polymers. The PoP variation

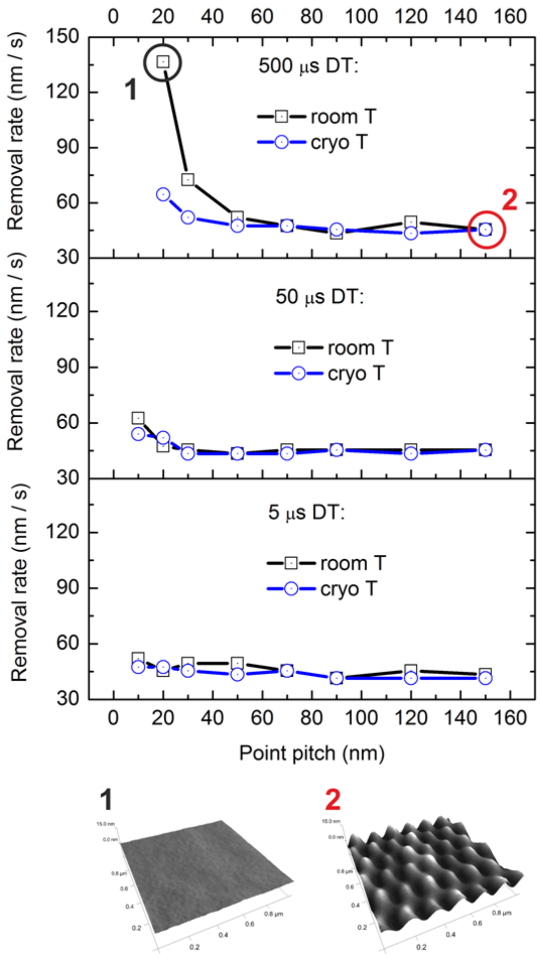

Figure 2.9.: *Removal rates as a function of PoP distances for 500 s (top panel), 50 s (center panel) and 5 s (bottom panel), dwell time at room- (black squares) and cryo-temperatures (blue circles). The green stars gives a preview of interlacing removal rates at room temperatures as will be discussed later. The bottom row gives AFM images of 1x1 µm bottom areas of FIB structured PP according to the indication in the top panel. RMS roughness analysis revealed 0.2 nm (1) and 2.9 nm (2).*

for 5 µs, 50 µs and 500 µs also reveasl the same behavior as observed for PP (compare Figure 2.10 with Figure 2.9). As the DT variation reveals, the absolute values of the removal rate are highest for PEO followed by PMMA while remaining approximately constant for all the other polymers. For low DTs the removal rate is constant for all polymers individually and this onset is observed at the higher DTs at high point pitches. For 50 and 500 µs DTs the low PoP patterning shows an increased removal rate below 30 nm and 50 nm, respectively, which is also in very good agreement with the observations

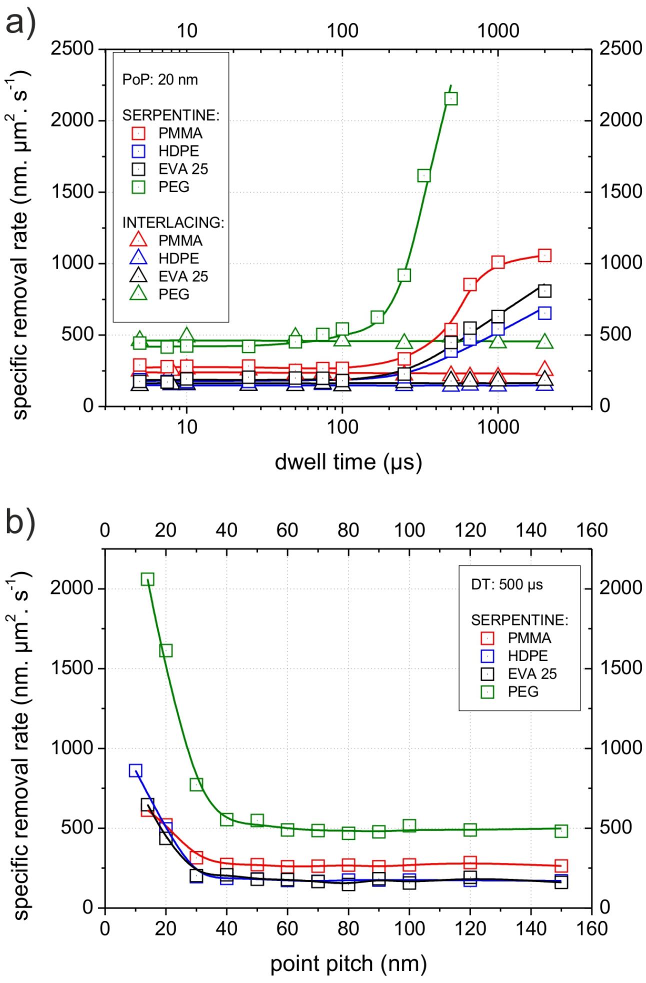

Figure 2.10.: *Comparison of dwell time (a) and point pitch (b) dependency of the removal rate for PMMA, HDPE, EVA and PEO, revealing the same tendency as shown for PP.*

on PP. Here it must be noted that the removal rate increase at 50 μs is very weak for most of the polymers, except for PEO.

This allows the conclusion that the observed behavior and the explanation given are observable for a wide range of polymers and are thus attributable to an intrinsic effect during FIB processing of polymers with low thermal conductivities. However, so far, only morphological aspects have been investigated. Therefore, the study is expanded to include chemical studies in the following to gain a much more comprehensive insight. A detailed discussion of material-related effects can be found in reference [32].

2.2.2. Chemical Degradation

Investigations of the chemical degradation are performed via Raman spectroscopy (RS) for different preparation parameters, patterning strategies and sample temperatures, since all of the polymers used clearly show assignable Raman signatures. In more detail, RS intensities of CH_2 and CH_3 stretching vibration bands between 2700 cm^{-1} and 3000 cm^{-1} are integrated as a quantitative measure for the chemical polymer degradation in dependence on different FIB process parameters.The same structures with a 2x×2 μm^2 footprint were patterned for these measurements as RS allows focusing diameters of approximately 400 nm. Figure 2.11 summarizes the results for RT (red) and CT (blue) conditions in dependence on the DTs for PP samples using standard patterning strategies. First, the massive degradation for increasing DTs is evident, resulting in complete chemical degradation for DTs in the ms range, which is in agreement with the removal rate results shown in section 2.2.1. The difference between CT and RT is very small for shortest and longest DTs while the central region around 500 μs shows stronger deviation. Comparing these findings with the removal rate experiments in Figure 2.8, it becomes evident that the observed behavior exactly describes the situation where CT conditions delay but cannot prevent the destruction of the chemical structure.

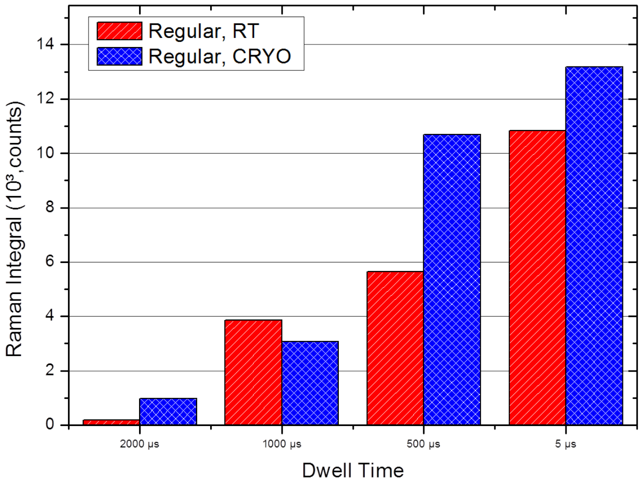

Figure 2.11.: *Raman summary for room (red) and cryogenic temperature (blue) experiments on PP performed at 30 kV, 500 pA, 20 nm PoP and varying DTs via standard patterning strategies. The higher the bars the more intact is the resulting polymer area.*

In Figure 2.12, the Raman intensities of the investigated region are shown for the polymers used for the room temperature experiments. In principle, these reveal trends similar to the PP measurement and in particular to the removal rate findings summarized in Figure 2.10. The main difference between the polymers again is the onset of chemical degradation, where the decrease of Raman intensities becomes significant.

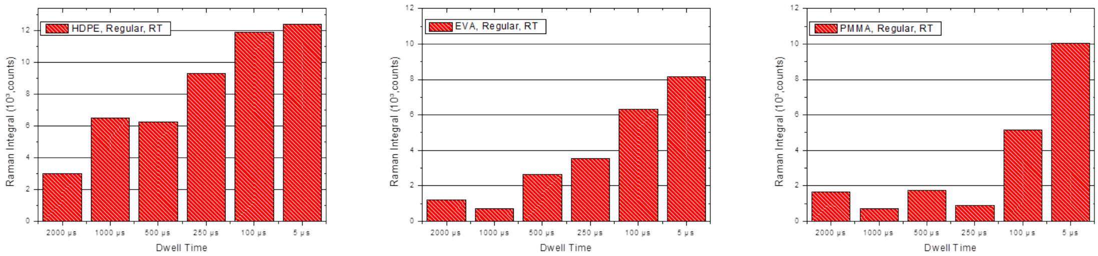

Figure 2.12.: *Raman integral summary for HDPE, EVA and PMMA for the room temperature experiments.*

The essence of this section, however, is the result that chemical degradation goes along with increasing removal rates as described in section 2.2.1. This is completely consistent with the interpretation based on the volatizing threshold which will be further discussed in sections 2.3 and 2.3.3.

2.2.3. Cross-Section Characterization

2.2.3.1. Ultramicrotomy Cuts

To investigate cross-sections of differently patterned areas, ultramicrotomy preparation was used. For this purpose, $10{\times}2\,\mu m^2$ footprints were structured in PP using different FIB parameters and these were subsequently embedded in epoxy (EPOFIX). To find minimum cross influences from the embedding and ultramicrotomy preparation, different procedures were tested as described in section 1.5. Related cross-sections were then investigated via AFM and KPFM to obtain a comprehensive insight concerning unwanted preparation artifacts as well as details on the damaged polymer areas.

First of all, embedding in EPON and SPURR followed by an RT ultramicotomy with oscillating diamond knives reveals two different effects as shown in Figure 2.13 left and center, respectively. EPON-based processing reveals a peak ≈ 50 nm high at the interface which is about 500 nm wide as can be seen by the correlated AFM height cross sections

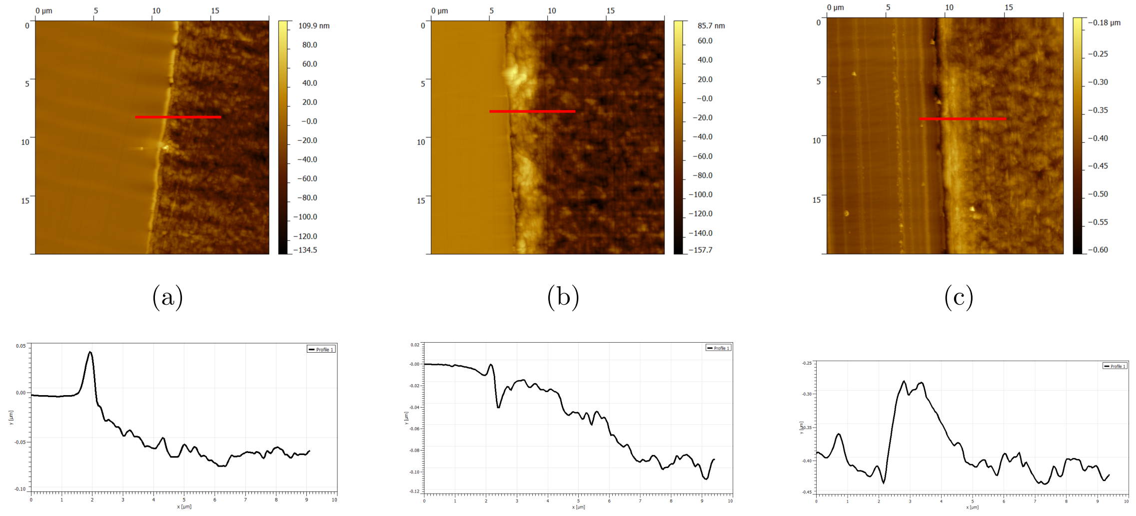

(a) (b) (c)

(d) (e) (f)

Figure 2.13.: *AFM height images (top row) of ultramicrotomy related PP cross-sections with the PP areas on the right side for different epoxy types: EPON (left), SPURR (center), and SPURR at -120°C (right). The bottom row gives the height cross-sectional profiles along the red lines in the AFM height images.*

in Figure 2.13 (bottom row). As the depth damage in the polymer is expected to be clearly less than 500 nm, which follows from the calculation in section 2.3, the peak which appears prevents high resolution analyses via AFM phase and/or KPFM. Therefore, SPURR procedures were investigated which revealed the opposite effect of a 60 nm deep trench with a width of almost 1 μm (see cross sections in Figure 2.13). The underlying effect might be the difference in the Youngs modulus together with shear forces during ultramicrotomy cutting. Therefore, we changed the preparation temperature for SPURR embedding to - 120°C while cutting as can be seen at the right side of Figure 2.13. Unfortunately, severe preparation artefacts such as scratches but also unwanted peaks at the interface areas appeared which again prevents reliable AFM-based analysis. Finally, we specifically changed the embedding material towards SPECIFIX as it polymerizes at low temperatures. With this material, different parameters were tested including cooling down to - 120°C together with an oscillating knife. With this set of parameters for the cutting process, structures with a footprint of $10 \times 2\,\mu\text{m}^2$ were cut for the investigation in AFM via KPFM. Although this method provided acceptable cross-sectional profiles, another problem occurred by means of redeposition influences which finally prevented a clear assignment of damaged polymer zones at the bottom areas of FIB structured samples. Therefore, ultramicrotomy based cross-sectional profiles are not an option to perform high-resolution KPFM and/or AFM phase investigations.

2.2.3.2. Polishing in Cross-Section Preparation

After the unsuccessful ultramicrotome attempts, careful polishing was tested as we consideedr KPFM to be the ideal method to achieve chemical variations with nanometer resolution. After optimizing the polishing procedure, AFM investigations revealed interface structures that are too high as can be seen in the AFM images and cross-sectional profile in Figure 2.14. Therefore, in spite of great efforts and a large number of samples that were investigated, ultramicrotomy and careful polishing were not able to provide sufficiently smooth and compact interfaces for AFM-based high-resolution imaging to obtain cross-sectional information from FIB processed bottom areas.

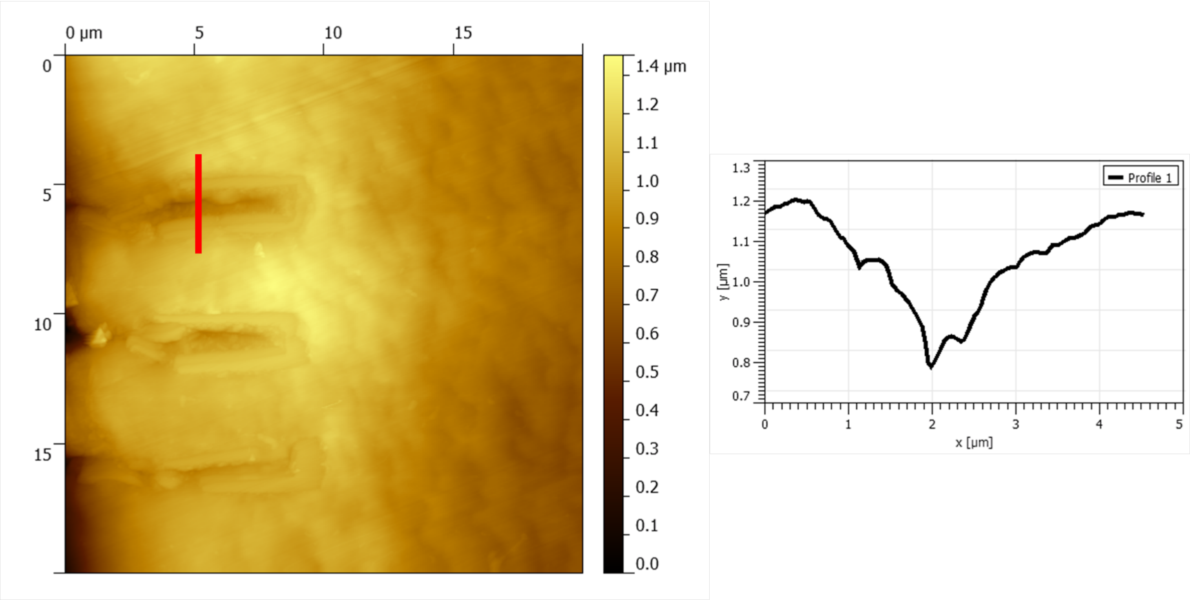

Figure 2.14.: *AFM height image (left) of a polished cross-section showing severe height variation by a line cross section (right) at the region of interest (marked red) making it incompatible with KPFM.*

2.3. Simulations

2.3.1. Finite Elements Simulations

The first approach using the finite element method (**FEM**) was used for calculating the temperature evolution during the ion beam processing of soft matter via the simulation software ANSYS V13. Due to the enormous computing power required, the temperature was initially estimated following the theoretical approach by Volkert et al. [49] with the steady-state temperature

$$T(t) = \frac{P}{\pi \alpha \kappa} \tag{2.1}$$

where α is the FWHM of the circular ion beam, which is supposed to be 39 nm as the manufacturer specifies, P as the beam power and κ is the thermal conductivity of the sample. With this approach, one is able to estimate a maximum temperature, but without considering spatial distribution and / or temporal evolution. Computing this temperature for the polymers used we get values for the maximum temperature as listed in Table 2.1.

Table 2.1.: *Calculated maximum temperatures for the polymers based on Equation 2.1.*

Material	**Temperature** [°C]
PP	1113
HDPE	499
PMMA	1288
PS	3060

The FEM simulations were started with a heating of a hemispherical volume 39 nm in diameter for the corresponding dwell time of 500 μs and subsequent cooling for 1 μs. Using this simulation for PP, we get a temporal and spatial temperature evolution as shown in Figure 2.15 (a). This plot reveals a spatially very confined area of sample heating, but at a distance of 20 nm (vertical axis) from the hemispherical center, the temperature rise is approximately 75 % of the maximum temperature. Even at a 100 nm distance, the temperature shows a value of approximately 15 % from the maximum value. With this temperature distribution, an upper estimation of proximal heating can be done when neglecting dynamic cooling processes. Note, the latter assumption in a first step was unfortunately limited by a lack of computing power. Assuming now that subsequent patterning points start at already elevated temperatures, one can estimate the expected temperature accumulation as shown in Figure 2.15 (b) along the scan direction for different point pitches between 10 nm and 500 nm. As can be seen, technically-induced heating by a factor of 20 is the consequence for the most critical point pitch of 10 nm. Of more relevance, even for 20 nm and 50 nm, equivalent to 50 % and 125 % beam overlap respectively, the process induces a temperature increase of a factor 6 and 8, respectively. This estimation immediately provides the justification for the interlacing strategy, which will reduce this process-induced heating effect by expanding the point pitch of consecutive points towards a distance where proximity heating is practically negligible. Furthermore, individual patterning points are allowed to cool down before neighboring pixel points are patterned, which depends on the lateral dimensions of the patterning footprint as well on the dwell times used. In Figure 2.15 (c), the maximum temperature rise is plotted for the calculated point pitch, revealing that for a 100 nm point pitch the increased temperature is far below that of the default point pitch of 20 nm. However, as expected and confirmed by experimental results, a simple expansion of the point pitch is not a satisfactory solution due to roughness effects.

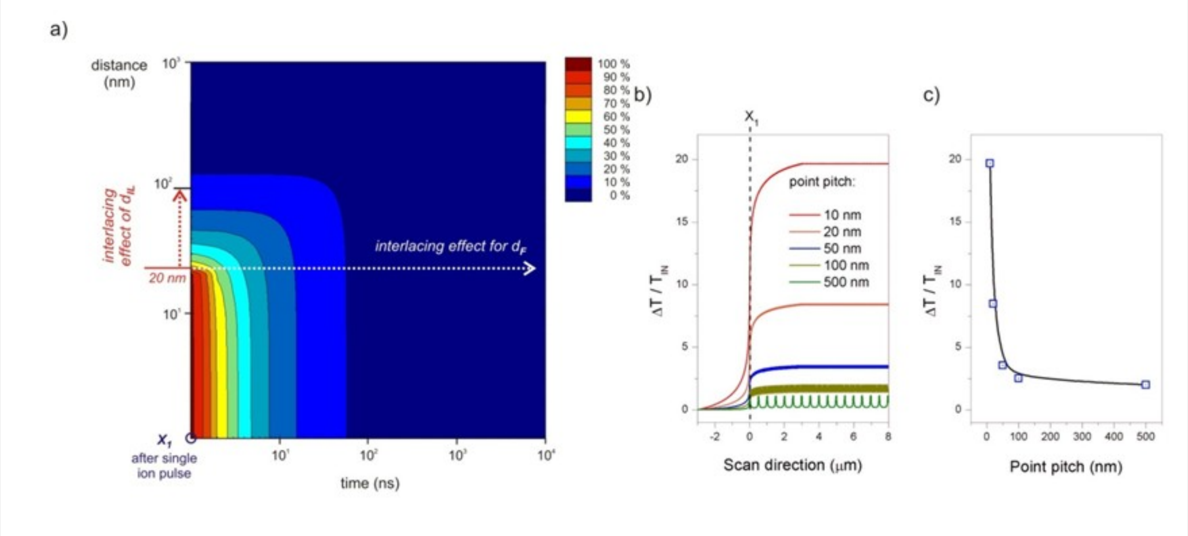

Figure 2.15.: *(a) Surface temperature FEM simulation as a function of time (horizontally) and the radial distance (vertically) after a single ion beam pulse. (b) Estimation of the technically-induced temperature increase during classical serpentine or raster-like scan. (c) Shows the saturated values of (b) in dependence on the point pitch allowing identification of minimum point pitches for reduced temperature accumulation.*

Furthermore, the thermal evolution inside a cylinder was implemented, which was used henceforward due to SRIM / TRIM simulations (see section 1.8.6) of the interaction volume revealing a more cylindrical interaction volume than hemispherical, by using a heat generation rate of $1.705\times10^{17}\,\mathrm{W/m^3}$, calculated from the beam power at $1.5\times10^{-5}\,\mathrm{W}$ and the cylinder volume of $8.79\times10^{-23}\,\mathrm{m^3}$. With this refinement, a 9-point classical strategy was simulated by straightforward calculation of the temperature evolution of these 9 points with heat dissipation and thermal decay revealing a temperature rise of approximately 2.5 % for the last point, which can be seen in Figure 2.16. This is a very weak percentage temperature increase compared with previous simulations. This approach has the lack of not considering the real interaction volume of the impinging ion beam and thus the heating process cannot be simulated properly with acceptable simulation duration. Thus another approach based on the thermal spike model was used, which will be explained in the following sections.

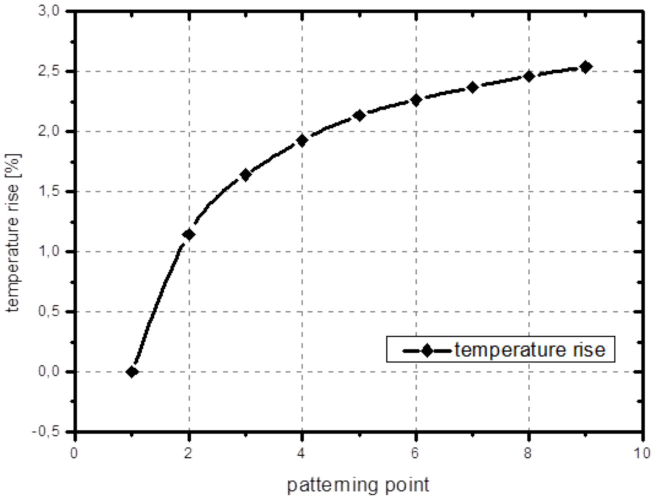

Figure 2.16.: *FEM simulated temperature increase for the first 9 ion beam points of patterning with a point pitch of 20 nm revealing a temperature increase of 2.5 % and a clear saturation behavior.*

2.3.2. Interaction Volume and Phonon Distribution Simulation

As mentioned before, the FEM simulation is not able to describe the temperature accumulation. Hence, the thermal spike model was considered to be an appropriate workaround. However, before the thermal spike model can be applied the interaction volume needs to be simulated as an input parameter. This can be done using the SRIM / TRIM software package which is considered to be the golden standard [54]. This simulation allows simulation of the interaction volume including energy losses and related phonon distribution which are used as input parameters for the thermal spike model calculations.

Table 2.2.: *Simulated radial diameter and longitudinal distance (FWHM) of the interaction volume for the materials used.*

Material	**Radial diameter** [Å]	**Longitudinal distance** [Å]
Si	536	279
PP	534	490
HDPE	532	474
PMMA	548	511

As a starting point, the interaction volumes of normally impinging 30 kV Ga$^+$ ions with a Gaussian cross section profile and a half max diameter (FWHM) of 40 nm, according to the ion beam diameter of 500 pA for the NOVA 200 DBM used, were simulated for the polymers PP, HDPE and PMMA that were used. These materials were chosen as they suffer severely understandard FIB processing strategies and are representative. Furthermore, these polymers basically exhibit very different chemical processes during heating which ultimately allows assignment of individual effects as discussed later [32, 40].

Simulations were performed with 10,000 ions and a voxel size of 1.5 Å.Si was used as a reference material, due to its uncomplicated and easy implementation in FIB processes. Figure 2.17 gives an in-scale comparison of the simulated interaction volumes revealing a similar lateral expansion of approximately 540 Å. However, the depth distribution in Si has been found to be in the range of about 280 Å while for polymers, this value is almost doubled (500 Å), as is summarized in more detail by Table 2.2. This difference in the longitudinal distance of the ion traces is a consequence of the lower stopping power of polymeric materials as compared to Si, allowing the ions to travel further before scattering events [54].

The second aspect which must be considered before entering the thermal spike model concerns the energy dissipation mechanism, as shown in Figure 2.17 (c) and as summarized in Table 2.3. Based on the SRIM simulations for Si and the three polymers, it can be seen that the highest energy losses of 45-55 % are correlated to recoils related phonons generated by atoms which leave their original positions temporarily due to inelastic

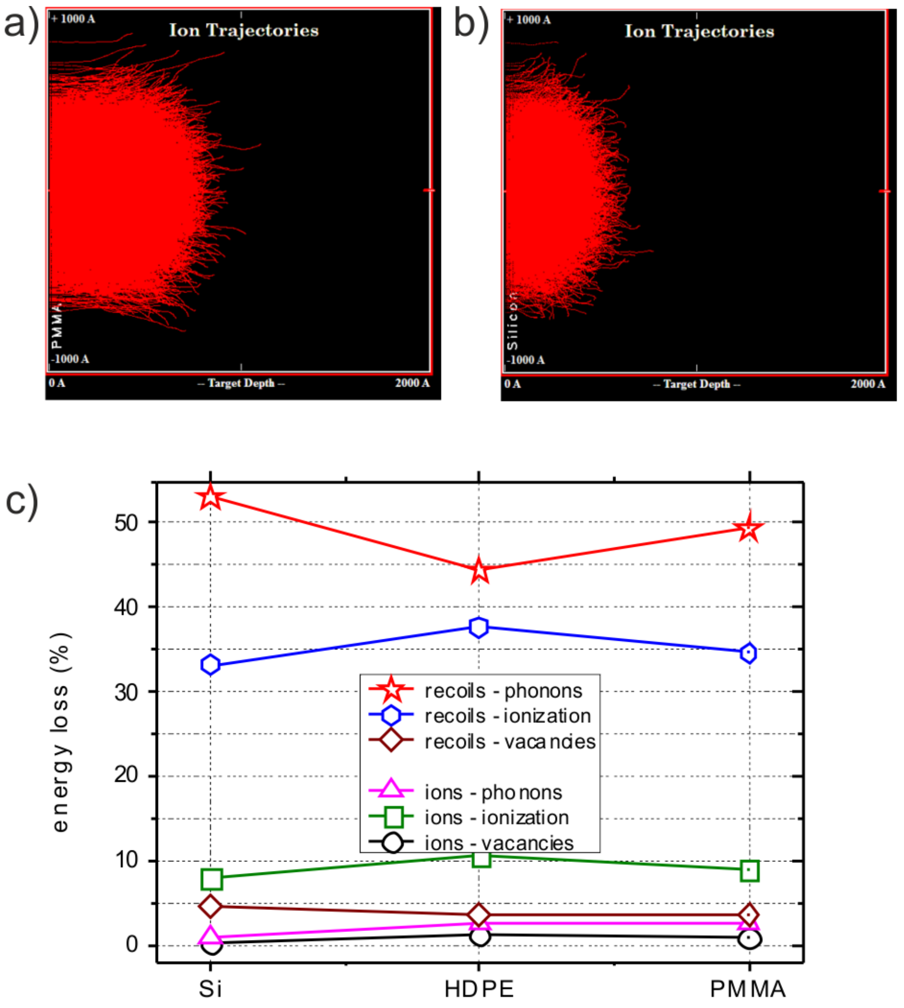

Figure 2.17.: *Ion related Interaction volumes of normally impinging 30 kV Ga$^+$ ions in PMMA (a) and Si (b). All simulations used 10,000 ions with a Gaussian beam profile with a FWHM of 40 nm. (c) shows the relative percentages of the individual dissipation mechanism for different materials.*

scattering. By their returning to their primary positions their energy is transferred to the oscillations of the polymer backbone, which we call phonons due to the similarity to phonons in crystallographic materials. The second highest energy loss mechanism is related to recoil ionization at about 30-40 % which has a minor influence on temperature effects studied in this work. This is due to the energy transfer which is higher than the displacement energy and thus there is no transfer to phonons and meaning it is not coupled with thermal excitations. Other effects such as primary ionization or vacancy generation are found to be of minor importance with less than 10 % of the energy dissipated. As

Table 2.3.: *Different energy dissipation processes and their percentage for the four different materials.*

Material	**Recoils phonons** [%]	**Recoils ionization** [%]	**Recoils vacancies** [%]	**Ions phonons** [%]	**Ions ionization** [%]	**Ions vacancies** [%]
Si	53	33	8	5	1	0
PP	45	38	11	4	3	1
HDPE	44	38	11	4	3	1
PMMA	49	35	9	4	3	1

can be seen in Table 2.3, Si has the highest energy loss due to recoils related phonons amounting to 53 % while the polymeric samples show higher recoil ionization effects compared to Si.

Due to the dominating energy loss for recoil related phonons, this distribution is of particular importance for the thermal spike model as energy loss input. Figure 2.18 shows the ion interaction volumes for Si (top), HDPE (center) and PMMA (bottom) together with the related phonon distribution along Z with the beam in the center (Y = 0) and reveals clearly smaller spatial and energetic distribution expansions for all polymers. In contrast, Si shows an approximately halved range along Z but with an almost doubled energy loss per Å as the total incoming energy is the same for the polymeric samples. Typical values for the polymers are around 1.3-1.5 eV/Å per ion while for Si there is an area with values up to 2.8 eV/Å per ion.

The spatially resolved phonon distribution obtained from these considerations is now used as input data for the energy loss distribution $\Delta E_p(r)$ per Å in the cylindrical thermal spike model.

2.3.3. Thermal Spike Model Calculation and Experimental Validation

With the phonon distribution as an energy loss input parameter, the cylindrical thermal spike model according to Equation 2.2 can be used for the calculation of the spatial and temporal temperature distribution and evolution, respectively. This model assumes that the energy transfer occurs immediately for phonon generation within a zero-sized region.

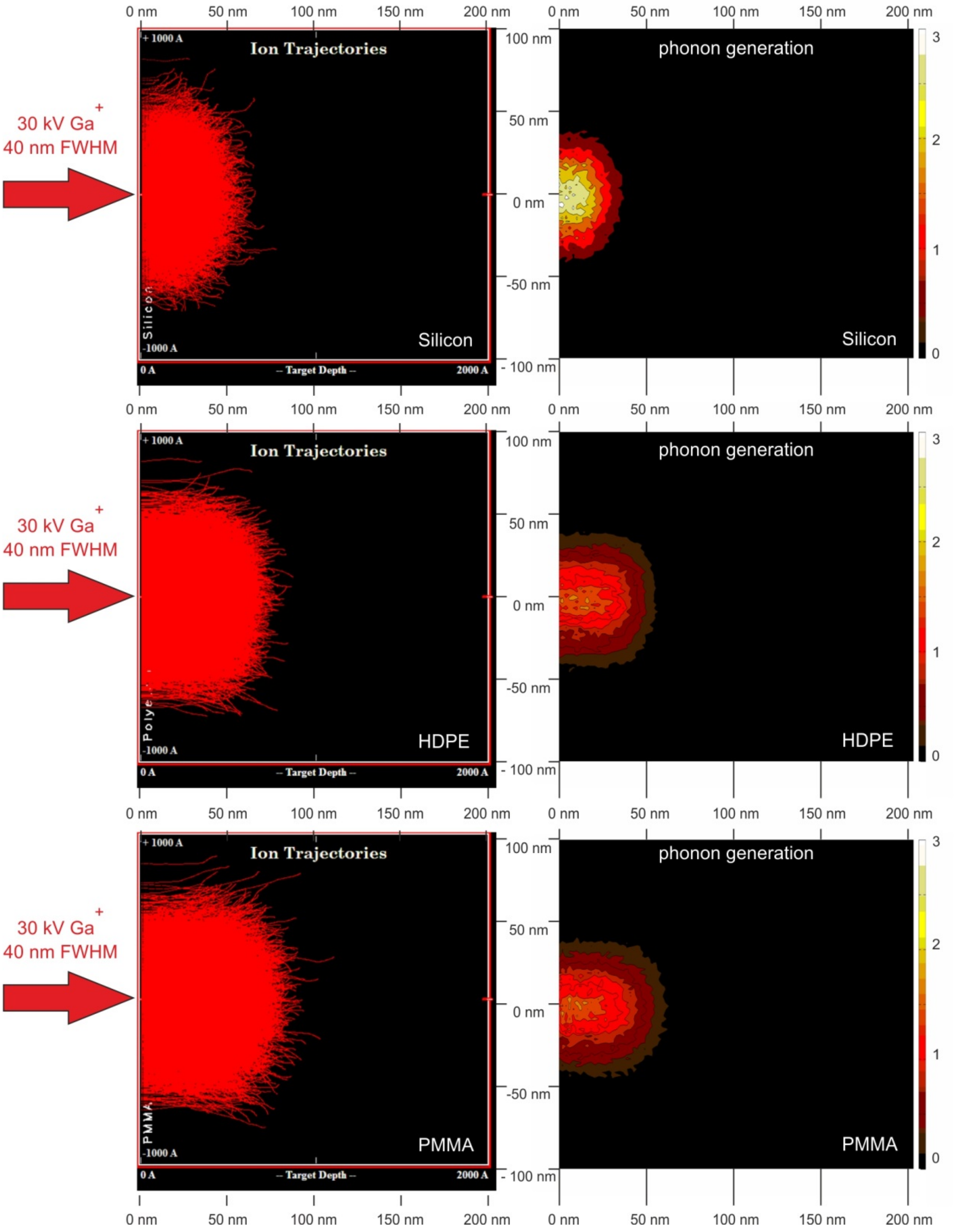

Figure 2.18.: *Simulated phonon distribution for HDPE (top left), PP (top right), PMMA (bottom left) and Si (bottom right).*

All calculations were performed via MATLAB in a 2-dimensional radius / depth plane with a time resolution of 0.2 ps.

$$T(r,t) = T_0 + \frac{\Delta E_p(r)}{4\pi\kappa t} exp\left\{\frac{-c_p r^2}{4\kappa t}\right\} \tag{2.2}$$

Further assumptions made in this model are i) steady state conditions which means that deposited energies are distributed among the atoms in the collision cascade such that a local transient thermal equilibrium is reached and a temperature can clearly be assigned; ii) the thermal spike occurs within 0.2 ps of each ion strike; iii) heat convection and heat radiation are not included; and iv) an isotropic thermal conductivity is assumed. A severe disadvantage of this model is the ignoring of material removal through sputtering and/or the evaporation induced through thermal increase. Appropriate workarounds, however, are discussed later in the thesis.

Table 2.4.: *Thermal conductivities and volumetric heat capacities of the different materials as subsequently used for thermal spike calculations.*

Material	**Thermal conductivity** [W/m]	**Volumetric heat capacity** [J/cm^{3}K]	**Maximum temperature** [°C]
Si	149	1.64	90
PP	0.22	2.09	4633
HDPE	0.49	2.09	2111
PMMA	0.19	1.74	5945

By using Equation 2.2 together with the spatial phonon distributions, a laterally and temporally resolved temperature distribution on the surface is calculated for Si, HDPE and PMMA, which can be seen in Figure 2.19. This calculation reveals a maximum surface temperature for Si of less than 100°C (see Table 2.4) in agreement with the literature [49]. Considering the high melting point for Si, this nicely explains why this material can be processed via FIB without strong melting effects on the meso-scale. However, for polymeric samples, we calculated maximum surface temperatures up to 6000°C, which is only a hypothetical value due to the fact, that the thermal spike model ignores material evaporation and/or sputtering and will be discussed in the next paragraph. However, the main difference of the polymers compared to Si is the thermal conductivity which is 3 orders of magnitude lower, as can be seen in Table 2.4. Therefore, the generated heat in the material is not efficiently dissipated to surrounding regions in polymeric samples leading to a severe hypothetical temperature rise. As HDPE has the highest thermal conductivity of the investigated polymers the temperature rise is lowest as expected. For PP and PMMA, the thermal conductivities are very similar, therefore, the temperature differences in Table 2.4 are the consequence of the different heat capacities. As the phonon distribution is very similar for all three polymers, it can be concluded that the resulting difference is not due to the energy loss mechanism, but mainly to the strongly different, intrinsic material properties.

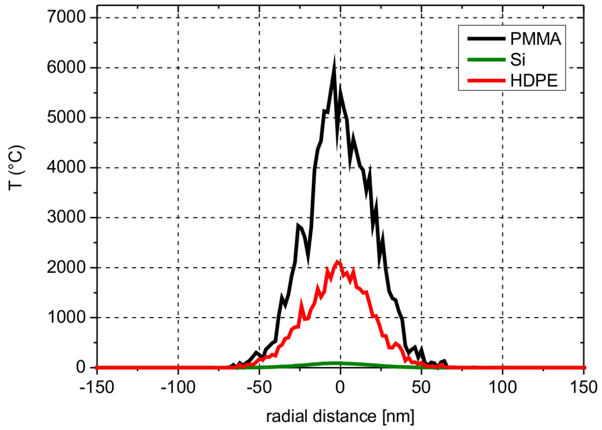

Figure 2.19.: *Calculated surface temperature distribution for Si, HDPE and PMMA based on the thermal spike model. Please note, these temperatures entirely ignore material removal via evaporation and/or sputtering. Hence, the results are hypothetical temperatures which serve as input information for further considerations.*

As described above, Figure 2.19 gives the hypothetical temperature ignoring material evaporation and/or sputtering. For polymers, it is logical that such high temperatures cannot be achieved as they by far exceed the evaporation temperatures. The latter are characterized in detail via combined differential scanning calorimetry (DSC) and thermogravimetric analysis (TGA) as shown in Figure 2.20 by red and black curves, respectively. This combined approach is also called simultaneous thermal analysis (STA) as used in the following. Based on these data and representatively shown in Figure 2.20, a classification into three regions is possible: 1) solid for temperatures below the melting point; 2) volatized for temperatures above the volatizing threshold where the chains are so short that they can directly leave the surface indicated by the start of mass loss; and 3) melt for temperatures between 1) and 2). The melt state must be further divided into liquid and modified depending on the polymer type used as discussed in detail in section 1.7. The latter fact was the reason for choosing the polymer types in this study as it allows detailed investigation of melt effects [32]. With this classification, three spatial

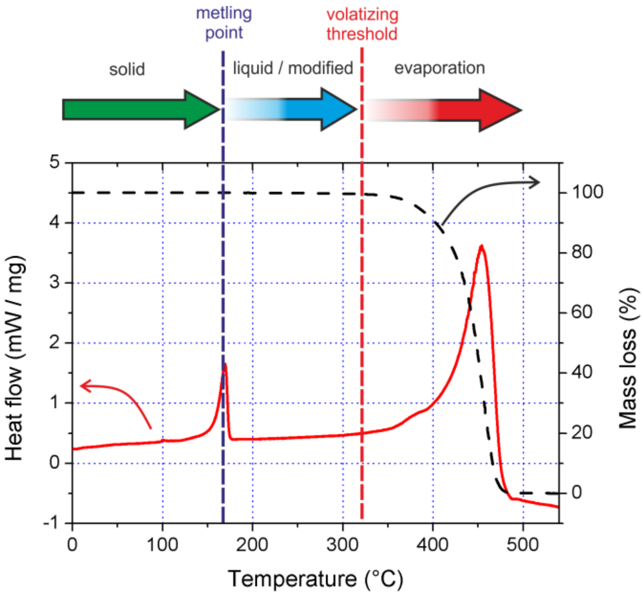

Figure 2.20.: *Representative STA analysis showing DSC (red) and TGA (black) behavior during heating. The first DSC peak indicates the melting temperature while the decaying TGA behavior for high temperatures indicates that the volatizing threshold has been exceeded. These two points allow classification of three different states during heating: solid, melt (liquid / modified) and evaporated (volatized) as used in the further course of this thesis.*

zones can be derived according to the different material states: solid (pristine), liquid / modified and volatized.

Table 2.5.: *Radial and depth values for volatized and modified regions for all polymers.*

	Volatized zone		**Modified zone**	
Material	**Radial range** [Å]	**Depth range** [Å]	**Radial range** [Å]	**Depth range** [Å]
PP	850	600	150	100
HDPE	800	550	150	100
PMMA	900	700	150	100

With this characterization, 2D cross sections along the Z-axis can be derived as representatively shown in Figure 2.21 for PMMA (a) and HDPE (b). According to the classification discussed above, the following color code has been adopted based on the STA characterization: green = solid (pristine), yellow = liquid / modified (material dependent), and red fully volatized. The corresponding lateral and depth dimensions are summarized in Table 2.5 to provide quantitative data.

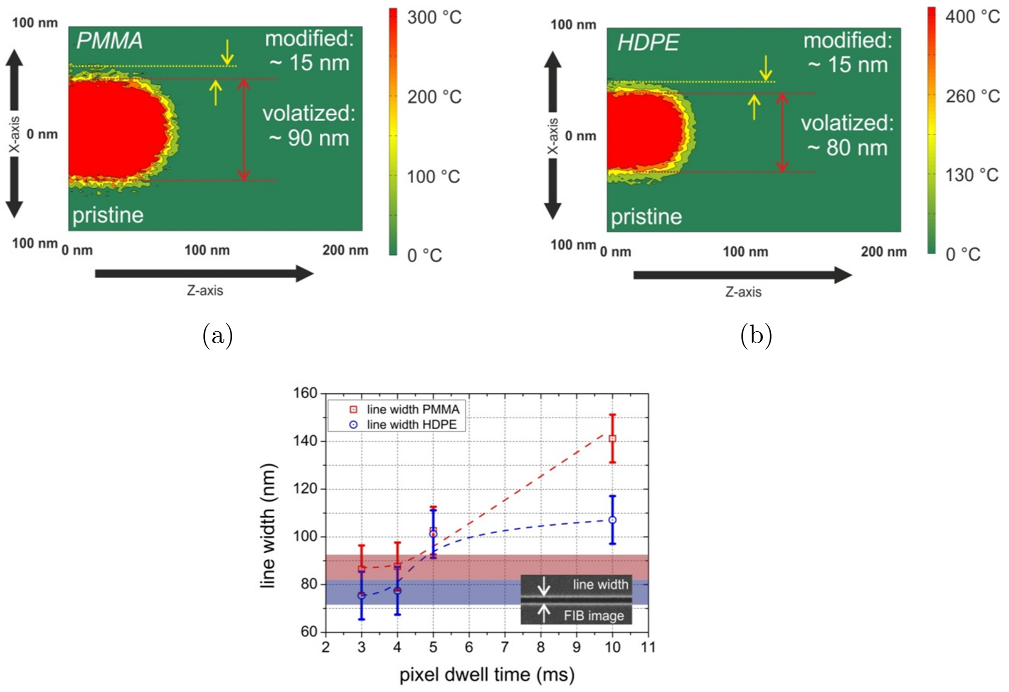

(a)

(b)

(c)

Figure 2.21.: *Calculated temperature distribution for PMMA (a) and HDPE (b) using the SRIM / thermal spike model approach. The different colors are adapted to the polymers where green means solid (pristine), yellow shows liquid / modified regions and red indicates entirely volatized areas. (c) shows experimental single line widths in dependence on pixel dwell times patterned in PMMA (red squares) and HDPE (blue circles) with regular patterning strategies revealing minimum line widths in the same range as predicted by the volatizing width for PMMA and HDPE, indicated by the red and blue bars, respectively. The inset gives a representative FIB image of shortest dwell times in PMMA.*

The crucial element which remains is to compare the widths for volatized regions from the calculations with real FIB experiments. Figure 2.21 shows the experimentally determined widths of single lines in PMMA (red) and HDPE (blue) in dependence on the pixel dwell time used. The latter must be investigated as this parameter leads to discontinuous lines for very short dwell times (not included in the graph) whereas increasing pixel dwell times lead to the expected line broadening due to longer single point exposure and the thermally assisted evaporation in the surrounding areas this entails. Hence, the values of the shortest dwell times (3 μs and 4 μs at a beam current of 500 pA at 30 kV) represent minimum line widths with continuous character. As can be seen in Figure 2.21, the values found experimentally are in very good agreement with the calculated predictions shown by the red and blue bars for PMMA and HDPE, respectively. This clearly proves the reliability of the calculations with respect to spatial temperature evolution and its consequences during FIB processing in polymers.

This model now can be expanded by means of a scanning patterning line allowing estimation of the relative temperature increase in dependence on process parameters. Figure 2.22a shows the heat calculated relative temperature increase for different point pitches between 20 nm and 100 nm using a regular single line patterning strategy. These calculations predict a gradual temperature increase by a factor of 2.6 for default point pitches of 20 nm, which is equal to a beam overlap of 50 % for the parameters of 30 kV and 500 pA used. As is evident, the calculations suggest an initial increase followed by a steady state condition at which the thermodynamic equilibrium between temperature generation and temperature dissipation due to energy loss and transfer to the surrounding areas respectively is established. By increasing the point pitch a situation is created where the consecutive patterning point starts at lower temperatures leading to lower heat accumulation and thus the additional heating is prevented for point pitches larger than 80 nm.

To cross check these predictions with real situations, Figure 2.22 also shows experimental single line data in PMMA as the most sensitive polymer. By patterning a single line with 20 nm point pitch (b) an initial width increase is observed followed by a constant line width which is in agreement with the temperature rise predicted by the thermal spike model (black squares in (a)). In contrast, when the point pitch is increased to 80 nm, a generally constant line width is achieved right from the beginning in accordance with the constant temperature prediction in Figure 2.22 (a).

This experimentally verifies that the combined approach of SRIM and thermal spike model calculations is able to predict both line widths and the effect of varying process parameters. This not only gives a deeper insight into thermal processes during FIB processing of polymers but also confirms for the first time the effect of technically-induced heating due to inappropriate scanning strategies. The latter aspect and a highly efficient workaround are both discussed in the following section. The main result of this section, however, is a presentation of the first approach for describing thermal effects in polymers during FIB processing which, to the best of our knowledge, has never been demonstrated before in a spatially and temporarily resolved manner. A detailed discussion of the calculations can also be found in reference [40].

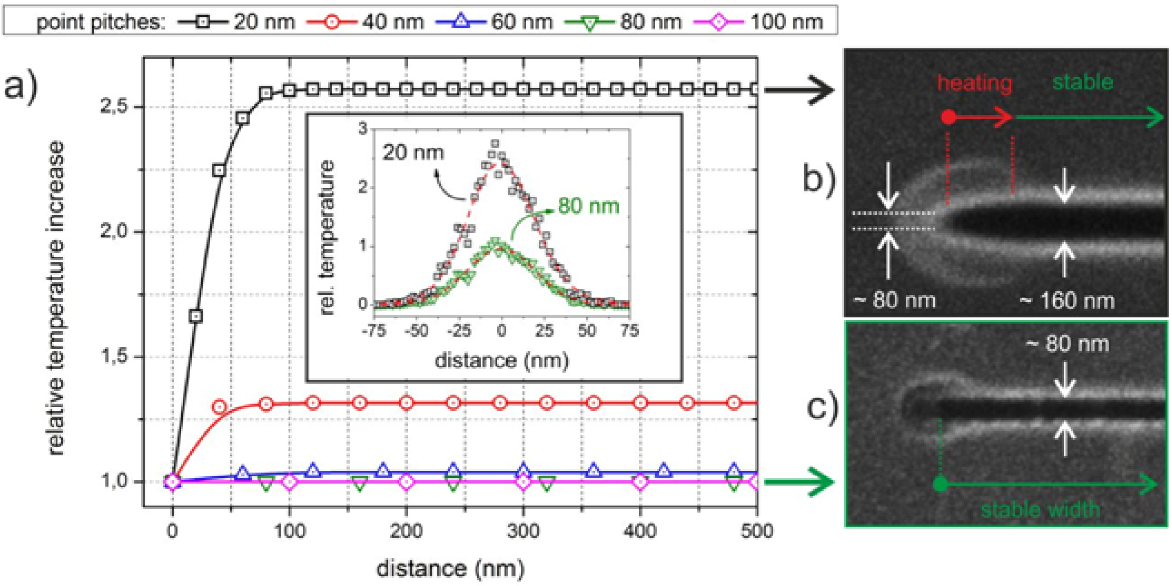

Figure 2.22.: *(a) Relative temperature evolution during regular patterning for different point pitches along the center of a PMMA single line calculated by the combined SRIM / thermal spike model approach. The lateral temperature distribution is shown in the inset for 20 nm (black squares) and 80 nm (green triangles) point pitches. (b) and (c) shows experimental FIB single lines in PMMA with 20 nm and 80 nm point pitch, respectively. As predicted by the calculations in (a) (black squares) the relative temperature should first increase and then find a stable value during patterning. This is directly observed in (b) which shows an initial line widening towards a stable value. In agreement with the predictions for a 20 nm point pitch in (a) (green triangles) the experimental single lines show generally stable line widths right from the beginning (c).*

2.4. Interlacing Strategy Characterization

As a starting point, we reconsider the findings in section 2.3. It was demonstrated that closely spaced, consecutive patterning points lead to a technically-induced heat component. To prevent this heating, it would follow that the pixel point distance must be increased so that subsequent patterning points are not mutually influenced. As can be seen in Figure 2.23, the increase from 20 nm (left) to 150 nm (right) results in a massive surface roughening which cannot be used for ideal results.

Therefore, we introduced the interlacing (**IL**) strategy which consists of a two-step procedure as schematically shown in Figure 2.24. First, the pixel distance dI is increased to minimize mutual temperature effects (a). Then, the entire pattern, indicated by 1 in the right scheme (blue boxes) in Figure 2.24 (b) is shifted by a small distance d and

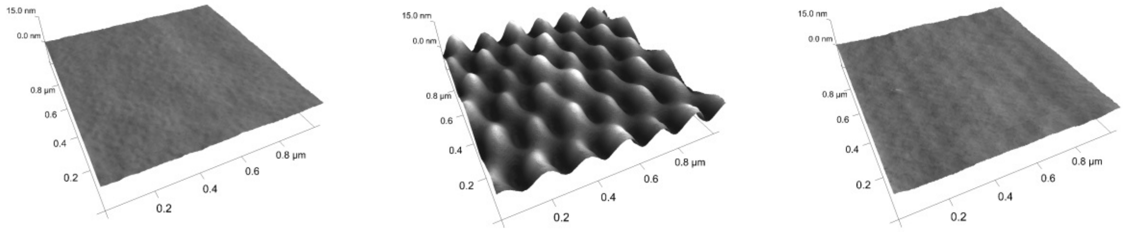

(a)

(b)

(c)

Figure 2.23.: *In-scale AFM height images of FIB structured bottom areas in PP with 20 nm PoP (a) and 150 nm PoP (b) fabricated via standard processing parameters. The right image (c) shows interlaced areas using 100 nm IL-PoP and 20 nm final PoP.*

patterned again (green boxes in the right scheme). This procedure is systematically repeated until all patterning points are addressed (see different numbers in the right scheme). The result is a very flat surface as can be seen in Figure 2.23 (b) at same process times, however, with eliminated temperature contributions from the patterning process.

Before we can demonstrate the performance of this concept we need to discuss morphological and chemical aspects in the following sections.

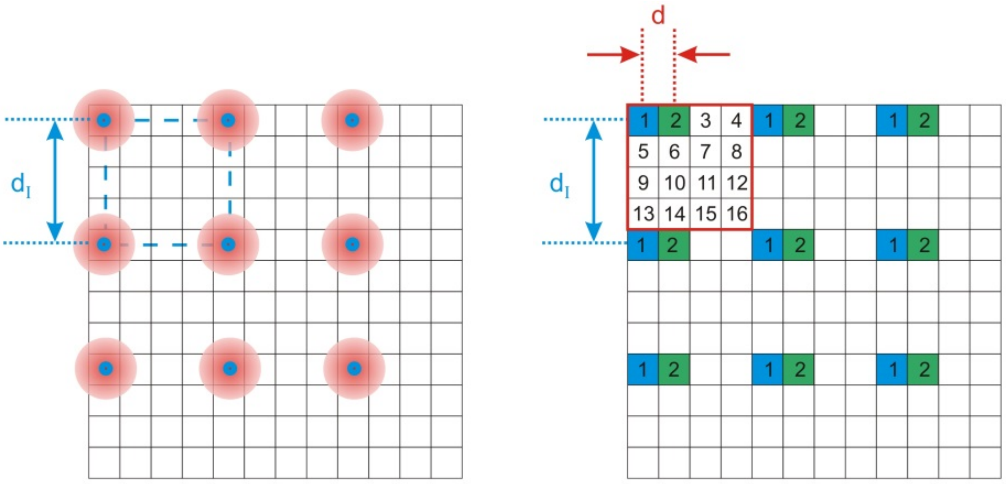

(a)

(b)

Figure 2.24.: *Interlacing (IL) patterning concept as described in the main text.*

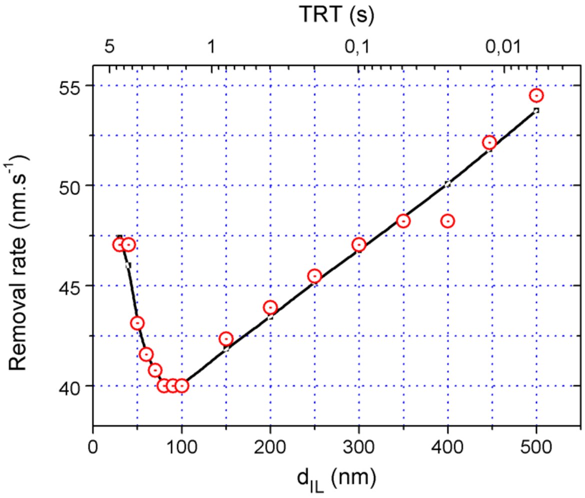

Figure 2.25.: *Interlacing point pitch variation dependency of the removal rate, revealing a minima at approximately 80 nm to 100 nm, which is the final point pitch multiplied by a factor of 4 and 5, respectively.*

2.4.1. Morphological Stability

As described above, the IL strategy uses widely spaced pixel points in each sub-frame. Furthermore, in secton 2.2.1 we have used the removal rate and its variation as an indicator of temperatures beyond the volatizing threshold. In a first step, we now consider the removal rate for an increasing pixel distance dIL in combination with the IL strategy (see Figure 2.23). Figure 2.25 shows the results for a dIL range of 30 nm to 500 nm on PP (30 kV, 500 pA) and 20 nm final point pitch d. As is evident, there is a removal rate minima between 80 nm-100 nm. At first glance, the removal rates increases again for higher IL-PoPs seem to be surprising as higher distances should even further improve the thermal situation. However, the patterning footprint has to be kept in mind which has been 2×2 μm2 for these experiments. This leads to the situation that the cooling time per pixel point is decreased for increasing dIL as a smaller number of pixels have been patterned in each sub-frame. Therefore, a total refresh time (**TRT**) has been introduced in the top axis of Figure 2.25 showing the decreasing cooling times for increasing point pitches. This demonstrates that the cooling times also play a major role and the patterning footprint becomes relevant as well.

To compensate for this TRT related drawback, we have introduced the smart interlacing (**SIL**) strategy, which expands the IL approach by including a history check. This ensures that consecutive points in close proximity during different frames fulfil a minimum cooling time. These points are then sorted out, stored and patterned later. A representative

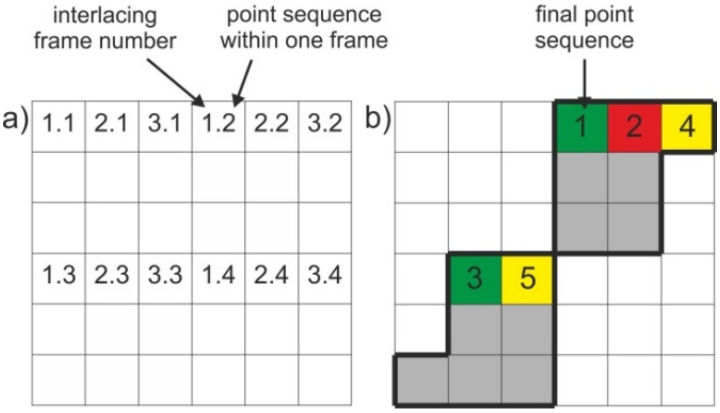

Figure 2.26.: *(a) Scheme of an interlacing strategy, where in 'X.Y' X gives the frame sequence and Y the sequence of points within one frame. (b) The grey, encircled area is an example of a pattern. In this case neighbouring points are patterned consecutively (indicated in red) or within a very short time (indicated in yellow) if the basic interlacing strategy shown in (a) is used.*

example is shown in Figure 2.26: the left scheme indicates the basic interlacing mask by the frame number (first number) and point number (second number). The right scheme gives a special case in which only the grey pixels should be patterned. The colored boxes then give the real patterning sequence by the basic IL strategy (compare to left scheme). As is evident, the final sequence leads to an almost consecutive procedure which will result in massive heating effects. The SIL strategy, however, compensates this drawback and allow structuring of any pattern shape in any size with minimally increased process times.

To directly visualize the reduced temperatures by the SIL approach, we have performed the same dwell time experiments as shown and discussed in section 2.2. Dwell time variation experiments can be seen in Figure 2.27 (left), showing a comparison between standard and IL strategies for RT and CT conditions (see legend). The right part of Figure 2.27 gives a PoP sweep for 500 s (top) and 5 s (bottom) performed via standard (blue) and IL strategies (green) at room temperature. In both cases it is clearly evident that the IL strategy does not show any removal rate increase which indicates that even for the harshest conditions, the volatizing threshold is not reached.

The most remarkable detail however, is the fact that the IL strategy works ideally already at room temperature conditions making cryogenic stages unnecessary for these applications. Furthermore, it has to be kept in mind that the process times are identical making this approach simple and straightforward. The above-mentioned TRT problem

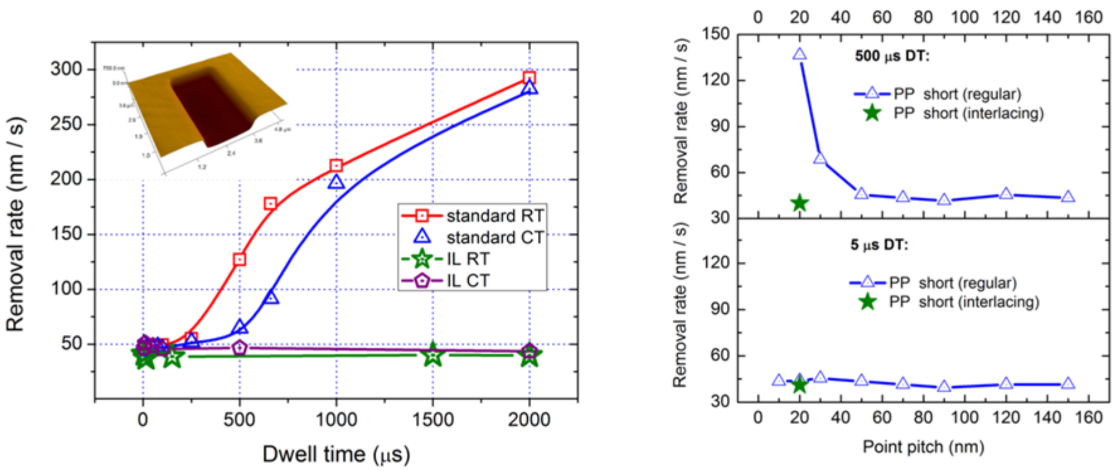

Figure 2.27.: *Direct performance comparison between standard and interlacing (IL) patterning strategies. The left graphic shows the dwell time sweeps for standard patterning at RT (red) and CT (blue) both showing the massive increase related to a temperature increase beyond the volatizing threshold. In contrast, IL strategies at CT (purple) and at RT (green) do not show any signs of increased removal rates even for the highest dwell times in the ms range. The top left inset shows an AFM height image of an IL pattern at RT revealing perfectly flat bottom areas as intended. The right graphic gives a PoP sweep for different dwell times (see legend) and compares standard patterning (blue) and IL results (green stars) again not showing increased removal rates even for the smallest PoPs of 20 nm. All experiments have been performed at 30 kV and 500 pA in PP.*

is also addressed by the introduction of the SIL strategy and leads to ideal results at slightly increased process times for very small and/or special geometries.

2.4.2. Chemical Stability

After demonstrating the significant improvements for IL strategies with respect to morphological issues, its influence on the chemical degradation is of particular importance. As shown for the regular patterning, the Raman spectroscopy serves as a tool for measuring the chemical degradation by integrating the characteristic peaks (see section 2.2.2).

Figure 2.28 summarizes the dwell time dependent results for PP by comparing regular (red and blue) with IL strategies (green and olive) at RT and CT conditions (see legend). As clearly evident, IL processing reveals strongly increased Raman intensity even for dwell times in the ms range. Furthermore, in agreement with the findings in the previous section, the difference between RT and CT conditions during IL patterning is very small.

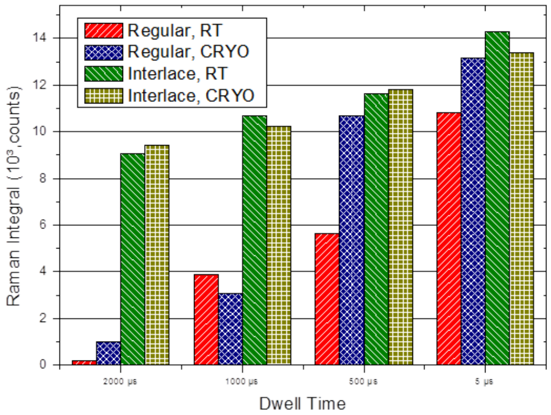

Figure 2.28.: *Comparison of PP related, characteristic Raman integrals in dependence on the used dwell times. In more detail, the plot compares regular with IL patterning strategies for RT and CT conditions.*

Figure 2.29 shows the results for HDPE (left) and PMMA (right) by direct regular IL comparison in dependence on the dwell time. Again, the very stable chemical signal for IL patterning is clearly visible and it should be kept in mind that the X-axes in these plots are logarithmic. These measurements clearly prove that the chemical damage can be kept at a minimum for IL strategies over a very large range of parameters. It also allows to conclude that this strategy approaches the unavoidable damage by means of direct ion-matter interaction and eliminates any additional component by improper patterning parameters.

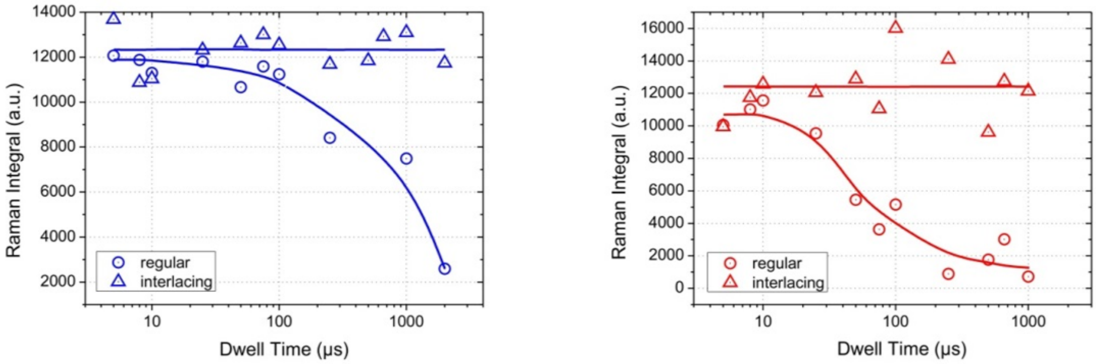

Figure 2.29.: *dwell time dependent characteristic Raman signals for HDPE (left) and PMMA (right) for standard (triangles) and IL patterning strategies (circles) fabricated at room temperature conditions.*

2.4.3. Material Related Effects

Finally, we have investigated material related effects by means of different processes during temperature rises. As discussed in section 2.2.2 and 2.4.2 two extremes exist: 1) chain scission (**CS**) defined by chain cleavage during temperature increase; and 2) cross linking (**CL**) of adjacent polymer chains. While PMMA is a strong CS representative, HDPE is a classical CL polymer which is the reason why we chose these materials initially. Figure 2.30 summarizes the chemical effects characterized via Raman spectroscopy (top and bottom panels) in dependence on the pixel dwell time for regular (left column) and IL strategies (right column) and PMMA (upper half) and HDPE (lower half). We start the discussion with morphological effects for increasing dwell times as shown in Figure 2.30 (c). As can be seen, PMMA shows widely flat morphologies for the shortest dwell time correlated with highest Raman signals (a). This region is further denoted as regime 1 which reflects the intrinsic damage during FIB processing including small pinholes in the bottom areas. For highest dwell times, the Raman signal goes practically to zero indicating complete chain scission allowing the material to volatize. This area is further denoted as regime 3 showing entirely improper morphologies (c). The region in between leads to material modification by means of partial chain scission (see a) leading to destabilized morphologies as shown in Figure 2.30 (c). Hence, this modified area is further denoted as region 2. Applying the same procedures to HDPE as CL representative, the situation changes. First, it can be seen that region 2 is not destabilized but still flat as a consequence of increasingly cross linked molecules which improves morphological stability. Nevertheless, Raman spectra indicate a decay which justifies the notation as region 2 by means of modified materials. For very high DTs the Raman again shows signals close to zero which suggests volatizing processes and explains the unstable morphology in Figure 2.30(e).

When changing now to IL strategies the situation is much improved as can be seen in the right column of Figure 2.30. For PMMA as a CS representative it becomes obvious that the destabilized regime 2 is strongly shifted to highest dwell times (d) in agreement with the corresponding Raman spectra in Figure 2.30b. For CL materials, the situation is even better as neither morphological destabilization (d) nor chemical degradation (f) can be observed. In other words, regime 1 reflects the unavoidable, intrinsic damage. Regime 2 represents modified material properties due to the increasing temperatures during patterning. The limit is regime 3 in which the polymer chains are so short that they can volatize directly, which entirely destabilizes the morphology. The IL strategy

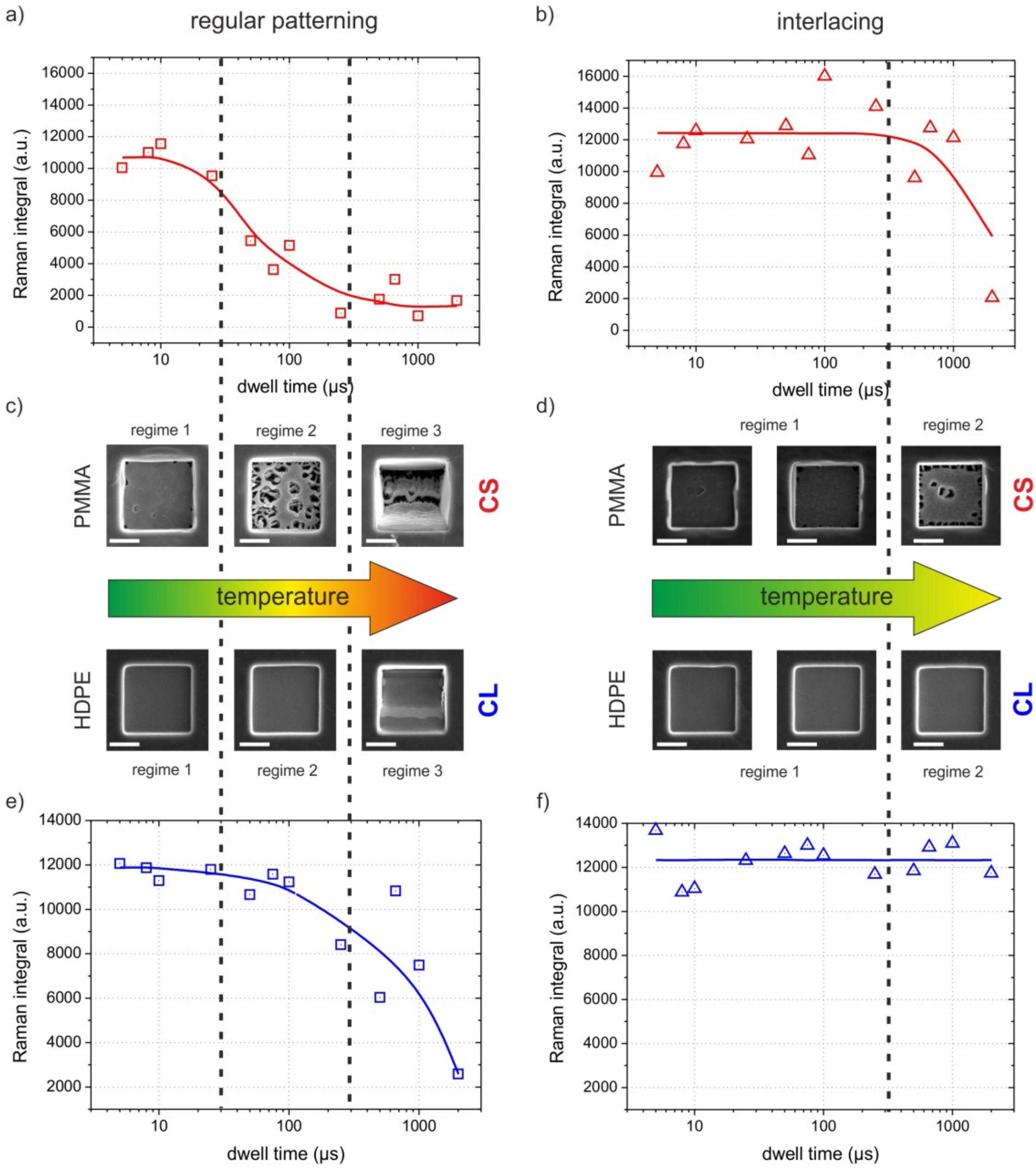

Figure 2.30.: *Integrated Raman signals for characteristic material peaks of PMMA (upper row) and HDPE (lower row) fabricated via regular (left column) and IL patterning (right column). The central row shows SEM images revealing three different regimes for CS and CL materials. The scale bars in the SEM images are always 2 μm. A detailed explanation can be found in the main text.*

actually decreases local temperatures thereby providing much more stable morphologies and functionalities. A detailed discussion of material-related effects can be found in reference [32].

In conclusion it can be stated that even different polymer classes strongly benefit from IL strategies by means of increased chemical and morphological stabilities without increasing the process times. Therefore, IL patterning can be considered to be a strategy which minimizes technically-induced heating components and shifts the working regime strongly towards the unavoidable damage due to direct ion-polymer interaction.

2.5. Applications

Finally, two examples are shown which demonstrate the greatly improved possibilities afforded by using the interlacing strategy introduced here. First, we show how even sensitive materials can be structured in a manner which often has been considered as complicated or even impossible. The second part concerns the very critical topic of FIB based preparation of ultrathin TEM lamellas. Using regular FIB processing one has to cope with many challenges when working with low melting materials such as chemical interlayer mixing, morphological delamination or chemical degradation in general. Therefore the interlacing strategy is applied for a validation of the introduced IL strategy. As test samples, different types of organic thin film transistors (**OTFT**) and different polymeric layer systems with or without metal separation layer were used.

2.5.1. FIB Structuring of Polymers

As described in the previous sections, PMMA is a very challenging polymer as it easily undergoes modification processes at increasing temperatures. Therefore, we have chosen this test material for the fabrication of an inter-digital structure. As shown by the top left image in Figure 2.31, a single pass pattern using 30 kV, 500 pA, 20 nm PoP and 2 ms DT leads to entirely rugged surfaces which cannot be used for real applications. The first intention would be a strong reduction of the ion beam current. This can be seen in the top right image of Figure 2.31 where the same pattern was used, however, with a reduced beam current of 100 pA. Although the results are improved, it is still evident that such a process step cannot be used for real applications. Finally, we chose the high beam current of 500 pA together with long dwell times of 2 ms in combination with the interlacing strategy. The impressive result is shown at the bottom in Figure 2.31 which clearly prooves the massive improvement just by changing the point sequence thereby eliminating the technically-induced heating components. As the interlacing strategy can

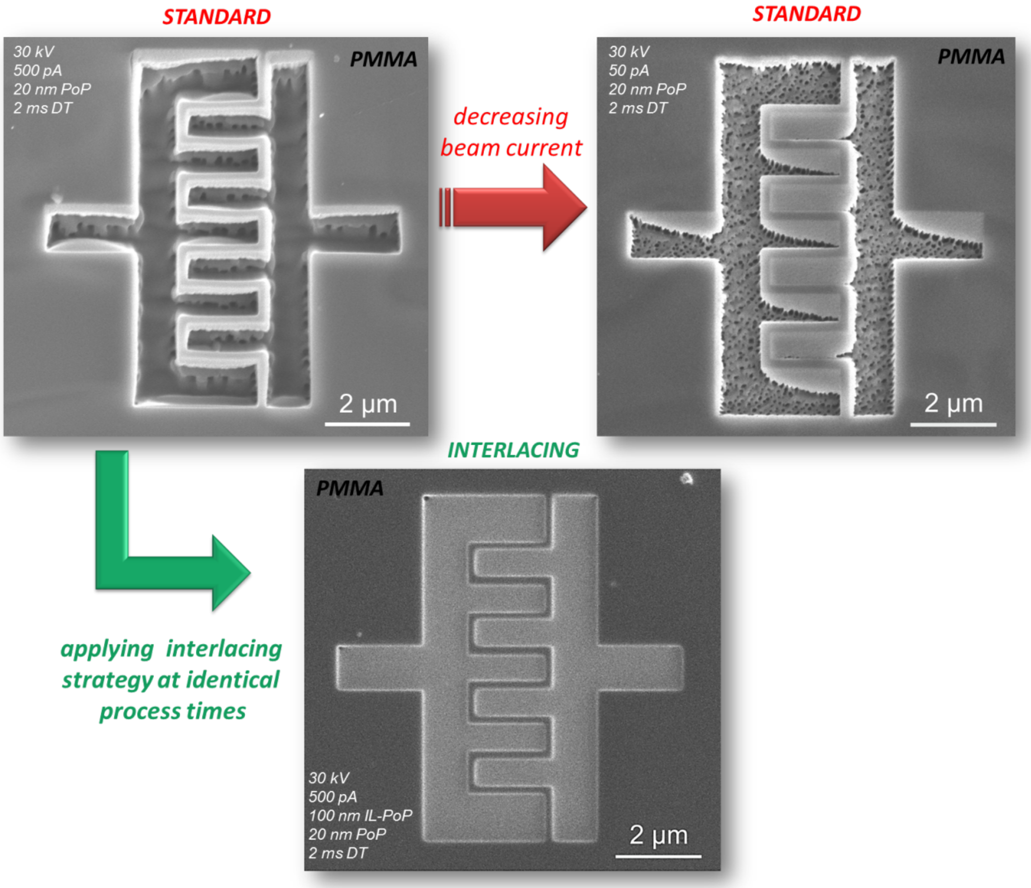

Figure 2.31.: *Proof of the concept regarding improved structuring capabilities due to application of an interlacing strategy. The top row shows the morphological result of standard FIB processing on PMMA surfaces performed at 30 keV, 20 nm PoP, 2 ms DT via single pass processing. The top left image is the result for a 500 pA beam current while the top right image shows the structure for a 100 pA beam current which demonstrates that simple current reduction is not sufficient. When changing from standard to interlacing patterning by using the same pattern with 500 pA, the structure shows excellent morphological stability as can be seen in the bottom image. These images can be seen as successful proof-of-concept developed during this PhD thesis.*

also be seen as a method which reduces the local temperatures towards the unavoidable value during direct ion-polymer interaction, this image can also be considered to be the result of predominant intrinsic effects. That provides the successful proof-of-concept which might open up new possibilities for soft matter processing via focused ion beams which has been considered to be very complicated or even impossible in the past.

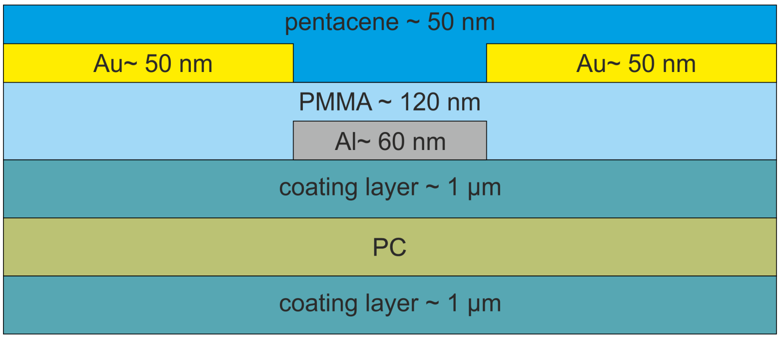

Figure 2.32.: *Cross-sectional scheme of an OTFT structure used for IL based FIB lamella preparation for TEM investigations.*

2.5.2. TEM Lamella Preparation of an Organic Thin Film Transistor

As TEM is a very important method for structural or chemical analysis, e.g. via EELS, it is of particular importance to provide a sample preparation method with a minimum of preparation artefacts. This gets more and more challenging since the TEM analytics have been further developed by means of energy resolution and are able to investigate fine structures of ionization edges and plasmonic peaks in detail which allows the investigation of preparation artefacts. As a starting point, an OTFT is used to demonstrate the challenges which have to be overcome to optimize the process of preparing TEM lamellas when dealing with soft matter.

For an extensive performance test, different OTFT structures have been used for the fabrication of TEM lamella. Figure 2.32 shows the cross sectional setup of the OTFT structure used. In a first step, a sample without the pentacene top layer was used to investigate whether the highly sensitive PMMA layer can be maintained. Lamella preparation followed standard FIB: first electron beam induced Pt deposition followed by ion beam induced Pt deposition was used to protect the relevant area. Afterwards, two trenches were milled with regular patterning strategies using regular cross-section patterns at 30 kV and 500 pA. After thinning to about 3 μm in thickness, the thinning process is the next step achieved by applying the interlacing strategy using $20 \times 2\,\mu\text{m}^2$ patterns with 20 nm PoP, 100 nm IL-PoP and 500 μs DT. This process is repeated until the lamella is approximately 1 μm thin. Next, the so-called U-cut was done using the IL strategy to allow the subsequent lift-out via the micromanipulator. After transfer and fixation at the TEM grid, final thinning processes were started.

These processes were not performed for the entire lamella, but only for a small, 4 μm wide window in the center of the lamella due to stability reasons. This step has been

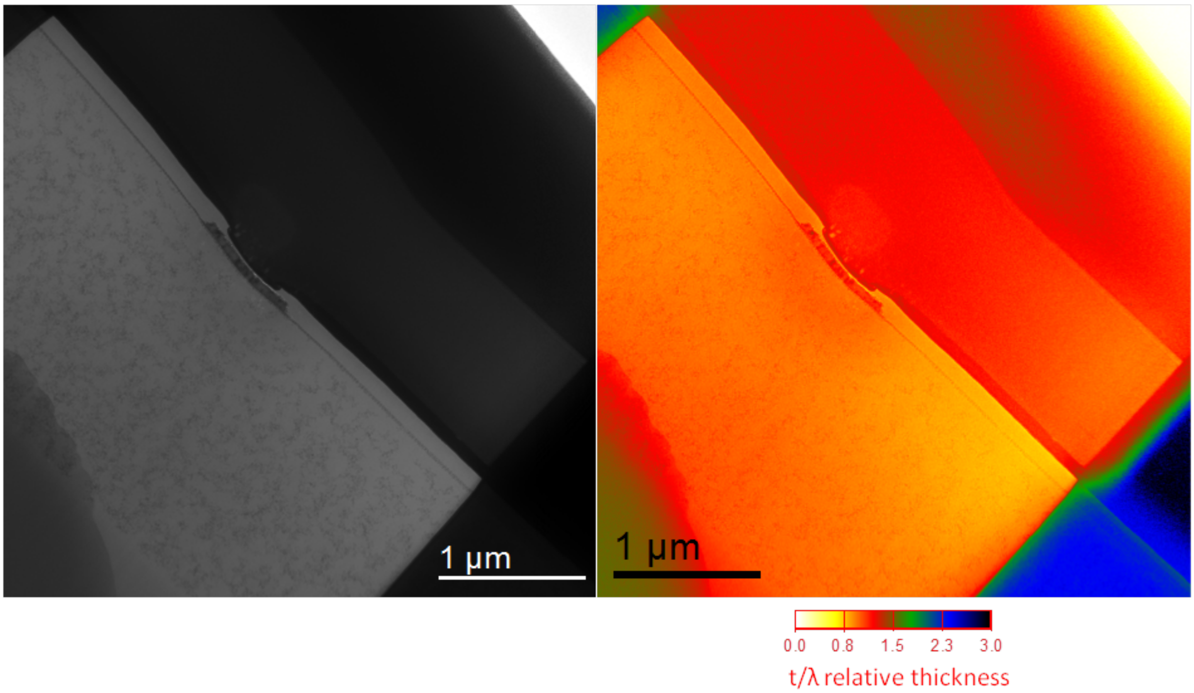

Figure 2.33.: *Zero-loss filtered bright field TEM Image (left) and t/λ map (right) indicating the relative lamella thickness revealing the thin and very homogeneous character as needed for reliable high-resolution TEM / EELS analysis.*

done at a beam current of 500 pA towards a thickness of about 500 nm without tilting the sample. Subsequently, the beam current was reduced to 100 pA and the lamella was tilted by 2° to suppressing a wedge-like shape from the thin top to the thick bottom end. From this point on, the pattern shape was adjusted to a $4 \times 0.1\,\mu m^2$ size for minimized sample stress. At a thickness of approximately 200 nm the ion beam current was further decreased to 50 pA. By simplly approaching the window in 50 nm steps at each pass of the pattern on each side a final thickness of approximately 80 nm was obtained, as can be seen at the final TEM lamella and the related t/λ thickness map in Figure 2.33 left and right, respectively. The first detail in the latter map is the very homogeneous thickness across the milled window reflected by the homogeneous color. This map also reveals the metal parts of the OTFT, as there is an Al gate and Au source and drain contacts.

The left image in Figure 2.34 shows a HAADF TEM image at higher magnification revealing a very thin polymeric (PMMA) layer on top of the gate electrode. The essential detail is the absence of any delamination which often occurs for such thin polymers after FIB preparation. This is further proven by EFTEM investigations at even higher magnification shown at the right side of Figure 2.34 by the red regions on top of the

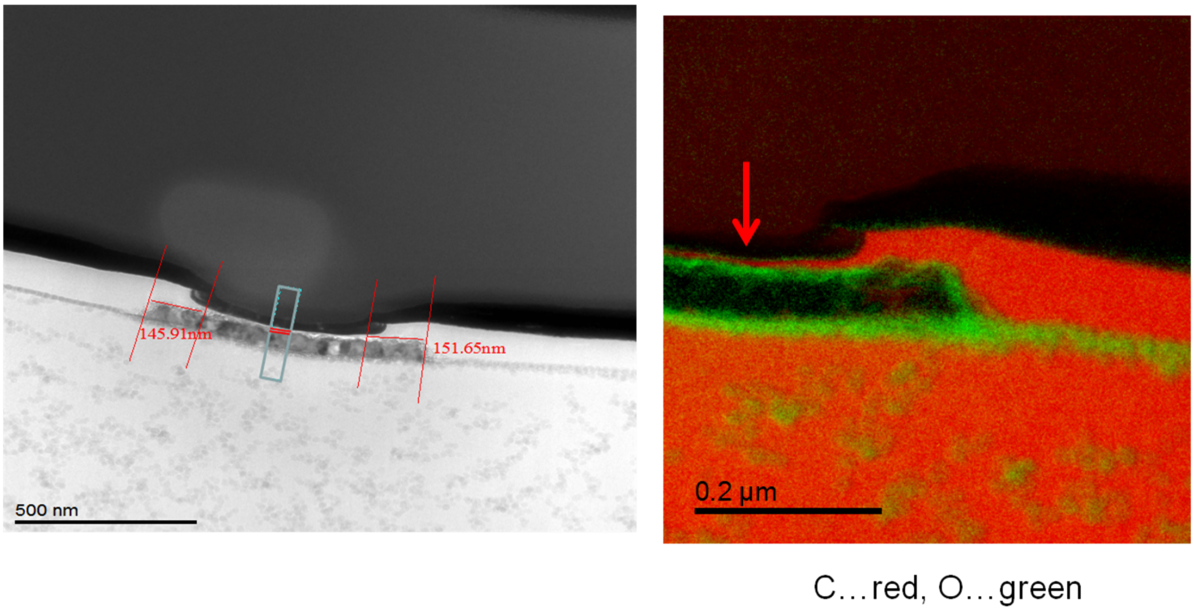

Figure 2.34.: *HAADF TEM image (left) and EFTEM image (right) of the region of interest revealing an approximately 10 nm thick polymeric (PMMA) layer (red) without delamination and chemical mixing. The green regions indicate the* AlO_X *which are clearly separated.*

AlOX layer in green (see arrows). A detailed description of the successful TEM related analysis can be found in reference [21].

The main result of this section is that we have demonstrated the added value of IL based FIB processing on polymeric layers without complete chemical degradation and/or delamination effects even for highly sensitive polymer layers as thin as 10 nm. Therefore, the IL approach can not only be used for (functional) structuring but also for preparation purposes, which has been very complicated in the past.

2.5.3. TEM Lamella Preparation of a Layered Polymeric Sample

After showing the interlacing strategy to be fully compatible with the TEM lamella preparation of an OTFT, the next challenge arose with a fully polymeric layered structure without any metallic interlayers, which can be seen in 2.36. This structure was produced by spin casting and the polymer types were chosen to be compatible with the process of nanoimprint lithography with which a fully printable OTFT can be produced. First tests of the polymeric layered structure were performed to be compatible with the TEM investigations and therefore the structure has to be prepared.

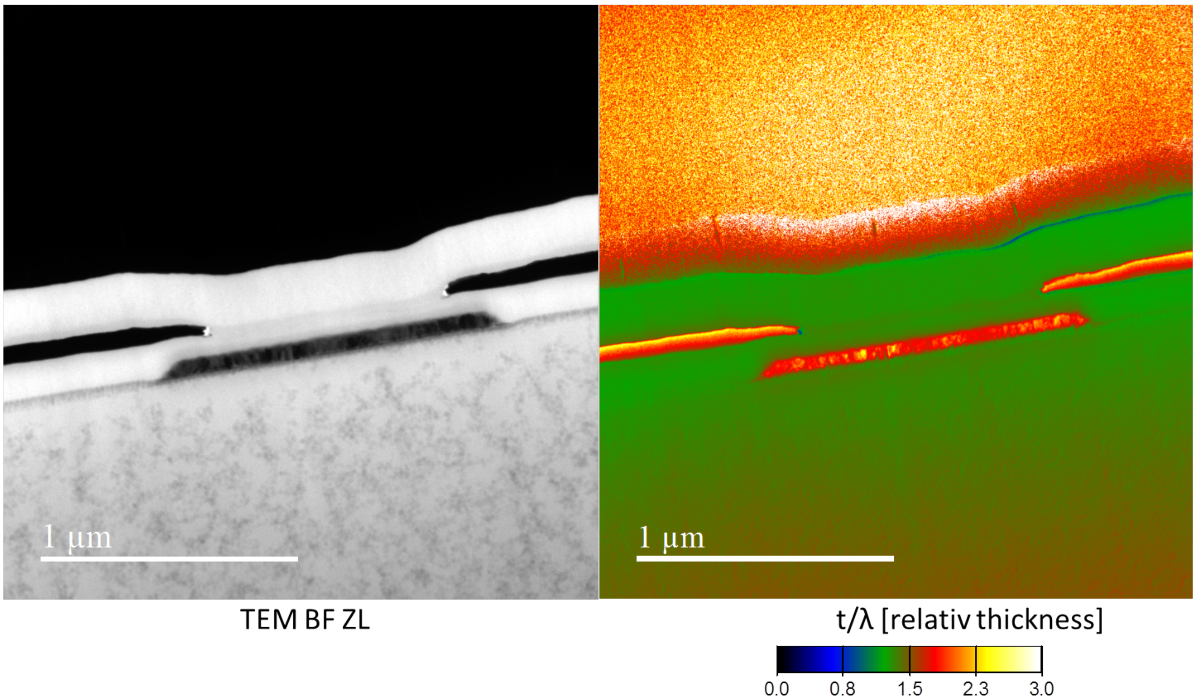

Figure 2.35.: *TEM BF zero-loss filtered and relative thickness map of final OTFT sample revealing a preaparation without layer delamination and interlayer mixing due to changed protection layer - and interlacing strategy.*

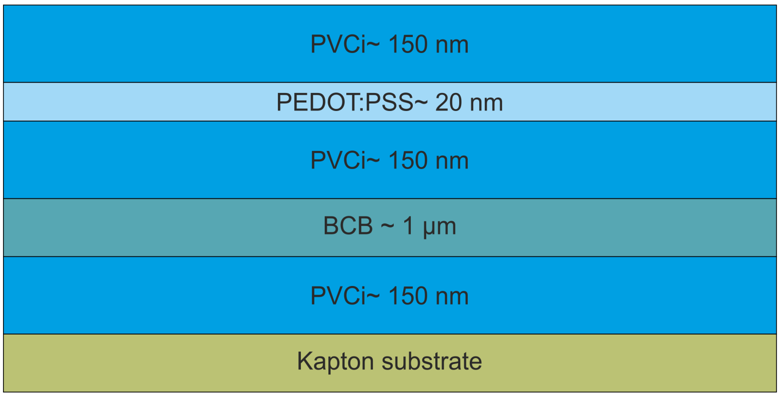

Figure 2.36.: *Illustration of the layered fully polymeric structure serving as a testsample for demonstrating the compatibility of TEM lamella preparation with the interlacing strategy in such a critical sample.*

First of all an approximately 80 nm thick Pt/Pd protective layer was sputtered on top of the structure so as to not damage the area of investigation with the ion beam. Afterwards, the same procedure as described in section 2.5.2 was applied. The outcome can be seen in Figure 2.37 by an STEM bright field image (left) and the signal intensity of heteroatoms (right) for differentiation of the various polymeric layers.

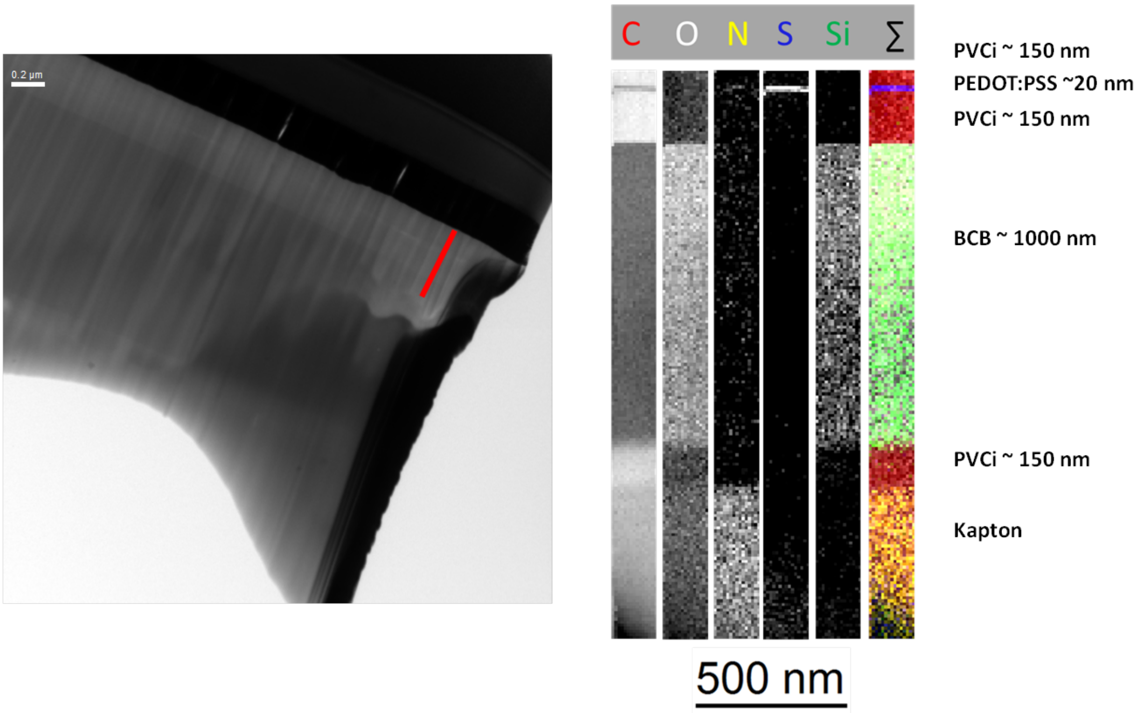

Figure 2.37.: *STEM bright field image (left) of the prepared lamella with the area marked that was used for EELS and EDX analysis for material differentiation and signal intensitiy of heteroatoms from EELS and EDX signals respectively clearly showing the layered structure.*

In the STEM image the curtaining effect can be cleary seen, which is due to the inhomogeneous protective Pt/Pd layer and could be eliminated by performing an upside-down preparation. But, as one can see in the analytical data, a clear differentiation between the polymeric layers down to approximately 20 nm can be achieved even with a non-optimal lamella such as this. Furthermore no layer intermixing and delamination is observable, which is often a severe problem in the preparation of polymeric samples and can be eliminated by using the interlacing strategy.

3. Summary

In this PhD thesis, focused ion beam processing of polymers is investigated by experiments and simulations. In more detail, the classically-used patterning procedures were shown to be improper and to lead to additional heating effects. These findings were then correlated with theoretical considerations and corresponding simulations which proved the presence of this technically-induced heating component. Based on the deep fundamental insight gained during this PhD thesis into the underlying processes, a counterstrategy was developed which was successfully able to minimize technical drawbacks. This not only enabled FIB surface structuring of highly sensitive polymers, but also was applied for the fabrication of ultra-thin lamellas for transmission electron microscopy investigations. In this way, the study ranges from experimental investigations to theoretical considerations as the fundamental aspect for the development of highly efficient counter-strategies which can be applied for real applications in the field of soft matter FIB processing.

The study started with removal rate variation during dwell time and point pitch variation as discussed in section 2.2.1. It could be shown that increasing the former and/or decreasing the latter leads to massive removal rate increases at constant total doses. Extensive correlation with different polymer types revealed the observable increase as an indicator that the temperatures in the proximity of the ion beam were exceeding the volatizing threshold, leading to thermally assisted evaporation, which explained the elevated removal rates. The first astonishing result was the observation that even cryogenic temperatures of - 150 °C could not prevent but only delay this proximity heating. This demonstrated that the application of complicated cryogenic sample stages is not a guarantee to compensate for this massive heating during FIB processing. The reason for this behavior can be found in the very low thermal conductivity of polymers which prevents sufficient heat transfer to surrounding areas.

Beside these morphological aspects, polymers are also damaged chemically as is discussed extensively in section 2.2.2. By using Raman spectroscopy as ideal tool for degradation characterization, we were able to observe damage behavior very similar to the removal rate dependencies described above. Also we were able to support the hypothesis that even cryogenic temperatures cannot prevent but only delay chemical degradation due to thermal conductivity issues of polymers.

At the same time, we initiated a theoretical consideration to gain deeper understanding of the fundamental processes during FIB processing as covered in section 2.3. In a first step, we used finite element simulations (section 2.3.1) to estimate the relative temperature evolution with a laterally resolved character. This led to the identification of a technically-induced component when a pattern consists of closely spaced, consecutively executed patterning points. The problem arises as the lateral temperature distribution exceeds typically used pixel spacing which leads to the situation that subsequent patterning points then already start at elevated temperatures. This process leads to increasing temperatures at the beam center but also in its proximity, which later settles in stable temperature values once the thermodynamic equilibrium is reached. However, the predictions could not be verified by the finite element method due to a lack of computing power for the large areas under consideration. Therefore, we developed a new approach based on the thermal spike model which is easier to handle but still has been proven in the past to be very powerful approach for inorganic materials. As this model can describe spatially resolved situations, proper input data were necessary which describe the ion beam impingement and related trajectories in the polymer. This was realized by careful simulations via the software package SRIM (section 2.3.2). First, we extracted spatially resolved phonon distributions for the polymers and used this information as input data for the thermal spike model (section 2.3.3). The first main results were hypothetical temperature spikes with a laterally resolved character suggesting temperatures up to 6000°C as this model entirely ignores material sputtering and/or evaporation. The latter aspect was then introduced by careful polymer analysis via thermodynamic methods (section 2.1). These investigations allowed a classification of the polymers into solid (pristine), melt (liquid / modified) and volatized states. The latter were then combined with the simulation results by the thermal spike model to estimate the expansion of volatized regions. Subsequently, we correlated the predictions with experimental single line widths after FIB processing and found excellent agreement between them. After this successful correlation we applied the combined SRIM / thermal spike model approach for the estimation of temperature effects during patterning which failed via the finite element approach due to technical limitations. This led on the one hand to a conformation of the predicted effect of a technically-induced heating component and on the other hand to a prediction that single lines with critical conditions should actually show an initial widening followed by a constant width. Again, experiments revealed the suggested behavior which further proved the applicability of the simulation approach introduced here. Beside the aspect that we successfully developed a method for spatially and temporally resolved prediction of temperature effects during FIB processing, we also gained a deeper knowledge of the fundamental processes involved.

Based on this progress, we focused on the technically-induced heating component and derived a concept which was able to eliminate this effect: the interlacing strategy. This approach consists of a multi - step process: first, a large pixel spacing is used which exceeds the thermal expansion zone from consecutive patterning points. Second, this pattern is then systematically shifted by very small distances to achieve very small final pixel distances to provide nano-flat surfaces (section 2.4). By applying this approach, we were able to successfully prevent any removal rate variations which proved that local and proximal temperatures did not exceed the volatizing threshold (section 2.4.1). As another major achievement, we demonstrated that this strategy works at room temperature as effectively as at cryogenic temperatures, which entirely eliminates the application of low-temperature sample stages. Detailed investigations, however, revealed an influence from pattern sizes and shapes which finally led to the development of a smart interlacing code which accounts for this drawback and allows highly efficient processing of arbitrary shape pattern geometries. After this, we once again investigated chemical aspects using Raman spectroscopy (section 2.4.2). It could be successfully proven that the morphological improvements are accompanied by a strongly reduced chemical degradation which is of essential importance when aiming for intact functionalities on the structured sample surfaces. Finally, polymer-specific effects during FIB processing were investigated (section 2.4.3). For this purpose, the extremes of predominant chain scission and cross linking behavior for increasing temperatures were studied in detail. While these polymer classes show very different effects during classical FIB processing, it could be shown that the interlacing approach is capable of minimizing both morphological instabilities as well as chemical degradation. This means that the alternative patterning approach introduced here can be used for a wide variety of polymer types by a reduction of thermal stress moving towards the unavoidable, intrinsic limit given by local ion - polymer interactions.

Finally, secton 2.5 demonstrated the successful application of the interlacing strategy. First, very sensitive polymer layers were used to demonstrate the massive improvement achieved using the interlacing strategy as shown in Figure 3.1. The result can be understood to be a successful proof-of-concept for the elimination of technically-induced heating by classical patterning strategies. In a second application we successfully incorporated the interlacing strategy during FIB preparation of ultra-thin lamellas for transmission electron microscopy. We demonstrated that this approach is capable of preventing delamination effects in nanometer- hick polymer layers which were often the main issue in the past. Both applications reflect the great benefit of the alternative patterning strategy which has been developed as a result to a fundamental understanding of thermal processes during FIB processing of low melting materials.

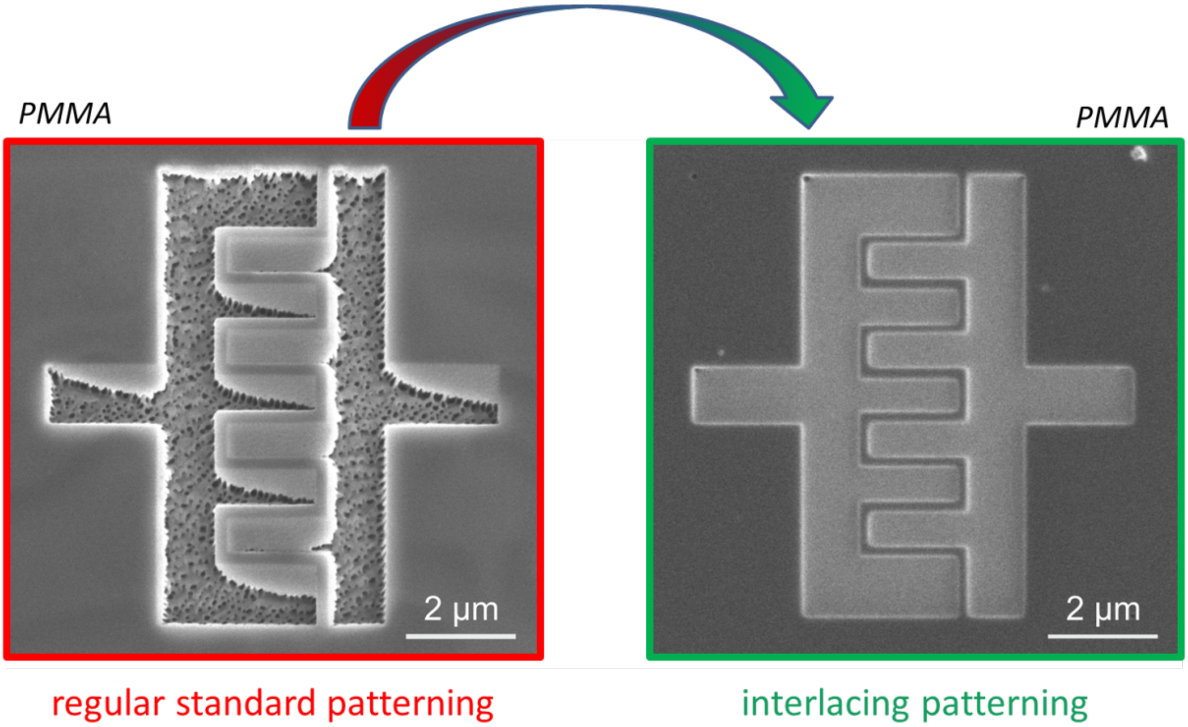

Figure 3.1.: *Direct comparison of classical (left) and interlacing patterning strategies (right) for the same process times.*

References

[1] Courtesy of Claudia Mayrhofer, Institute for Electron Microscopy and Nanoanalysis, Graz University of Technology, Steyrergasse 17, 8010 Graz, Austria.

[2] Courtesy of Harald Plank, Institute for Electron Microscopy and Nanoanalysis, Graz University of Technology, Steyrergasse 17, 8010 Graz, Austria.

[3] URL `www.semclean.com`.

[4] M. Y. Ali, W. Hung, and F. Yongqi. A Review of Focused Ion Beam Sputtering. *International Journal of Precision Engineering and Manufacturing*, 11(1):157–170, Feb. 2010. ISSN 1229-8557. doi: 10.1007/s12541-010-0019-y.

[5] I. V. Amirkhanov, A. Y. Didyk, D. Z. Muzafarov, I. V. Puzynin, T. P. Puzynina, N. R. Sarker, I. Sarhadov, and Z. A. Sharipov. Investigation of thermal processes in one- and two-layer materials under irradiation with high-energy heavy ions within the thermal peak model. *Crystallography Reports*, 51(1):S32–S43, 2006. ISSN 1063-7745. doi: 10.1134/S1063774506070078.

[6] N. D. Bassim, B. T. De Gregorio, A. L. D. Kilcoyne, K. Scott, T. Chou, S. Wirick, G. Cody, and R. M. Stroud. Minimizing damage during FIB sample preparation of soft materials. *Journal of Microscopy*, 245(3):288–301, 2012. ISSN 0022-2720. doi: 10.1111/j.1365-2818.2011.03570.x.

[7] W. Brostow, B. P. Gorman, and O. Olea-Mejia. Focused ion beam milling and scanning electron microscopy characterization of polymer+ metal hybrids. *Materials Letters*, 61(6):1333–1336, 2007.

[8] C. Dufour, A. Audouard, F. Beuneu, J. Dural, J. P. Girard, A. Hairie, M. Levalois, E. Paumier, and M. Toulemonde. A High-Resistivity Phase Induced by Swift Heavy-Ion Irradiation of Bi - A Probe for Thermal Spike Damage. *Journal of*

Physics-Condensed Matter, 5(26):4573–4584, June 1993. ISSN 0953-8984. doi: 10.1088/0953-8984/5/26/027.

[9] R. F. Egerton, P. Li, and M. Malac. Radiation damage in the TEM and SEM. *Micron*, 35(6):399–409, Jan. 2004. ISSN 0968-4328. doi: 10.1016/j.micron.2004.02.003.

[10] A. C. French, A. L. Thompson, and B. G. Davis. High-purity discrete PEG-oligomer crystals allow structural insight. *Angewandte Chemie (International ed. in English)*, 48(7):1248–52, Jan. 2009. ISSN 1521-3773. doi: 10.1002/anie.200804623.

[11] L. A. Giannuzzi and F. A. Stevie. *Introduction to focused ion beams: instrumentation, theory, techniques, and practice*. Springer, New York, xviii edition, 2005.

[12] J. Goldstein, D. Newbury, D. Joy, C. Lyman, P. Echlin, E. Lifshin, L. Sawyer, and J. Michael. *Scanning Electron Microscopy and X-ray Microanalysis*, volume 1. 2003. ISBN 0306472929.

[13] M. F. Hayles, D. J. Stokes, D. Phifer, and K. C. Findlay. A technique for improved focused ion beam milling of cryo-prepared life science specimens. *Journal of Microscopy*, 226(3):263–269, 2007.

[14] Hobbs. *Introduction to Analytical Electron Microscopy*. Plenum Press, New York, 1979.

[15] G. A. Khoury and B. Willoughby. Polypropylene fibres in heated concrete. Part 1: Molecular structure and materials behaviour. *Magazine of Concrete Research*, 60(2): 125–136, 2008. ISSN 0024-9831. doi: 10.1680/macr.2008.60.2.125.

[16] D. Kiener, C. Motz, M. Rester, M. Jenko, and G. Dehm. FIB damage of Cu and possible consequences for miniaturized mechanical tests. *Materials Science and Engineering A*, 459:262–272, 2007. ISSN 09215093. doi: 10.1016/j.msea.2007.01.046.

[17] S. Kim, M. J. Park, N. P. Balsara, G. Liu, and A. M. Minor. Minimization of focused ion beam damage in nanostructured polymer thin films. *Ultramicroscopy*, 111(3):191–199, Feb. 2011. ISSN 0304-3991. doi: 10.1016/j.ultramic.2010.11.027.

[18] Y.-K. Kim, A. J. Danner, J. J. Raftery, and K. D. Choquette. Focused Ion Beam Nanopatterning for Optoelectronic Device Fabrication. *Selected Topics in Quantum Electronics, IEEE Journal of*, 11(6):1292–1298, Nov. 2005. ISSN 1077-260X. doi: 10.1109/JSTQE.2005.859022.

[19] J. J. Kochumalayil, A. Meiser, F. Soldera, and W. Possart. Focused ion beam irradiation - morphological and chemical evolution in PMMA. *Surface and Interface Analysis*, 41(5):412–420, 2009. ISSN 0142-2421. doi: 10.1002/sia.3042.

[20] S. Koltzenburg, M. Maskos, and O. Nuyken. *Polymere: Synthese, Eigenschaften und Anwendungen*. SPRINGER-VERLAG, 2014.

[21] J. Kraxner. Analytical TEM in Organic Electronics. *Imaging & Analysis*, 2014. URL `http://www.imaging-git.com/science/electron-and-ion-microscopy/analytical-tem-organic-electronics?page=1`.

[22] R. M. Langford, P. M. Nellen, J. Gierak, and Y. Fu. Focused ion beam micro- and nanoengineering. *MRS Bulletin*, 32(5):417–423, 2007. ISSN 0883-7694. doi: 10.1557/mrs2007.65.

[23] A. Liscio, V. Palermo, K. Mullen, and P. Samori. TipSample Interactions in Kelvin Probe Force Microscopy: Quantitative Measurement of the Local Surface Potential. *The Journal of Physical Chemistry C*, 112(44):17368–17377, 2008. doi: 10.1021/jp806657k.

[24] M. Marko, C. Hsieh, W. Moberlychan, C. A. Mannella, and J. Frank. Focused ion beam milling of vitreous water: prospects for an alternative to cryo-ultramicrotomy of frozen-hydrated biological samples. *Journal of Microscopy-Oxford*, 222(1):42–47, Apr. 2006. ISSN 0022-2720. doi: 10.1111/j.1365-2818.2006.01567.x.

[25] M. Marko, C. Hsieh, R. Schalek, J. Frank, and C. Mannella. Focused-ion-beam thinning of frozen-hydrated biological specimens for cryo-electron microscopy. *Nature Methods*, 4(3):215–217, 2007. ISSN 1548-7091. doi: 10.1038/nmeth1014.

[26] J. Mayer, L. A. Giannuzzi, T. Kamino, and J. Michael. TEM sample preparation and FIB-induced damage. *MRS Bulletin*, 32(5):400–407, 2007.

[27] J. P. McCaffrey, M. W. Phaneuf, and L. D. Madsen. Surface damage formation during ion-beam thinning of samples for transmission electron microscopy. *Ultramicroscopy*, 87(3):97–104, Apr. 2001. ISSN 0304-3991. doi: 10.1016/S0304-3991(00)00096-6.

[28] W. Melitz, J. Shen, A. C. Kummel, and S. Lee. Kelvin probe force microscopy and its application. *Surface Science Reports*, 66(1):1–27, 2011. ISSN 0167-5729. doi: DOI:10.1016/j.surfrep.2010.10.001.

[29] M. T. Myers, B. H. Sencer, and L. Shao. Multi-scale modeling of localized heating caused by ion bombardment. *Nuclear Instruments & Methods in Physics Research Section B-Beam Interactions with Materials and Atoms*, 272:165–168, Feb. 2012. ISSN 0168-583X. doi: 10.1016/j.nimb.2011.01.057.

[30] P. M. Nellen, V. Callegari, and R. Bronnimann. FIB-milling of photonic structures and sputtering simulation. *Microelectronic Engineering*, 83(4-9):1805–1808, 2006. ISSN 0167-9317. doi: 10.1016/j.mee.2006.01.176.

[31] K. Niihara, T. Kaneko, T. Suzuki, Y. Sato, H. Nishioka, Y. Nishikawa, T. Nishi, and H. Jinnai. Nanoprocessing and nanofabrication of a structured polymer film by the focused-ion-beam technique. *Macromolecules*, 38(8):3048–3050, Apr. 2005. ISSN 0024-9297. doi: 10.1021/ma048380m.

[32] A. Orthacker, R. Schmied, B. Chernev, J. E. Froch, J. Hobisch, G. Trimmel, and H. Plank. Chemical degradation and morphological instabilities during focused ion beam prototyping of polymers. *Physical Chemistry Chemical Physics*, 16(4):1658–66, 2014. doi: 10.1039/C3CP54037E.

[33] V. Palermo, M. Palma, and P. Samorì. Electronic Characterization of Organic Thin Films by Kelvin Probe Force Microscopy. *Advanced Materials*, 18(2):145–164, 2006. ISSN 1521-4095. doi: 10.1002/adma.200501394.

[34] L. Pastewka, R. Salzer, A. Graff, F. Altmann, and M. Moseler. Surface amorphization, sputter rate, and intrinsic stresses of silicon during low energy Ga+ focused-ion beam milling. *Nuclear Instruments & Methods in Physics Research Section B – Beam Interactions with Materials and Atoms*, 267(18):3072–3075, Sept. 2009. ISSN 0168-583X. doi: 10.1016/j.nimb.2009.06.094.

[35] T. Piok, H. Plank, G. Mauthner, S. Gamerith, C. Gadermaier, F. P. Wenzl, S. Patil, R. Montenegro, M. Bouguettaya, J. R. Reynolds, U. Scherf, K. Landfester, and E. J. W. List. Solution Processed Conjugated Polymer Multilayer Structures for Light Emitting Devices, 2005.

[36] L. Reimer. *Scanning Electron Microscopy: Physics of Image Formation and Microanalysis.* 1998. ISBN 9783540639763. doi: 10.1002/jobm.3620270311. URL `http:\books.google.de/books/about/Scanning_Electron_Microscopy.html?id=0Fm3T6F6_LEC&redir_esc=y`.

[37] J. C. Reiner, P. Nellen, and U. Sennhauser. Gallium artefacts on FIB-milled silicon samples. In *Microelectronics Reliability*, volume 44, pages 1583–1588, 2004. ISBN 0026-2714. doi: 10.1016/j.microrel.2004.07.073.

[38] M. Schaffer, J. Wagner, B. Schaffer, M. Schmied, and H. Mulders. Automated three-dimensional X-ray analysis using a dual-beam FIB. *Ultramicroscopy*, 107(8): 587–597, Aug. 2007. ISSN 0304-3991. doi: 10.1016/j.ultramic.2006.11.007.

[39] R. Schmied, B. Chernev, G. Trimmel, and H. Plank. New possibilities for soft matter applications: eliminating technically induced thermal stress during FIB processing. *RSC Advances*, 2(17):6932–6938, 2012. ISSN 2046-2069. doi: 10.1039/c2ra21025h.

[40] R. Schmied, J. E. Fröch, A. Orthacker, J. Hobisch, G. Trimmel, and H. Plank. A combined approach to predict spatial temperature evolution and its consequences during FIB processing of soft matter. *Physical Chemistry Chemical Physics*, 16(13): 6153–6158, 2014. doi: 10.1039/c3cp55308f.

[41] M. Sezen. *Nanostructuring and Modification of Conjugated Polymer Based Optoelectronic Device Structures by Focused Ion Beam.* Doctoral thesis, Graz University of Technology, 2009.

[42] M. Sezen, H. Plank, P. M. Nellen, S. Meier, B. Chernev, W. Grogger, E. Fisslthaler, E. J. W. List, U. Scherf, and P. Poelt. Ion beam degradation analysis of poly(3-hexylthiophene) (P3HT): can cryo-FIB minimize irradiation damage? *Physical Chemistry Chemical Physics*, 11(25):5130–5133, 2009. ISSN 1463-9076. doi: 10.1039/b816893h.

[43] M. Sezen, H. Plank, E. Fisslthaler, B. Chernev, A. Zankel, E. Tchernychova, A. Bluemel, E. J. W. List, W. Grogger, and P. Poelt. An investigation on focused electron/ion beam induced degradation mechanisms of conjugated polymers. *Physical Chemistry Chemical Physics*, 13(45):20235–20240, 2011. ISSN 1463-9076. doi: 10.1039/c1cp22406a.

[44] N. Shukla, S. K. Tripathi, A. Banerjee, A. S. V. Ramana, N. S. Rajput, and V. N. Kulkarni. Study of temperature rise during focused Ga ion beam irradiation using nanothermo-probe. *Applied Surface Science*, 256(2):475–479, 2009. ISSN 0169-4332. doi: 10.1016/j.apsusc.2009.07.024.

[45] R. Timilsina and P. D. Rack. Monte Carlo simulations of nanoscale focused neon ion beam sputtering. *Nanotechnology*, 24:495303, 2013. ISSN 1361-6528. doi: 10.1088/0957-4484/24/49/495303.

[46] I. Utke and P. E. Russel. *Nanofabrication using focused ion and electron beams: principles and applications*. Oxford University Press, New York, 1 edition, 2012.

[47] I. Utke, P. Hoffmann, and J. Melngailis. Gas-assisted focused electron beam and ion beam processing and fabrication. *Journal of Vacuum Science & Technology B*, 26(4):1197–1276, July 2008. ISSN 1071-1023. doi: 10.1116/1.2955728.

[48] G. H. Vineyard. Thermal Spikes and Activated Processes. *Radiation Effects and Defects in Solids*, 29(4):245–248, 1976. ISSN 1042-0150. doi: 10.1080/00337577608233050.

[49] C. A. Volkert and A. M. Minor. Focused ion beam microscopy and micromachining. *MRS Bulletin*, 32(5):389–395, 2007. ISSN 0883-7694. doi: 10.1557/mrs2007.62.

[50] Z. G. Wang, C. Dufour, E. Paumier, and M. Toulemonde. The S(E) Sensitivity of Metals Under Swift-Heavy-Ion Irradiation - A Transient Thermal-Process. *Journal of Physics-Condensed Matter*, 6(34):6733–6750, Aug. 1994. ISSN 0953-8984. doi: 10.1088/0953-8984/6/34/006.

[51] H. D. Wanzenboek, H. Langfischer, A. Lugstein, E. Bertagnollo, U. Grabner, P. Pongratz, J. Smoliner, and E. Gornik. Effects of Ga-ion irradiation on properties of materials processed by a Focused Ion Beam (FIB). In *MRS Symposium Proceedings*, pages O6.6.1 – O6.6.9, 2001.

[52] P. K. Weber, G. A. Graham, N. E. Teslich, W. M. Chan, S. Ghosal, T. J. Leighton, and K. E. Wheeler. NanoSIMS imaging of Bacillus spores sectioned by focused ion beam. *Journal of Microscopy*, 238(3):189–199, 2010.

[53] D. B. Williams and C. B. Carter. *Transmission Electron Microscopy: A Textbook for Materials Science*, volume V1-V4. 2009. ISBN 9780387765006. doi: 10.1007/978-1-61779-415-5_23. URL http://www.loc.gov/catdir/enhancements/fy0820/96028435-d.html.

[54] B. J. P. Z. M. D. Ziegler J. F. *SRIM : the stopping and range of ions in matter*. SRIM Co., Chester, Md., 2012. ISBN 9780965420716 096542071X.

A. Curriculum Vitae

Curriculum Vitae

Dipl. Ing. Roland Schmied, BSc - Friedrichgasse 37/11 - 8010 Graz / Austria
roland.schmied@oeaw.ac.at - +43 650 985 23 12

Personal Data

Name:	Roland Schmied
Date of birth:	23/12/1985
Place of birth:	Wolfsberg/Austria
Nationality :	Austrian
Academic degree:	Dipl. Ing., BSc

Profession

08/14 - to date	PostDoc Position at the *Space Research Institute, Austrian Academy of Science* on the operations and science of the MIDAS (Micro-Imaging Dust Analysis System) atomic force microscope within the ESA ROSETTA mission

Education

08/11 - to date	Ph.D student in technical physics at the *Graz Centre for Electron Microscopy* and the *Institute for Electron Microscopy and Nanoanalysis, Graz University of Technology*
02/08 - 07/11	Masters of Science degree in technical physics at the *Institute for Electron Microscopy and Nanoanalysis, Graz University of Technology*, on the topic of *Fundamental Proximity Effects for Electron Beam Induced Deposition Processes”*
10/05 - 02/08	Bachelor of Science degree in technical physics at the Graz University of Technology, on the topic of *The International Nuclear Event Scale”*
09/04 - 09/05	Military Service including the education for officers
09/96 - 07/04	A - Level at the BG/BRG Peraustraße Villach
09/92 - 07/96	Elementary School, Villach

PEER REVIEW PUBLICATIONS

R. Schmied, J.D. Fowlkes, P.D. Rack, H. Plank, *Fundamental Edge Broadening Effects during Focused Electron Beam Induced Nanosynthesis*, invited at Beilstein Journal of Nanotechnology, in review, 2014

T. Rothländer, J. Kraxner, R. Schmied, A. Haase, H.Gold, W. Grogger and B. Stadlober, *Influence of the source-gate and drain-gate overlap length on the on-current of self-aligned, NIL structured OTFTs*, in submission, 2014

R. Schmied, J. E. Froech, A. Orthacker, J. Hobisch, G. Trimmel and H. Plank, *A combined approach to predict spatial temperature evolution and its consequences during FIB processing of soft matter*, Phys. Chem. Chem. Phys., 2014, 16 (13), 6153 - 6158

J. Kraxner, R. Schmied, T. Rothländer, H. Plank, W. Grogger, *New Possibilites in Polymer Preparation and Analysis*, Imaging and Analysis, October 2014

B. Geier, C. Gspan, R. Winkler, R. Schmied, J.D. Fowlkes, H. Fitzek, S. Rauch, J. Rattenberger, P.D. Rack, H. Plank, *Rapid and highly compact purification for focused electron beam induced deposits: a low temperature approach using electron stimulated* H_2O *reactions*, Journal of Physical Chemistry C, 2014, 118 (25), 14009 - 14016

A. Orthacker, R. Schmied, B. Chernev, J. E. Froech, R. Winkler, J. Hobisch, G. Trimmel, H. Plank, *Chemical degradation and morphological instabilities during focused ion beam prototyping of polymers*, Phys. Chem. Chem. Phys., 2014, 16 (4), 1658 - 1666

R. Schmied, B. Chernev, G. Trimmel and H. Plank, *New possibilities for soft matter applications: eliminating techically induced thermal stress during FIB processing*, RSC Advances, 2012, 2, 6932 - 6938

CONFERENCE CONTRIBUTIONS

invited Talk:	FOCUSED ION BEAM PROCESSING OF LOW MELTING POLYMERS: NEW PERSPECTIVES DUE TO OPTIMIZED PATTERNING STRATEGIES, Symposium on Ultramicrotomy and Methods in Material Science, October 2013, Halle/GERMANY
invited Talk:	FOCUSED ION BEAM PROCESSING OF SOFT MATTER: FROM FUNDAMENTAL EFFECTS TOWARDS TEM LAMELLA PREPARATION, 8th FIB Workshop, June 2013, Unterpremstätten/AUSTRIA

Talk : Temperature Evolution during FIB Processing of Soft Matter: From Fundamentals towards TEM Lamella Preparation, 18th International Microscopy Congress IMC, September 2014, Prague/CZECH REPUBLIC

Talk: Temperature Evolution during Focused Ion Beam Processing of Soft Matter: From Fundamentals towards TEM Lamella Preparation, 4th ASEM Workshop, May 2014, Vienna/AUSTRIA

Talk: Temperature Evolution During Focused Ion Beam Processing of Low Melting Materials, May 2013, EMRS Spring Meeting Strasbourg/FRANCE

Talk: Focused Ion Beam Processing of Soft Matter, 7th FIB Workshop, June 2012, Dresden/GERMANY

Talk: Focused Ion Beam Processing of Soft Matter, 2nd ASEM Workshop, April 2012, Salzburg/AUSTRIA

Talk: Fundamental Proximity Effects for the Electron Beam Induced Deposition Process, 10th Multinational Congress on Microscopy, September 2011 , Urbino/ITALY

Poster: New Possibilities of Soft Matter Applications: Eliminating Technically Induced Thermal Stress during FIB Processing, Microscopy Conference, August 2013, Regensburg/GERMANY

Poster: Advances in FIB Soft Matter Processing, 15th European Microscopy Congress, September 2012, Manchester/UNITED KINGDOM

SCIENTIFIC AWARDS

Fritz-Grasenick-Preis 2013 of Austrian Society for Electron Microscopy for *Focused Ion Beam Processing of Polymers: From Simulations towards TEM Lamella Preparation*

PROJECTS AND THESES

Technical responsibility	FFG Project on FIB Soft Matter Processing - Project number 830186
Thesis	Co - Supervisor of 1 Master and 3 Baccalaureate Theses

Personal Skills and Competences

Native Language:	German
others	English (C1), French (B2), Italian (A1)
Computer Skills:	ECDL
	Fundamental Knowledge in Computer Simulations (Finite Elements (ANSYS,COMSOL), Monte Carlo Simulations)
	Programming Language (C, Visual Studio)
	Programs (MatLab, Adobe Photoshop, CorelDraw, Origin)
Social Skills:	Leadership: acquired at military service
	Teamwork: aquired at different team sports